Different regimes of high harmonics generation in plasma skin layer

Inaugural Dissertation

zur Erlangung des Doktorgrades der
Mathematisch-Naturwissenschaftlichen Fakultät der
Heinrich-Heine-Universität Düsseldorf

vorgelegt von

Mykyta Cherednychek
aus Charkiw

Düsseldorf, August 2016

aus dem Institut für Theoretische Physik 1
der Heinrich-Heine-Universität Düsseldorf

Gedruckt mit der Genehmigung der
Mathematisch-Naturwissenschaftlichen Falultät der
Heinrich-Heine-Universität Düsseldorf

Referent: Prof. Dr. Alexander Pukhov
Korreferent: Prof. Dr. Dr. Carsten Müller

Tag der mündlichen Prüfung: Oktober 19, 2016

Erklärung

Ich, Mykyta Cherednychek, versichere hiermit, dass ich die vorliegende Dissertation selbstständig und ohne unzulässige, fremde Hilfe angefertigt habe. Alle von mir verwendeten Quellen und Hilfsmittel sind angegeben.

Ort, Datum: Düsseldorf, 12.08.2016 Untreschrift:

Zusammenfassung

Mit der Erzeugung von hohen Harmonischen auf der Plasmaoberfläche ist es möglich einen Laserpuls in eine Reihe von aufeinander folgenden Attosekunden- oder sogar Zeptosekunden- Pulsen in der Rückstrahlung umzuwandeln. Diese Attosekunden-Pulse können eine Amplitude haben, die unter bestimmten Voraussetzungen um einige Größenordnungen höher als die Amplitude des Laserpulses ist. Wir untersuchen diesen Vorgang im Detail. Speziell schauen wir uns die sogenannten Nano-Bündeln von Plasma-Elektronen an. Wir leiten einen analytischen Ausdruck her, der das Elektronendichte-Profil beschreibt und erhalten eine gute Übereinstimmung mit particle-in-cell-Simulationen. Wir erforschen den effizientesten Fall der Erzeugung von hohen Harmonischen bei moderaten Laserintensitäten ($I \approx 2 \cdot 10^{20} W/cm^2$) auf dem überdichten Plasma mit einem exponentiellen Vorplasma-Profil. Wir berechnen die Spektren der einzelnen Attosekunden-Pulse von der Rückstrahlung. Dabei verwenden wir unseren Ausdruck für das Dichte-Profil kombiniert mit der Gleichung für das Spektrum der Nano-Bündel-Strahlung.

Darüber hinaus präsentieren wir einen neuen Mechanismus für die Erzeugung von extrem-ultravioletten Attosekunden-Pulsen (XUV) an der von einem Laser bestrahlten überdichten Plasmaoberfläche im Wellenbrechungszustand. Durch die particle-in-cell-Simulationen und Analysis demonstrieren wir, dass die erhaltene ultra-kurze XUV Emission, bei den Parametern, die wir verwendet haben, größtenteils wegen den starken Plasmadichte-Oszillationen und nachfolgender Wellenbrechung zustande kommt. Die Kopplung der starken Dichtevariation und der Querfelder an der vorderen Oberflächenschicht gibt den Anlass für die transmittierte Emission mit Frequenzen im Bereich der lokalen Plasmafrequenz. Dieser Mechanismus öffnet neue Einsichten in das Szenarium von XUV Erzeugung an den Festkörperoberflächen und auf die Dynamik von Laser-Plasma-Wechselwirkungen.

Abstract

With the high-order harmonic generation (HHG) from plasma surfaces it is possible to turn a laser pulse into a train of attosecond or even zeptosecond pulses in the backward radiation. These attosecond pulses may have amplitude several orders of magnitude higher than that of the laser pulse under appropriate conditions. We study this process in detail, especially the nanobunching of the plasma electron density. We derive an analytical expression that describes the electron density profile and obtain a good agreement with particle-in-cell simulation results. We investigate the most efficient case of HHG at moderate laser intensity ($I \approx 2 \cdot 10^{20} W/cm^2$) on the over-dense plasma slab with an exponential profile pre-plasma. Subsequently we calculate the spectra of a single attosecond pulse from the backward radiation using our expression for the density shape in combination with the equation for the spectrum of the nanobunch radiation.

Further we present a new mechanism of attosecond extreme-ultraviolet (XUV) pulses generation from a relativistic laser-driven overdense plasma surfaces in the wavebreaking regime. Through particle-in-cell simulations and analysis, we demonstrate that the observed ultrashort XUV emission for the parameters we considered is predominantly due to a strong plasma-density oscillation subsequent to wavebreaking. The coupling of the strong density variation and the transverse fields in the front surface layer gives rise to the transmitted emission with frequencies mainly around the local plasma frequency. This mechanism provides new insights into the scenarios of XUV generation from solid surfaces and the dynamics of laser-plasma interactions.

Danksagung

Ich möchte hier meine Dankbarkeit an die Leute ausdrücken, die mir während meiner Promotion geholfen und mich unterstützt haben.

Ein riesengroßes Dankeschön geht an meinen Betreuer Prof. Dr. Alexander Pukhov, der mich in seine Arbeitsgruppe aufgenommen hat. Ich danke ihm sowohl für die extrem präzisen Tipps, die mich jedes Mal einen Schritt nach vorne brachten, als auch für das Vertrauen und die Möglichkeit vieles selbstständig zu machen, Ansätze zu suchen und Entscheidungen zu treffen. Diese Erfahrung war für mich sehr wertvoll.

Vielen Dank an Prof. Dr. Dr. Carsten Müller, der so nett war das Korreferat meiner Arbeit zu übernehmen. Außerdem möchte ich mich für die großartige Zusammenarbeit bei der Lehre in seiner Arbeitsgruppe bedanken, wo ich als Übungsgruppenleiter mitwirkte.

Weiterhin bedanke ich mich ganz herzlich bei unserem Systemadministrator Evgenij Bleile für die hochprofessionelle technische Unterstützung und für die enorme Hilfsbereitschaft.

Vielen Dank an Frau Elvira Gröters, die immer sehr nett war und bei allen bürokratischen Fragen geholfen hat.

Selbstverständlich möchte ich noch meine Dankbarkeit an meine weiteren Arbeitskollegen aussprechen. Das ist zu aller erst der Dr. Zi-Yu Chen mit dem wir einige Zeit eng zusammenarbeiteten und von dem ich viel gelernt habe. Danke an Dr. Götz Lehmann und Dr. John Farmer, die immer nett zu mir waren und aufgrund ihrer hohen Kompetenz und Hilfsbereitschaft bei vielen kleinen Fragen und Problemen helfen konnten. Außerdem sorgten auch Alexey Snydnikov, Tobias Tückmantel, Liangliang Ji, Oliver Jansen, Phuc Luu, Friedrich Schluck, Vural

Kaymak, Roberto Martorelli, Selym Villalba, Matthias Dellweg, Martin Jansen, Longquing Yi, Debin Zou und Christoph Baumann für die perfekte Atmosphäre in der Gruppe.

Abschließend bedanke ich mich ganz herzlich bei meinen Eltern, die mich immer in allen Fragen und mit vollem Einsatz unterstützt haben.

Contents

Chapter 1

Introduction

Since the invention of laser in the year of 1960 [1], laser technology has witnessed an immense progress [2–17]. The typical duration of a laser pulse was drastically reduced from several nanoseconds in sixties to a few femtoseconds in our days. On the other hand the power of a laser systems was grown constantly during last fifty years and the threshold of 2PW was broken recently [16].

Everything started with lasers of the light power exiting the kilowatt range and reaching 10^9 W/cm^2 intensity (Fig. 1.1), which opened the door to nonlinear optics. during the seventies the lasers that could reach 10^{14} W/cm^2 intensity were constructed. The revolutionary invention of the chirped pulse amplification technique brought the laser to a completely new level in 1985 [2]. That was the most important breakthrough in the history of laser technology.

The idea of the CPA is based on a sequence stretcher-amplifier-compressor. Simply speaking, we stretch an initially short but weak pulse, then amplify the long pulse and subsequently perform a compression in order to obtain a short and strong pulse. Obviously the question arises why can not the original short pulse be amplified directly? The point is that the optical setup would not be able to stand such power. Let us consider the CPA process in details. We can start with Ti:Sa-laser containing some nJ of energy. In order to stretch the pulse and to be able to reverse this process afterwords we impose a positive chirp to the pulse. That means if the pulse passes through an optical medium the waves with lower frequencies containing in the pulse propagate faster then the corresponding waves with higher frequencies. This process causes a broadening of the pulse. With this principle the stretching factor of the order 10^4 can be reached. The amplification

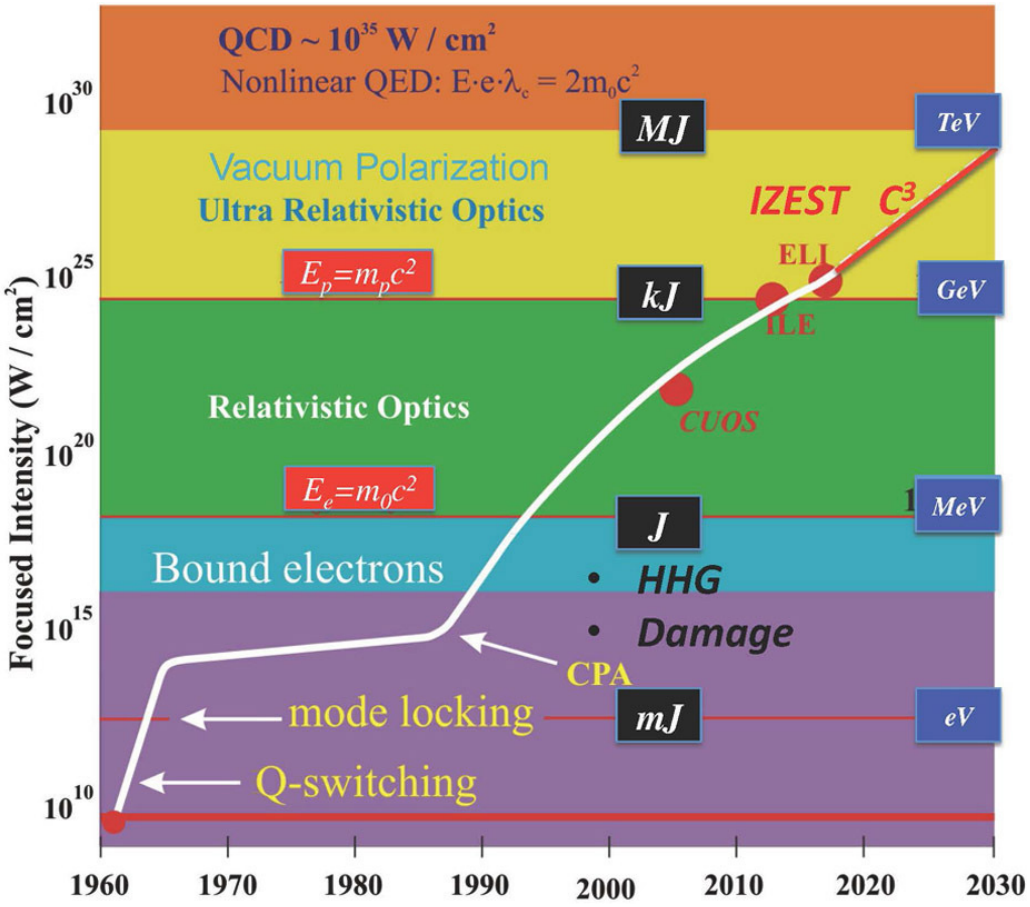

Figure 1.1: (Taken from [18]) Intensity development since beginning from the year 1960, when the first laser was produced. The red line is an aim of the project proposed by International Center for Zetta- and Exawatt Science and Technology (IZEST). Black boxes show typical laser energies. Blue boxes show typical particle energies. QCD: Quantum chromodynamics. QED: Quantum electrodynamics. E: Electric field. e: Electron charge. λ_c: Compton wavelength. m_0: Electron mass. c: Speed of light. E_p: Proton energy. m_p: Proton mass. E_e: Electron energy. C_3: Cascaded conversion compression. ELI: Extreme Light Infrastructure. ILE: Institut de la Lumiere Extreme. CUOS: Center for Ultrafast Optical Science. HHG: High harmonic generation. CPA: Chirped pulse amplification.

process is usually divided in several stages using pump lasers. Finally the amplified pulse is compressed by adding a negative chirp.

Roughly twenty years after invention of CPA the record peak intensity of order $10^{22}W/cm^2$ was reached by focusing of a 45-TW laser beam [12]. Recently, a compression scheme has been proposed that opens the possibility to generate ultra-short and ultra-strong laser pulses with focused intensities of $10^{24}W/cm^2$ and duration of 2fs [17].

The red line in Fig. 1.1 describes the aim of International Center for Zetta- and Exawatt Science and Technology (IZEST). IZEST plans to explore new low-repetition-rate technologies and architectures. The symbol C^3 is the name of a new amplification method for cascaded conversion compression [18]. With this method it should be possible to generate femtosecond pulses with the peak power above one exawatt. The corresponding intensities should reach the Schwinger limit ($8 \cdot 10^{30}\mathrm{W/cm^2}$), where nonlinear effects in vacuum occur.

The progress in laser technology offers an opportunity to study new physical phenomena of laser plasma interactions. One of the most important processes in this field is the HHG, which has been studying very intensely nowadays. As the minimum achievable duration of laser pulses continuously reduces towards few femtoseconds, the generation of even shorter pulses (in the attosecond or even zeptosecond range) is possible only for radiation with shorter wavelengths. The reduction of the pulse duration and the radiation wavelength would open new horizons for potential applications, including the exploration of novel ultrafast dynamics with unprecedented temporal resolution[19], investigation of nonlinear optics in the XUV region[20], and as a probe for laser-plasma interactions[21, 22]. This is the main motivation in studying the high harmonic generation.

First observations of HHG from plasmas were made in 1981 [23, 24]. Rather matured is HHG in gases that allows to generate single attosecond pulses with duration less than 1fs [25–28]. However, this method of HHG requires the limitation of laser pulse intensity by maximum $10^{15}W/cm^2$ in order to prevent the ionization.

Fortunately, there is another method of efficient production of high-order harmonics by unlimited laser power. This is the interaction process of high

contrast laser pulses [29] with solid density targets. The pedestal of the pulse ionizes the surface and the main pulse interacts with electrons of the overdense plasma, while ions remain nearly immobile during the short pulse duration. One distinguishes two main HHG mechanisms in this case: coherent wake emission (CWE) [29–31] and the "relativistically oscillating mirror" (ROM) [32–40].

CWE is caused by fast Brunel electrons [41], which excite plasma oscillations at the local plasma frequencies. Thus, there are no harmonics beyond the maximal plasma frequency in the case of CWE. This process dominates for non-relativistic laser intensities $a_0 \lesssim 1$.

For $a_0 \gg 1$ the harmonics are generated mostly via the ROM mechanism. In this case, the electron layer at the plasma surface acts as a mirror that oscillates at relativistic velocities, resulting in the generation of high-order harmonics via Doppler effect when the surface moves towards the incident wave. During this process there is no limit of frequency like by CWE, so higher harmonics can be generated. The first theoretical description of ROM claimed that the intensity spectrum envelope of reflected wave can be described by $I(n) \propto n^{-5/2}$ up to the "roll over" frequency ω_r which is proportional to $4\gamma^2$, where n is the harmonic order and γ is the relativistic gamma factor [35]. Later this theory was improved, especially the acceleration of the reflecting layer was taken into account. This leads to the power law $I(n) \propto n^{-8/3}$ and $\omega_r \propto \gamma^3$ [37]. This model assumes the existence of a so called apparent reflection point (ARP) where the transverse electric field vanishes. Predictions based on that model where experimentally confirmed [38–40].

Most recently another HHG mechanism was discovered. Using p-polarized oblique incident light with $a_0 \gg 1$ one can cause the formation of extremely dense electron nanobunches under appropriate conditions. These bunches can emit attosecond pulses with intensities much larger compared to the incident pulse [42, 43]. This means that the boundary condition assumed in [37] corresponding to ARP fails and thus the ROM theory can not be applied in this case. This process is called coherent synchrotron emission (CSE). The reflected radiation in case of CSE in characterized by the power law $I(n) \propto n^{-4/3}$ or $I(n) \propto n^{-6/5}$ which is flatter comparing to ROM [42, 43]. The corresponding experiments can be found in Ref. [44–46]. Detailed numerical investigation of the case of p-polarized oblique incidence in Ref. [47] demonstrate that the ROM model can be violated when the

similarity parameter $S = n/a_0$ (where n is the electron density given in units of the critical density n_c and a_0 is the dimensionless laser amplitude [48]) is smaller than five. The authors of [47] present a new relativistic electronic spring (RES) model for $S < 5$.

Since usually one obtains a train of attosecond pulses by HHG, the question is whether it is possible to isolate one single pulse. One method is to use the polarization gate technique [49, 50]. This is important because it opens the opportunity to a number of potential applications [51]. Successful application of λ^3 focusing could even lead to investigation of vacuum instabilities [36, 52].

This work begins with an overview of the theoretical aspects of laser plasma interaction. Chapter 2 is dedicated to that topic. Here we derive some relations which are used in further topics starting from basic fundamental laws. In further chapters two different mechanisms of HHG are considered.

We pursue two main goals in chapter 3. The first one is to provide a more detailed analytical description of the spectrum in the case of CSE compared to [42, 43]. For this purpose we introduce an analytical approach which allows us to calculate the electron density profile of the given nanobunch as well as its current distribution, that are used in formulas for back-radiating spectrum derived in [42, 43]. Subsequently we compare the derived expressions with one-dimensional simulation results done with the VLPL PIC code. The second aim is to determine the most efficient case of HHG at moderate laser intensity ($I \approx 2 \cdot 10^{20} W/cm^2$). For that reason we perform several 1D PIC simulations with different parameters. Finally we analyze the obtain results and define different regimes of HHG. In the last section of the chapter we consider the nanobunches moving and radiating in forward direction.

In chapter 4, we report a new mechanism of ultrafast XUV pulse generation from laser-irradiated plasma surfaces in the wavebreaking regime. The attosecond XUV pulse is generated from the front layer of the plasma and then propagates through the foil target, with frequencies mainly around the local plasma frequency. Through simulations and analysis, we identify the underlying physics is predominately due to the strong plasma-density oscillation in the surface layer subsequent to wavebreaking, which we call wavebreaking-associated transmitted emission (WTE). We also show that the emission is a general process for a wide

range of laser and plasma parameters in the wavebreaking regime. Besides offering a new option to generate ultrafast XUV pulses, the radiation process identified here also provides important insights into the mechanism of XUV generation and the dynamics of laser-plasma interactions.

Chapter 2

Theoretical basics of the laser-plasma interaction

In this chapter we are going to review an important theoretical basics such as ultrashort pulse propagation, laser driven plasma oscillations and radiation from perturbed plasma. Starting from fundamental equations of electrodynamics we will derive some well known laws which are important in laser-plasma physics. Although we always will begin with general approach, we will specify the results for one dimensional case, since this is important case for further chapters.

2.1 Ultrashort pulse propagation

Since we are basically dealing with ultrashort electromagnetic pulses in this work, let us firstly consider how such pulses propagate in vacuum. We start our review with discussion of electromagnetic waves in general and then go over to the short pulses.

2.1.1 Electromagnetic plane wave in vacuum

Electromagnetic waves are electric and magnetic fields oscillating and propagating in space, while both fields are always perpendicular to each other and behave in the same way. Thus without loss of generality we will consider only behavior of the electric field $\boldsymbol{E}(\boldsymbol{r}, t)$ further. The fields of a wave in absence of charges and currents have to satisfy the wave equation

$$\Delta \boldsymbol{E}(\boldsymbol{r}, t) - \frac{1}{c^2} \frac{\partial^2 \boldsymbol{E}(\boldsymbol{r}, t)}{\partial t^2} = 0, \tag{2.1}$$

that can be immediately derived from the Maxwell equations

$$\nabla \times \boldsymbol{E} + \frac{1}{c}\frac{\partial}{\partial t}\boldsymbol{B} = 0, \qquad \nabla \cdot \boldsymbol{B} = 0, \tag{2.2}$$

$$\nabla \times \boldsymbol{B} - \frac{1}{c}\frac{\partial}{\partial t}\boldsymbol{E} = 0, \qquad \nabla \cdot \boldsymbol{E} = 0 \tag{2.3}$$

for $\boldsymbol{J} = 0$ and $q = 0$. One of the simplest and common examples solving equation (2.1) is the plane wave

$$\boldsymbol{E}(\boldsymbol{r}, t) = \boldsymbol{E}_0 e^{i(\boldsymbol{k}\cdot\boldsymbol{r} - \omega t)}, \tag{2.4}$$

with the constant amplitude $\boldsymbol{E}_0$, the oscillation frequency ω and the wave vector $\boldsymbol{k}$. If the direction of $\boldsymbol{E}_0$ remains constant then we are dealing with linear polarized wave. The wave vector $\boldsymbol{k}$ determines the propagation direction of the wave and its absolute value is given by $k = \omega/c$. The vectors $\boldsymbol{E}_0$ and $\boldsymbol{k}$ are orthogonal to each other so we have a wave that propagates with the speed of light in the direction perpendicular to its field oscillations. The physical field is represented by the real part of $\boldsymbol{E}(\boldsymbol{r}, t)$. Further we are going to consider only linearly polarized waves. In this case we can choose the coordinates in the way that the vector $\boldsymbol{E}(\boldsymbol{r}, t)$ has only one nonzero component $E(\boldsymbol{r}, t)$, so the equation (2.1) can be reduced to

$$\Delta E(\boldsymbol{r}, t) - \frac{1}{c^2}\frac{\partial^2 E(\boldsymbol{r}, t)}{\partial t^2} = 0. \tag{2.5}$$

Considering the wave propagating along the z-axis we have

$$E(\boldsymbol{r}, t) = E_0 e^{i(kz - \omega t)}. \tag{2.6}$$

In Fig. 2.1 one can see the sketch of such wave. However the field described by (2.6) does not depend on x and y coordinates, moreover the wave is infinitely wide. Of course this is absolutely non realistic case. In the next chapter we are going to derive the expression for pulses that are spatially localized concerning to x-y-plane.

2.1.2 Paraxial wave equation

In order to derive the expression for some localized electromagnetic waves we generalize the equation (2.6) to

$$E(\boldsymbol{r}, t) = E_0(\boldsymbol{r}) e^{i(kz - \omega t)}. \tag{2.7}$$

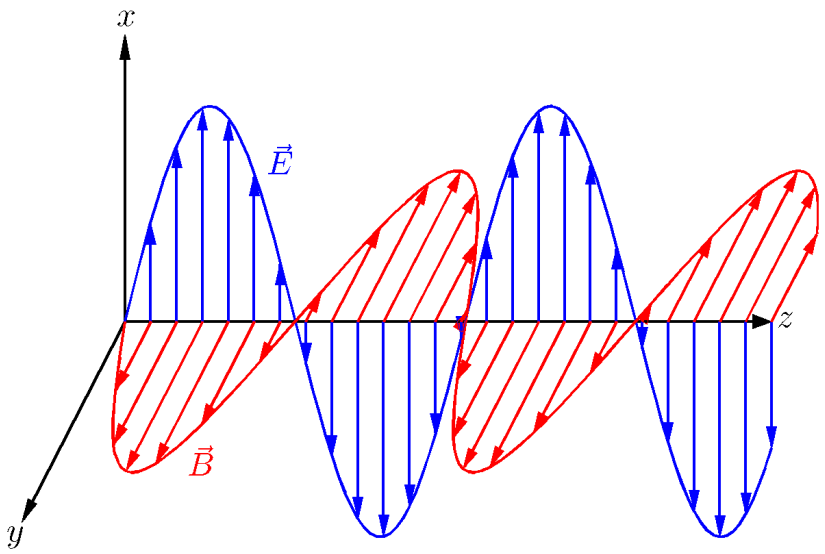

Figure 2.1: (Taken from [53]) Schematic representation of the electromagnetic plane wave.

Now the amplitude $E_0(\boldsymbol{r})$ is not a constant any more but represents the envelope of the pulse. In order to determine possible envelopes we insert this approach in (2.5) and obtain:

$$\left(\frac{\partial^2}{\partial x^2}+\frac{\partial^2}{\partial y^2}+\frac{\partial^2}{\partial z^2}+2ik\frac{\partial}{\partial z}\right)E_0(\boldsymbol{r})=0. \tag{2.8}$$

This deferential equation represents quite difficult mathematical problem. Nevertheless we can apply well known paraxial approximation [54] by assuming that $E(\boldsymbol{r})$ varies only slowly on the intervals of the order of one wave length λ. This is a good approximation for the most laser systems. Particularly that means

$$\left|\frac{\partial^2 E_0}{\partial z^2}\right| \ll k\left|\frac{\partial E_0}{\partial z}\right|, \tag{2.9}$$

so the equation (2.8) takes the form

$$\left(\frac{\partial^2}{\partial x^2}+\frac{\partial^2}{\partial y^2}+2ik\frac{\partial}{\partial z}\right)E_0(\boldsymbol{r})\cong 0. \tag{2.10}$$

One can find the detailed derivation of the solution of this equation in [54]. We give only the final result:

$$E_0^{mn}(\boldsymbol{r}) = \mathcal{E}\frac{w_0}{w(z)}H_m\left(\sqrt{2}\frac{x}{w(z)}\right)H_n\left(\sqrt{2}\frac{y}{w(z)}\right) \times e^{-\frac{x^2+y^2}{w^2(z)}+i\frac{k(x^2+y^2)}{2R(z)}-i(m+n+1)\tan^{-1}\left(\frac{z}{z_0}\right)}. \tag{2.11}$$

The numbers m and n are integers and start by zero. Correspondingly H_j denotes j-th order Hermite polynomial. Further parameters are defined by

$$R(z) = z + \frac{z_0^2}{z}, \tag{2.12}$$

$$w(z) = w_0\sqrt{1-\frac{z^2}{z_0^2}}, \tag{2.13}$$

$$z_0 = \frac{1}{2}kw_0^2. \tag{2.14}$$

Let us say that $\mathcal{E}$ and w_0 are just some constants. The indices m and n determine the particular beam mode also called $\mathrm{TEM_{mn}}$ mode. One may ask how good differed modes can be realized in experiments. The most appropriate in this case are lasers with hemispherical resonators because of low sensitivity to mirror misalignments. A common example of this type of lasers are the He-Ne lasers. In Fig. 2.2 different modes of a He-Ne laser are shown. Here we see the distribution of the intensity in the xy-plane on the certain distance from the laser. We are interested in the lowest $\mathrm{TEM_{00}}$ mode that is common in many applications and exhibits Gaussian distribution.

2.1.3 Gaussian laser beams

The envelope for $m = n = 0$ is given by

$$E_0(\boldsymbol{r}) = \mathcal{E}\frac{w_0}{w(z)}e^{-\frac{x^2+y^2}{w^2(z)}+i\frac{k(x^2+y^2)}{2R(z)}-i\tan^{-1}\left(\frac{z}{z_0}\right)}. \tag{2.15}$$

The function $w(z)$ characterizes the width of the beam. Its minimum w_0 by $z = 0$ is called beam waist (Fig. 2.3, from [54]). The number z_0 is called Rayleigh range and characterizes the length of the waist region. The quantity $R(z)$ is the radius of the curvature of the wave front defined by (2.12). It is infinite in the center of the waste ($z = 0$) and for large numbers of z we have $R(z) \approx z$. That means the

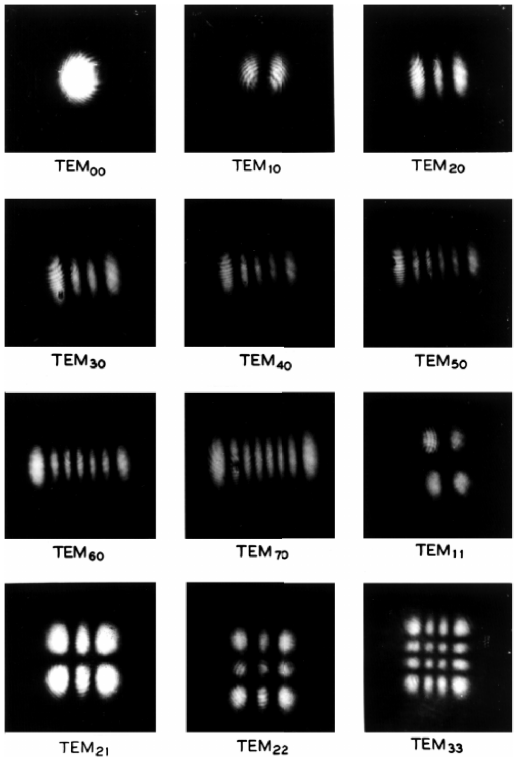

Figure 2.2: (Taken from [54]) Transverse Modes of He-Ne laser.

wave front behaves like a spherical wave with the center of curvature by $z = 0$. The term $\tan^{-1}\left(\frac{z}{z_0}\right)$ determines the phase shift along the z-axis ($x = y = 0$), which varies between $-\pi/2$ and $\pi/2$.

2.1.4 Ultrashort laser pulses

So far we have considered the simplest solution of the wave equation: the plane wave. We could spatially localize it via introduction of the envelope function $E_0(r)$ and solution of the paraxial wave equation. Since we are interested in short pulses we also need a temporal localization. Untill now we had a radiation source oscillating with the single frequency ω and time independent amplitude. Of course

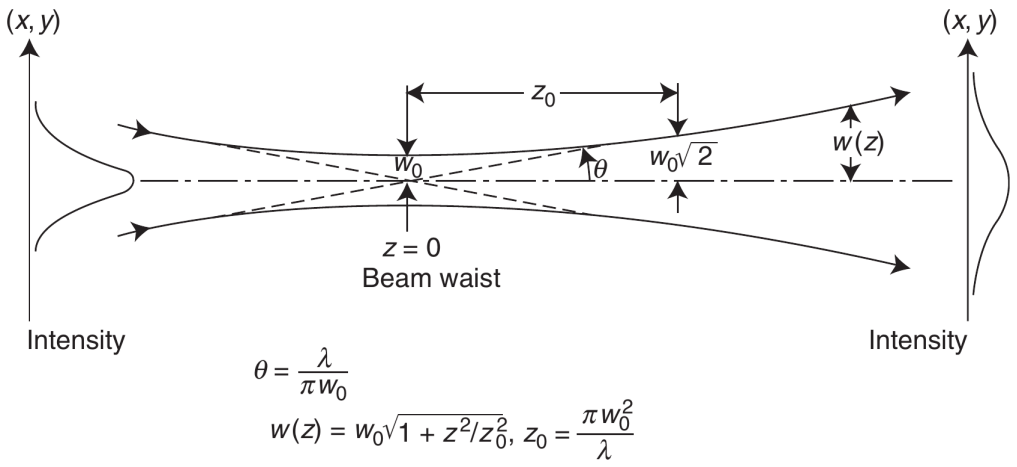

Figure 2.3: (Taken from [54]) Variation of spot size $w(z)$ of a Gaussian beam.

this is a non realistic case since the source would be infinitely wide on the time scale. In contrary to that a time localized source always has some finite frequency spectrum. Let us go along the lines of [55] and consider a radiation source $E(\boldsymbol{r}_\perp, t)$ at the position $z = 0$ with the spectrum $\hat{E}(\boldsymbol{r}_\perp, \omega)$, where $\boldsymbol{r}_\perp \equiv (x, y)$. The source produces the field $E(\boldsymbol{r}, t)$ which propagates along the z-axis. We assume that the spectrum can be written as $\hat{E}(\boldsymbol{r}_\perp, \omega) = \hat{p}(\omega)\hat{U}(\boldsymbol{r}_\perp)$ with $\hat{U}(0) = 1$. That means $\hat{p}(\omega)$ is the spectrum at the point $\boldsymbol{r}_\perp = 0$, where the source is approximately localized. The field at the coordinate origin is given by

$$E(0, t) = \frac{1}{\pi}\int_0^\infty \hat{p}(\omega)e^{-i\omega t}d\omega. \tag{2.16}$$

Here we can easily check that if the spectrum contains only one single frequency $\hat{p}(\omega) \propto \delta(\omega - \omega_0)$, then $E(0, t) \propto e^{-i\omega_0 t}$ like in the previous case. The spectrum $\hat{E}(\boldsymbol{r}, \omega)$ of the field $E(\boldsymbol{r}, t)$ for $z > 0$ can be written as

$$\hat{E}(\boldsymbol{r}, \omega) = \hat{p}(\omega)\hat{U}(\boldsymbol{r}, \omega) = \hat{p}(\omega)\psi(\boldsymbol{r}, \omega)e^{i\frac{\omega}{c}z}. \tag{2.17}$$

Obviously because of

$$E(\boldsymbol{r}, t) = \frac{1}{\pi}\int_0^\infty \hat{E}(\boldsymbol{r}, \omega)e^{-i\omega t}d\omega, \tag{2.18}$$

using the paraxial approximation we can write

$$\left(\frac{\partial^2}{\partial x^2}+\frac{\partial^2}{\partial y^2}+2i\frac{\omega}{c}\frac{\partial}{\partial z}\right)\psi(\boldsymbol{r},\omega)\cong 0. \tag{2.19}$$

Moreover the paraxial approximation implies $\psi(\boldsymbol{r},\omega)=\psi(\boldsymbol{r}_\perp,\frac{\omega}{c}z)$. Further we use the exponential form of $\hat{U}(\boldsymbol{r},\omega)$ and obtain

$$E(\boldsymbol{r},t)=\frac{1}{\pi}\int_0^\infty \hat{p}(\omega)a(\boldsymbol{r},\omega)e^{-i(\omega t-\varphi(\boldsymbol{r},\omega))}d\omega, \tag{2.20}$$

with $a(\boldsymbol{r},\omega)=|\psi(\boldsymbol{r}_\perp,\frac{\omega}{c}z)|$ and $\varphi(\boldsymbol{r},\omega)=\frac{\omega}{c}z+\arg\psi(\boldsymbol{r}_\perp,\frac{\omega}{c}z)$. Since we are interested in the envelope of the propagating field which is temporal and spatially localized. Thus we can define the envelope function $A(\boldsymbol{r},t)$ in the way:

$$E(\boldsymbol{r},t)=A(\boldsymbol{r},t)e^{-i(\omega_0 t-\varphi(\boldsymbol{r},\omega_0)-\phi)}, \tag{2.21}$$

where ϕ is an additional phase. That means we have enveloped propagating field, which oscillates with the constant frequency ω_0. The choice of ω_0 depends on the shape of $\hat{p}(\omega)$ and can be expressed as

$$\omega_0=\frac{\int_0^\infty \omega|\hat{p}(\omega)|d\omega}{\int_0^\infty|\hat{p}(\omega)|d\omega}. \tag{2.22}$$

Comparing the equations (2.20) and (2.21) we can follow:

$$A(\boldsymbol{r},t)=\frac{1}{\pi}\int_0^\infty \hat{p}(\omega)a(\boldsymbol{r},\omega)e^{-i((\omega-\omega_0)t-\varphi(\boldsymbol{r},\omega)+\varphi(\boldsymbol{r},\omega_0)+\phi)}d\omega. \tag{2.23}$$

Now we are going to use the general solution of the paraxial wave equation presented before with combination of the boundary condition

$$E(\boldsymbol{r}_\perp,t)=E(0,t)e^{-\frac{r^2}{w_0^2}}, \tag{2.24}$$

with $r=|\boldsymbol{r}_\perp|$. This corresponds to the spatially localized radiation source with Gaussian intensity profile. Es a result we obtain the TEM_{00} mode with

$$a(\boldsymbol{r},\omega)=\frac{w_0}{w(z,\omega)}^{-\frac{r^2}{w^2(z,\omega)}}, \tag{2.25}$$

$$\varphi(\boldsymbol{r},\omega)=\frac{\omega}{c}z-\tan^{-1}\left(\frac{z}{z_0(\omega)}\right)+\frac{\omega r^2}{2cR(z,\omega)}. \tag{2.26}$$

In the extreme case of $\hat{p}(\omega) \propto \delta(\omega - \omega_0)$ we obtain exactly the same situation es in the previous case (equations (2.7), (2.15)) and the envelope $A(\boldsymbol{r}, t)$ is constant in time. The present situation is more general and we can choose some source spectrum with finite FWHM in order to temporally localize the pulse. Obviously the wider is $\hat{p}(\omega)$ the shorter is the pulse. If $\hat{p}(\omega)$ has Gaussian shape, then the radiation source is Gaussian as well (see (2.16)). So we consider the pulses radiated by the source

$$E(\boldsymbol{r}_\perp, t) \propto e^{-\frac{r^2}{w_0^2}} e^{-\frac{t^2}{b^2}} e^{-i\omega_0 t}, \tag{2.27}$$

where we have introduced the parameter b, which characterizes the temporal width of the source. The propagating radiation and its envelope can be calculated numerically from equations (2.20) and (2.23) respectively. By the parameters $\omega_0 = 3.2$ fs^{-1}, $b = 1.668$ fs and $w_0 = 2$ μm the pulse with only one optical cycle is obtained. The propagation of this pulse is analyzed in detail in [55]. Close to the z-axis the pulse can be well approximated with $e^{(t-z/c)^2/b^2} a(\boldsymbol{r}, \omega_0) e^{i\varphi(\boldsymbol{r},\omega_0)} e^{-i\omega_0 t}$, where all diffraction effects are neglected. That means the pulse maintains its shape and propagates with the speed of light. This fact is important for 1D simulations.

2.2 Laser driven plasma oscillations

After we examined the nature of the ultrashort pulses, we want to pay attention to the theoretical concepts describing the plasma. Further we will consider how plasma interacts with such pulses and with electromagnetic waves in general. In this chapter we will basically orientate on [56] and [57].

2.2.1 Theoretical description of collisionless plasma

One can view a plasma as an ensemble of N charged particles, coupled via electromagnetic interaction. In order to describe such system even by neglecting of magnetic fields and electromagnetic waves we have to solve the system of $6N$

coupled differential equations of the form

$$m_i \ddot{\boldsymbol{r}}_i = q_i \boldsymbol{E}(\boldsymbol{r}_i), \tag{2.28}$$

$$\boldsymbol{E}(\boldsymbol{r}_i) = \sum_j \frac{q_j}{|\boldsymbol{r}_i - \boldsymbol{r}_j|^3}(\boldsymbol{r}_i - \boldsymbol{r}_j), \tag{2.29}$$

where m_i, q_i and $\boldsymbol{r}_i$ are the mass, charge and position of the particle denoted by the subscript i and $\boldsymbol{E}$ is the electric field. This is obviously not optimal approach for systems with large number of particles. One can show that we may assume the collisionless plasma for the large number of electrons in a Debye sphere $N_D = \frac{4}{3}\pi n \lambda_{De}^3$, with the electron density n and the electron Debye length λ_{De}^3. This is a good assumption for many cases being investigated in plasma physics. By this assumption the charged particles exhibit collective behavior. The central relation which describes a collisionless plasma is the Vlasov equation:

$$\frac{\partial f_j}{\partial t} + \boldsymbol{v} \cdot \frac{\partial f_j}{\partial \boldsymbol{r}} + \frac{q_j}{m_j}\left(\boldsymbol{E} + \frac{\boldsymbol{v} \times \boldsymbol{B}}{c}\right) \cdot \frac{\partial f_i}{\partial \boldsymbol{v}} = 0. \tag{2.30}$$

Here we have introduced the phase space distribution function $f_j(\boldsymbol{r}, \boldsymbol{v}, t)$ of j-th particle specie. This equation follows from the continuity equation since the particle conservation is assumed. By averaging over the velocities we obtain such important quantities like the density, the mean velocity and the pressure tensor via

$$n = \int f(\boldsymbol{r}, \boldsymbol{v}, t) d\boldsymbol{v}, \tag{2.31}$$

$$n\boldsymbol{u} = \int \boldsymbol{v} f(\boldsymbol{r}, \boldsymbol{v}, t) d\boldsymbol{v}, \tag{2.32}$$

$$\boldsymbol{P} = m \int (\boldsymbol{v} - \boldsymbol{u})(\boldsymbol{v} - \boldsymbol{u})^T f(\boldsymbol{r}, \boldsymbol{v}, t) d\boldsymbol{v}. \tag{2.33}$$

Here are n, $\boldsymbol{u}$ and $\boldsymbol{P}$ the electron density, mean velocity and pressure tensor respectively. We have also dropped the subscript j since we will consider only electrons further, assuming that the ions are at rest. Now we are going to insert the Vlasov equation in the equations (2.31) and (2.32). We obtain the continuity equation for the density

$$\frac{\partial n}{\partial t} + \frac{\partial}{\partial \boldsymbol{r}} \cdot (n\boldsymbol{u}) = 0 \tag{2.34}$$

and the equation of motion for the charged fluid

$$\frac{\partial}{\partial t}(n\boldsymbol{u}) + \frac{\partial}{\partial \boldsymbol{r}} \cdot (n\boldsymbol{u}\boldsymbol{u}^T) = \frac{nq}{m}\left(\boldsymbol{E} + \frac{\boldsymbol{u} \times \boldsymbol{B}}{c}\right) - \frac{1}{m}\frac{\partial p}{\partial \boldsymbol{r}} \tag{2.35}$$

respectively. In order to obtain the last equation we also set $\boldsymbol{P} = \boldsymbol{I}p$ with the unit dyad $\boldsymbol{I}$. In similar way we also calculate an equation of the pressure from

$$\int \frac{1}{2}mv^2 \left(\frac{\partial f}{\partial t} + \boldsymbol{v} \cdot \frac{\partial f}{\partial \boldsymbol{r}} + \frac{q}{m}\left(\boldsymbol{E} + \frac{\boldsymbol{v} \times \boldsymbol{B}}{c}\right) \cdot \frac{\partial f}{\partial \boldsymbol{v}}\right) d\boldsymbol{v} = 0. \tag{2.36}$$

In one dimensional case we obtain

$$\frac{\partial p}{\partial t} + u\frac{\partial p}{\partial x} + 3p\frac{\partial u}{\partial x} + 2\frac{\partial Q}{\partial x} = 0, \tag{2.37}$$

with $Q \equiv \frac{1}{2}m\int(v-u)^2 f dv$. On that point we want to restrict our consideration to the case of nearly cold plasma where we can neglect the heat flow. That means we can drop the last term in equation (2.37). The obtained result in combination with continuity equation (2.34) gives

$$\left(\frac{\partial}{\partial t} + u\frac{\partial}{\partial x}\right)\frac{p}{n^3} = 0. \tag{2.38}$$

That means $\frac{p}{n^3} = \text{const}$ along the plasma flow. This equation can be generalized to $\frac{p}{n^\gamma} = \text{const}$, where $\gamma = \frac{2+N}{N}$ and N is the number of degrees of freedom. This relation together with (2.34) and (2.35) gives us full description of a fluid.

2.2.2 Small amplitude fluctuations of the electron density

With the formalism derived above we are able to describe small electron density fluctuations which, lead to plasma oscillations and plasma waves. If we consider only one particular dimension the equations (2.34) and (2.35) simplify to

$$\frac{\partial n}{\partial t} + \frac{\partial}{\partial x}(nu) = 0, \tag{2.39}$$

$$\frac{\partial}{\partial t}(nu) + \frac{\partial}{\partial x}(nu^2) = -\frac{neE}{m} + \frac{neu_\perp B}{mc} - \frac{1}{m}\frac{\partial p}{\partial x}, \tag{2.40}$$

$$\frac{p}{n^3} = \text{const}. \tag{2.41}$$

Here is $u_\perp$ ortogonal to u and to B. We added the third equation in order to complete the equation system. Now let us introduce the small amplitude

perturbations via $n = n_0 + \tilde{n}$, $u = \tilde{u}$, $p = n_0\theta + \tilde{p}$ and $E = \tilde{E}$. Here we use the temperature $\theta = mv^2$. Using the Poisson equation

$$\frac{\partial E}{\partial x} = -4\pi e\left(n - Zn_i\right) \tag{2.42}$$

whih the ion charge Z and neglecting higher perturbation orders it is straight forward to obtain the equation for the amplitude fluctuations

$$\left(\frac{\partial^2}{\partial t^2} - 3v^2\frac{\partial^2}{\partial x^2} + \omega_p^2\right)\tilde{n} = \frac{n_0}{2}\frac{\partial^2 u_\perp^2}{\partial x^2}, \tag{2.43}$$

with the electron plasma frequency

$$\omega_p = \sqrt{\frac{4\pi e^2 n}{m}}. \tag{2.44}$$

If we consider a could plasma, the thermal velocity v can be neglected and we obtain simple relation

$$\left(\frac{\partial^2}{\partial t^2} + \omega_p^2\right)\tilde{n} = \frac{n_0}{2}\frac{\partial^2 u_\perp^2}{\partial x^2}, \tag{2.45}$$

so the density harmonically oscillates with frequency ω_p.

2.2.3 Ponderomotive force

We consider a linearly polarized electromagnetic wave which interacts with the plasma electrons, since the Ions are assumed to be at rest. The general equation of the Lorenz force is

$$\frac{d\boldsymbol{p}}{dt} = -e\left(\boldsymbol{E} + \frac{\boldsymbol{u}\times\boldsymbol{B}}{c}\right). \tag{2.46}$$

The fields are given by

$$\boldsymbol{E} = -\frac{1}{c}\frac{\partial \boldsymbol{A}}{\partial t}, \qquad \boldsymbol{B} = \nabla\times\boldsymbol{A}, \tag{2.47}$$

where $\boldsymbol{A}$ is a vector potential that characterizes the electromagnetic field. We also define a normalized vector potential $\boldsymbol{a}$ via

$$\boldsymbol{a} = \frac{e\boldsymbol{A}}{mc^2}. \tag{2.48}$$

In the limit $|\boldsymbol{a}| \ll 1$ we can write $\boldsymbol{p} = \boldsymbol{p}_q + \tilde{\boldsymbol{p}}$, with the quiver momentum $\boldsymbol{p}_q$ defined by

$$\frac{\partial \boldsymbol{p}_q}{\partial t} = -e\boldsymbol{E}. \tag{2.49}$$

This equation describes the respond of the electron fluid on the electric field and thus the electrons oscillate with the frequency of electromagnetic wave (laser). This is first order electron fluid motion. We are going to calculate the second order motion, which is more interesting. We start with

$$\frac{d\tilde{\boldsymbol{p}}}{dt} = \frac{d\boldsymbol{p}}{dt} - \frac{d\boldsymbol{p}_q}{dt}, \tag{2.50}$$

$$= -mc\left(\boldsymbol{u} \times \nabla \times \boldsymbol{a}\right) - mc\left(\boldsymbol{u} \cdot \nabla\right)\boldsymbol{a}. \tag{2.51}$$

Here we have used eqs. (2.46) to (2.49) es well as the operator $\frac{d}{dt} = \frac{\partial}{\partial t} + (\boldsymbol{u}\cdot\nabla)$. To obtain the second order it is enough to set $\boldsymbol{u} = \boldsymbol{p}_q/m$. Using well known relations of vector analysis we obtain

$$\frac{d\tilde{\boldsymbol{p}}}{dt} = -\frac{1}{2}mc^2\nabla a^2. \tag{2.52}$$

This expression represents the ponderomotive force. In one dimensional consideration this force is represented via

$$F_p = \frac{1}{2}m\frac{\partial u_\perp^2}{\partial x}. \tag{2.53}$$

This force is responsible for the electron oscillations in the linear regime (compare with eq. (2.45)). For example by normal incidence of linear polarized laser pulse on plasma surface the ponderomotive force pushes electrons inside the plasma away from boundary.

2.2.4 Wave breaking

The previous description is valued only for small perturbations by $a \ll 1$. In this case the electron density end the corresponding wake field (electric field waked by the density oscillations) oscillate harmonically like a sinus function. However the situation changes as soon as the laser intensity increases. In order to have an idea how the wake field looks like for larger perturbations ($a \sim 1$) we follow the Ref. [58] and consider a simple model of plasma electron plane oscillations. We assume that all electrons behave in the same way along the y- and z-axis, so

we consider only the motion along the x-axis. First, we define the equilibrium position x_0 and the displacement from the equilibrium $X(x_0)$. The position of an electron is then given by

$$x = x_0 + X(x_0). \tag{2.54}$$

Further we assume that the ordering of the electrons in x-direction remains unchanged. So if some electron moves from x_0 to x, we have a gain of the positive charge enX on the left hand side from the electron and the gain of the negative charge on the right hand side. By integrating of the Poisson eq. (2.42) we obtain the wake field

$$E = 4\pi enX. \tag{2.55}$$

Furthermore we can write the equation of motion for the electron

$$m\frac{d^2X}{dt^2} = -eE = -4\pi e^2 nX, \tag{2.56}$$

$$\frac{d^2X}{dt^2} = -\omega_p^2 X. \tag{2.57}$$

It is not surprising that the last equation is similar to eq. (2.45). The general solution of this equation of motion is given by

$$X(x_0) = X_1(x_0)\sin(\omega_p t) + X_2(x_0)\cos(\omega_p t). \tag{2.58}$$

The functions X_1 and X_2 are the arbitrary functions of x_0. The common example of a plasma wave is obtained if we set

$$X_1 = 0 \quad \text{and} \quad X_2 = A\sin kx_0. \tag{2.59}$$

Now we want to analyze the spatial distribution of the wake field and set $t = 0$. We obtain:

$$X = A\sin kx_0, \tag{2.60}$$

$$E = 4\pi enA\sin kx_0, \tag{2.61}$$

$$x = x_0 + X = x_0 + A\sin kx_0. \tag{2.62}$$

In order to obtain the wake field as a function of x we need to eliminate x_0 using last two equations. Since it is impossible to do it analytically, we still can solve this problem numerically. Some examples for different amplitudes A are shown

in Fig. 2.4. As we see for small amplitudes the field has the sine form that

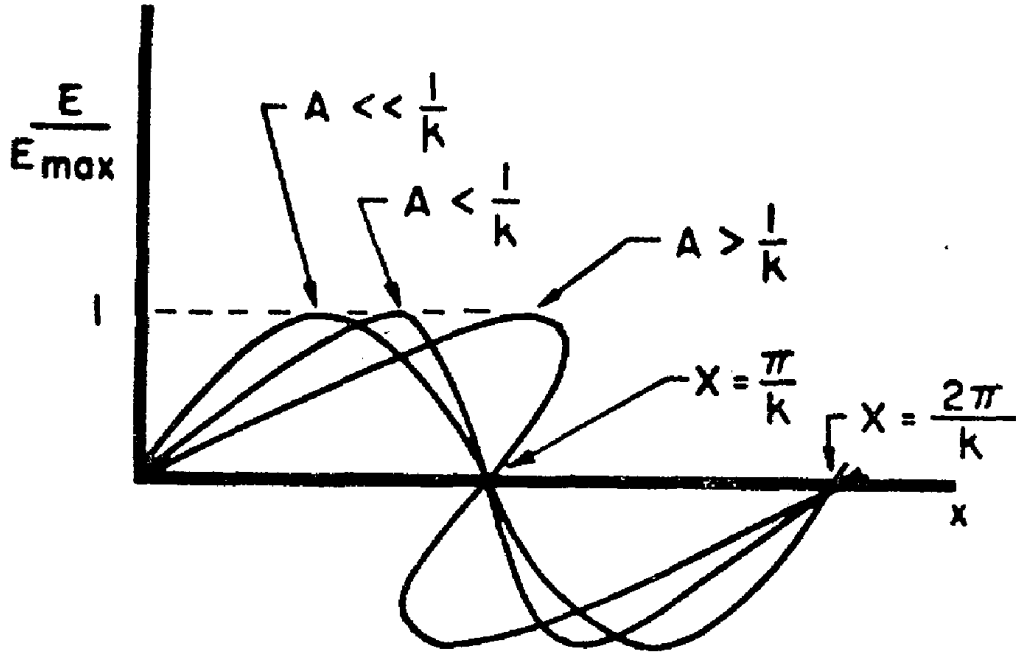

Figure 2.4: (Taken from [58]) Normalized wake field as a function of position x for different values of the amplitude A.

corresponds to the case of small density perturbations. As soon as the amplitude increases the maximum and the minimum of the field move towards each other and coincide for $A = \frac{1}{k}$. For greater values of A we obtain the solutions which are physically forbidden. This means that for the amplitudes greater than $1/k$ the assumption of the electrons unchanged ordering fails and we observe the case of wave breaking. Let us have a look on an example of the density distribution in case of the moderate amplitude $A < \frac{1}{k}$ (Fig. 2.5). As soon as the amplitude increases the density exhibits high spikes between the corresponding extreme values of the wake field. In the critical case of wave breaking the density tends to infinity. If we assume that the electrons oscillate with the wave number $k = \omega_p/c$, then we obtain the wave breaking field

$$E_{WB} = \frac{cm\omega_p}{e}. \tag{2.63}$$

This expression results from equation (2.61) if we set $A = \frac{1}{k} = \frac{c}{\omega_p}$.

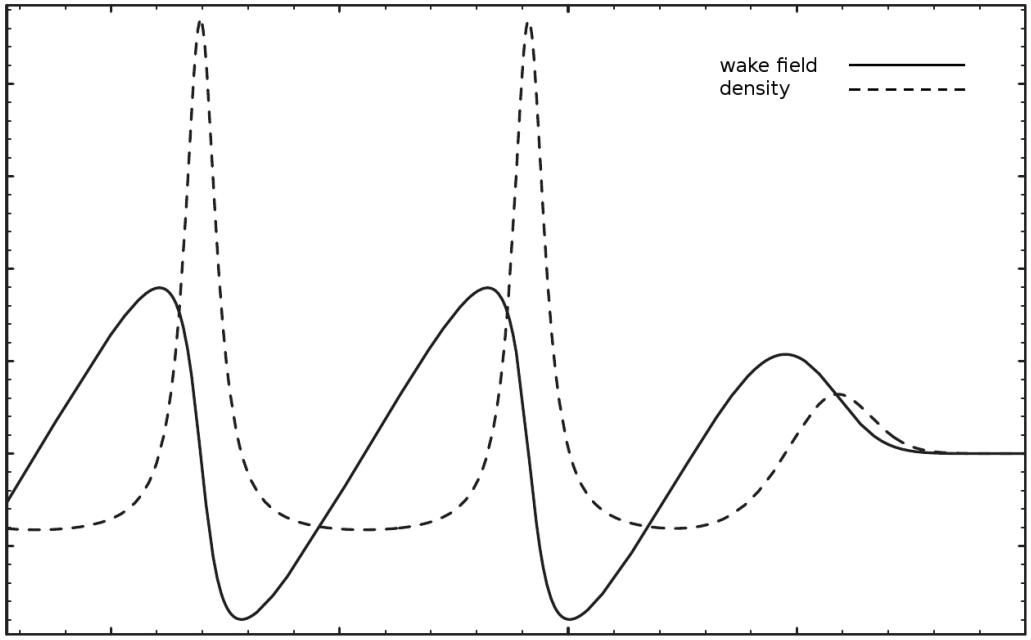

Figure 2.5: (Taken from [57]) Wake field and corresponding density distribution as a function of position x.

2.3 Radiation from perturbed plasma

An oscillating plasma driven by a laser radiates electromagnetic waves. In this section we will derive the expressions allowing us to calculate fields radiated from the perturbed plasma.

2.3.1 Inhomogeneous wave equation

At the beginning of this chapter we have derived the simple wave equation for the electric field in absence of charges and currents starting from Maxwell equations. Now we allow a current distribution $J(\boldsymbol{r}, t)$ in the perturbed plasma. Again, we start from the Maxwell equations

$$\nabla \times \boldsymbol{E} + \frac{1}{c}\frac{\partial}{\partial t}\boldsymbol{B} = 0, \qquad \nabla \cdot \boldsymbol{B} = 0, \tag{2.64}$$

$$\nabla \times \boldsymbol{B} - \frac{1}{c}\frac{\partial}{\partial t}\boldsymbol{E} = \frac{4\pi}{c}\boldsymbol{J}, \qquad \nabla \cdot \boldsymbol{E} = 4\pi\rho. \tag{2.65}$$

Using the Coulomb gauge $\nabla \cdot \boldsymbol{A} = 0$ for the vector potential defined by $\boldsymbol{B} = \nabla \times \boldsymbol{A}$ we obtain the well known wave equation

$$\Delta \boldsymbol{A}(\boldsymbol{r}, t) - \frac{1}{c^2} \frac{\partial^2}{\partial t^2} \boldsymbol{A}(\boldsymbol{r}, t) = -\frac{4\pi}{c} \boldsymbol{J}_\perp(\boldsymbol{r}, t), \tag{2.66}$$

where $\boldsymbol{J}_\perp$ denotes the transverse current given by $\boldsymbol{J}_\perp = \boldsymbol{J} - \frac{1}{4\pi} \nabla \frac{\partial}{\partial t} \varphi$ and serves as a radiation source. In one dimensional geometry this equation takes the form

$$\frac{\partial^2}{\partial x^2} \boldsymbol{A}(x, t) - \frac{1}{c^2} \frac{\partial^2}{\partial t^2} \boldsymbol{A}(x, t) = -\frac{4\pi}{c} \boldsymbol{J}_\perp(x, t). \tag{2.67}$$

In order to solve this equation we are going to find the Green's function G which depends on (x, x', t, t') and satisfy

$$\left(\frac{\partial^2}{\partial x^2} - \frac{1}{c^2} \frac{\partial^2}{\partial t^2} \right) G(x, t, x', t') = -\frac{4\pi}{c} \delta(x - x') \delta(t - t'). \tag{2.68}$$

In absence of boundaries the vector potential is given via

$$\boldsymbol{A}(x, t) = \iint G(x, t, x', t') \boldsymbol{J}_\perp(x', t') dx' dt'. \tag{2.69}$$

In order to find a particular solution of equation (2.68) we need to define some boundary conditions, which make sense form physical point of view. Thus, we set

$$G|_{t=t'} = \left. \frac{\partial G}{\partial t} \right|_{t=t'} = 0, \tag{2.70}$$

$$G|_{x \to \pm\infty} = \left. \frac{\partial G}{\partial t} \right|_{x \to \pm\infty} = 0. \tag{2.71}$$

Physically that means that the source starts to radiate for $t > t'$ and the radiation vanishes at the certain time if the distance from the source goes to infinity. Further we substitute $\tau \equiv t - t'$ and $\mathrm{x} \equiv x - x'$, so the equation (2.68) takes the form

$$\left(\frac{\partial^2}{\partial \mathrm{x}^2} - \frac{1}{c^2} \frac{\partial^2}{\partial \tau^2} \right) G(\mathrm{x}, \tau) = -\frac{4\pi}{c} \delta(\mathrm{x}) \delta(\tau). \tag{2.72}$$

To solve equation (2.72) we will use the method described in [59]. First, we apply the Laplace transformation on bough sides of equation (2.72) and write

$$\int_0^\infty \left(\frac{\partial^2}{\partial \mathrm{x}^2} - \frac{1}{c^2}\frac{\partial^2}{\partial \tau^2}\right) G(\mathrm{x},\tau)e^{-s\tau}d\tau = -\frac{4\pi}{c}\delta(\mathrm{x})\int_0^\infty \delta(\tau)e^{-s\tau}d\tau. \tag{2.73}$$

The integration of each term combined with boundary conditions (2.70) gives

$$\left(\frac{\partial^2}{\partial \mathrm{x}^2} - \frac{s^2}{c^2}\right) g(\mathrm{x},s) = -\frac{4\pi}{c}\delta(\mathrm{x}), \text{ with } g(\mathrm{x},s) = \int_0^\infty G(\mathrm{x},\tau)e^{-s\tau}d\tau. \tag{2.74}$$

The next step is to take the Fourier transform with respect to x of each term in equation (2.74)

$$\int_{-\infty}^\infty \left(\frac{\partial^2}{\partial \mathrm{x}^2} - \frac{s^2}{c^2}\right) g(\mathrm{x},s)e^{ik\mathrm{x}}d\mathrm{x} = -\frac{4\pi}{c}. \tag{2.75}$$

Performing the similar calculations as above and using (2.71) we end up with the simple equation

$$\left(-k^2 - \frac{s^2}{c^2}\right)\hat{g}(k,s) = -\frac{4\pi}{c}, \text{ with } \hat{g}(k,s) = \int_{-\infty}^\infty g(\mathrm{x},s)e^{ik\mathrm{x}}d\mathrm{x}. \tag{2.76}$$

Finally we obtain the expression for the double transformed function

$$\hat{g}(k,s) = \frac{4\pi c}{c^2k^2 + s^2}. \tag{2.77}$$

Further we have to perform two inverse transformations to obtain $G(\mathrm{x},\tau)$. First, we perform the Fourier inversion

$$g(\mathrm{x},s) = \frac{1}{2\pi}\int_{-\infty}^\infty \frac{4\pi c}{c^2k^2 + s^2}e^{-ik\mathrm{x}}dk \tag{2.78}$$

$$= \frac{2}{c}\int_{-\infty}^\infty \frac{1}{k^2 + \frac{s^2}{c^2}}e^{-ik\mathrm{x}}dk \tag{2.79}$$

$$= \frac{2\pi}{s}e^{-\frac{s}{c}|x|}. \tag{2.80}$$

In the last equation we used the table of Fourier transform pairs from [60]. The last step is the Laplace inversion of $g(\mathrm{x},s)$

$$G(\mathrm{x},\tau) = \frac{1}{2\pi i}\int_{\gamma-i\infty}^{\gamma+i\infty} g(\mathrm{x},s)e^{s\tau}ds, \tag{2.81}$$

where γ is a real constant that exceeds the real part of all the singularities of $g(\mathrm{x}, s)$. Using the table of Laplace transform pairs from [60] we finally obtain

$$G(\mathrm{x}, \tau) = 2\pi\Theta\left(\tau - \frac{|\mathrm{x}|}{c}\right), \tag{2.82}$$

with the Heaviside step function

$$\Theta(x) = \begin{cases} 0 & \text{for} \quad x < 0 \\ 1 & \text{for} \quad x \geq 0. \end{cases} \tag{2.83}$$

The function (2.82) solves the equation (2.72). In order to obtain the solution of (2.68) we just substitute back to initial variables

$$G(x, t, x', t') = 2\pi\Theta\left(t - t' - \frac{|x - x'|}{c}\right). \tag{2.84}$$

Now we can insert this result in (2.69) and obtain

$$\boldsymbol{A}(x, t) = 2\pi \int_{-\infty}^{\infty} \int_{-\infty}^{t - \frac{|x-x'|}{c}} \boldsymbol{J}_{\perp}(x', t') dt' dx'. \tag{2.85}$$

The radiated electric field is related to the vector potential via

$$\boldsymbol{E}(x, t) = -\frac{1}{c}\frac{\partial}{\partial t}\boldsymbol{A}(x, t). \tag{2.86}$$

Together with (2.85) this leads to

$$\boldsymbol{E}(x, t) = -\frac{2\pi}{c} \int \boldsymbol{J}_{\perp}\left(x', t - \frac{|x - x'|}{c}\right) dx'. \tag{2.87}$$

So the result is basically the spatial integral over the current distribution taken at the retarded time $t_{\mathrm{ret}} = t - \frac{|x-x'|}{c}$. Using the retarded time we take in to account the time that the wave needs to revel from the curtain source point x' to the observation point x. One can distinguish the radiation coming from the left $\boldsymbol{E}_{\mathrm{left}}$ and from the right $\boldsymbol{E}_{\mathrm{right}}$

$$\boldsymbol{E}_{\mathrm{left}}(x, t) = -\frac{2\pi}{c} \int_{-\infty}^{x} \boldsymbol{J}_{\perp}\left(x', t - \frac{x - x'}{c}\right) dx', \tag{2.88}$$

$$\boldsymbol{E}_{\mathrm{right}}(x, t) = -\frac{2\pi}{c} \int_{x}^{\infty} \boldsymbol{J}_{\perp}\left(x', t - \frac{x' - x}{c}\right) dx'. \tag{2.89}$$

This equations tells that the field at the curtain point x results from superposition of all the waves generated by the given current distribution and arrive x at the time t. So this description can be applied to describe the radiation from the cold collisionless plasma. A wave generated at the curtain point x' inside the plasma can propagate unchanged through the remaining plasma. Let us consider a localized plasma with the boundaries x_1 and x_2 irradiated by some laser pulse coming from the left. We assume that the laser radiation field $E_{\text{laser}}(x,t)$ is fully determined. The fields in front and at the rear side of the plasma are given by

$$\boldsymbol{E}_{x>x_2}(x,t) = -\frac{2\pi}{c}\int_{x_1}^{x_2} \boldsymbol{J}_\perp\left(x', t - \frac{x-x'}{c}\right) dx' + \boldsymbol{E}_{\text{laser}}(x,t), \tag{2.90}$$

$$\boldsymbol{E}_{x<x_1}(x,t) = -\frac{2\pi}{c}\int_{x_1}^{x_2} \boldsymbol{J}_\perp\left(x', t - \frac{x'-x}{c}\right) dx' + \boldsymbol{E}_{\text{laser}}(x,t). \tag{2.91}$$

Equation (2.91) is just the sum of the radiation reflected from the plasma coming from the right and the remaining laser radiation coming from the left. Similar equation (2.90) is an expression for the transmitted radiation.

2.3.2 Transverse electric field in plasma

Now we are interested in behavior of the electric field inside the plasma after the incident wave arrives at the plasma boundary and assume that there are no currents in plasma before it happens. Let us start with the Maxwell eqs. (2.64) and (2.65) again and assume $\nabla \cdot \boldsymbol{E} = 0$. Eliminating the term $\frac{1}{c}\frac{\partial}{\partial t}\nabla \times \boldsymbol{B}$ and using vector analysis we obtain

$$\Delta \boldsymbol{E} = \frac{1}{c^2}\frac{\partial}{\partial t}\left(4\pi \boldsymbol{J} + \frac{\partial}{\partial t}\boldsymbol{E}\right). \tag{2.92}$$

Using the relation $\frac{\partial}{\partial t}\boldsymbol{J} = ne\frac{\partial \boldsymbol{u}}{\partial t} = \frac{ne^2}{m}\boldsymbol{E}$ and $\boldsymbol{E} \propto e^{-i\omega t}$ we get

$$\frac{\partial^2}{\partial x^2}\boldsymbol{E}(x,t) - \frac{\omega_p^2 - \omega^2}{c^2}\boldsymbol{E}(x,t) = 0, \tag{2.93}$$

where we have restricted the analysis to one dimensional case again. Using the boundary condition $\boldsymbol{E}(x_1,t) = \boldsymbol{E}_0 e^{-i\omega t}$ we write the solution $\boldsymbol{E}(x,t) = \boldsymbol{E}_0 e^{i(k(x-x_1)-\omega t)}$ with the dispersion relation

$$k = \frac{1}{c}\sqrt{\omega^2 - \omega_p^2}. \tag{2.94}$$

For high enough plasma density (it will be always the case in further chapters) we have the case $\omega_p > \omega$. Then the wave number is imaginary and the wave does not propagate through the plasma. The solution of equation (2.93) looks like

$$\boldsymbol{E}(x,t) = \boldsymbol{E}_0 e^{-\frac{x-x_1}{\delta}} e^{-i\omega t}, \quad \text{with} \quad \delta = \frac{c}{\omega_p} \frac{1}{\sqrt{1-\frac{\omega^2}{\omega_p^2}}} \tag{2.95}$$

in this case. That means the electric field decays exponentially inside the overdens plasma. If the width $x_2 - x_1$ is sufficiently large there is no transmitted radiation in ideal case. In terms of equation (2.90) that means that the wave originated from the current distribution compensate the incident laser wave on the rear side of the plasma (full reflection).

Chapter 3

Nanobunching regime of high harmonics generation

Authorship claim: The content of this chapter is largely reproduced from my paper [61], which will appear in Physics of Plasmas.

3.1 Simulation set up

For our simulations we use the one-dimensional version of the VLPL PIC code [62]. In our geometry, the incident wave comes from the left hand side of the simulation box and propagates along the x-axis. The wave is p-polarized and the electric field component oscillates along the y-axis. The plasma is located at the right hand side of simulation box. The Code uses dimensionless normalized units. The time and space quantities are normalized to

$$x_{\text{num}} = \frac{x}{\lambda}, \quad t_{\text{num}} = \frac{ct}{\lambda}. \tag{3.1}$$

Here λ denotes the laser wavelength. The numerical Fields are given by

$$\boldsymbol{E}_{\text{num}} = \frac{e\boldsymbol{E}}{mc\omega}, \quad \boldsymbol{B}_{\text{num}} = \frac{e\boldsymbol{B}}{mc\omega}. \tag{3.2}$$

Here is e the elementary charge and ω the laser frequency related to λ as $\omega = 2\pi c/\lambda$. Further important quantities are the electron and current densities. By its normalization we use the critical electron density

$$n_c = \frac{m\omega^2}{4\pi e^2}. \tag{3.3}$$

Then the corresponding normalized densities can be written as

$$n_{\text{num}} = \frac{n}{n_c}, \quad \boldsymbol{J}_{\text{num}} = \frac{\boldsymbol{J}}{n_c c e}. \tag{3.4}$$

It is also possible to simulate oblique incidence with our code. Let θ be the angle of incidence in the laboratory frame and consider a frame moving along the y-axis with velocity $V = c\sin\theta$. Lorentz transformations verify that the laser is normally incident in this frame (see [63] for more details). At the same time the whole plasma moves in y-direction in the frame. Thus, attributing some initial velocity to plasma in our simulation, we are working in the moving frame. If we need to get the results in laboratory frame, we have to transform the values obtained from the simulation via Lorenz transformation. Consequently we obtain results that correspond to the process with oblique incidence (see appendix A for more details).

We use the incident wave $E_i(\tau)$ of duration $T = 10\lambda/c$, that is given by

$$E_i(\tau) = \frac{1}{4}\left(1 + \tanh\left(\frac{\tau}{\Delta t}\right)\right)\left(1 - \tanh\left(\frac{\tau - T}{\Delta t}\right)\right)\sin(2\pi\tau), \tag{3.5}$$

where $\Delta t = \lambda/4$ and $\tau = t - x/c$ (Fig. 3.1a). Further we use an exponential

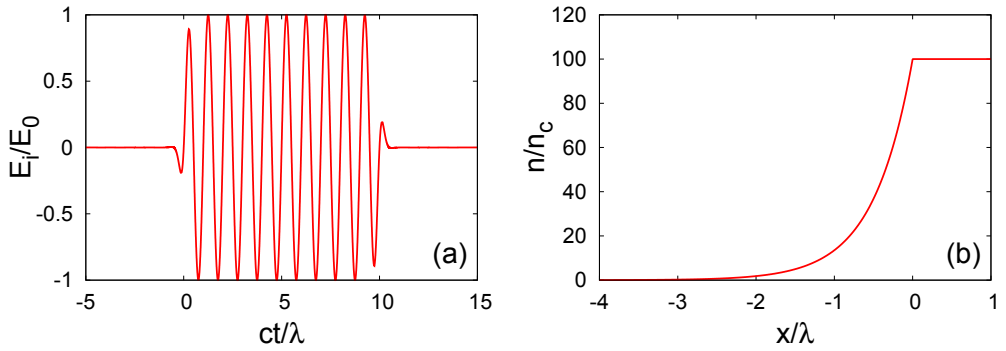

Figure 3.1: (a) Electric field component of the incident electromagnetic wave in vacuum plotted versus time at $x = 0$. (b) Initial density profile $\sigma = 0.5\lambda$, $n_0 = 100n_c$, where n_c is the critical density.

plasma density ramp for $x < 0$. For $x > 0$ the density remains constant (Fig.

3.1b),

$$n(x) = \begin{cases} n_0 e^{\frac{x}{\sigma}} & \text{for} \quad x < 0 \\ n_0 & \text{for} \quad x > 0. \end{cases} \tag{3.6}$$

Assuming that the ions are at rest during the whole interaction process, we consider only the interaction between the electrons and the incident wave. In the simple case of normal incidence there are two forces acting on particles along the x-axis. The electrostatic force proportional to E_x and laser ponderomotive force oscillating with 2ω (twice of the laser frequency). Thus, the plasma surface oscillates with the half of the laser period (Fig. 3.2 (a)). In the case of oblique

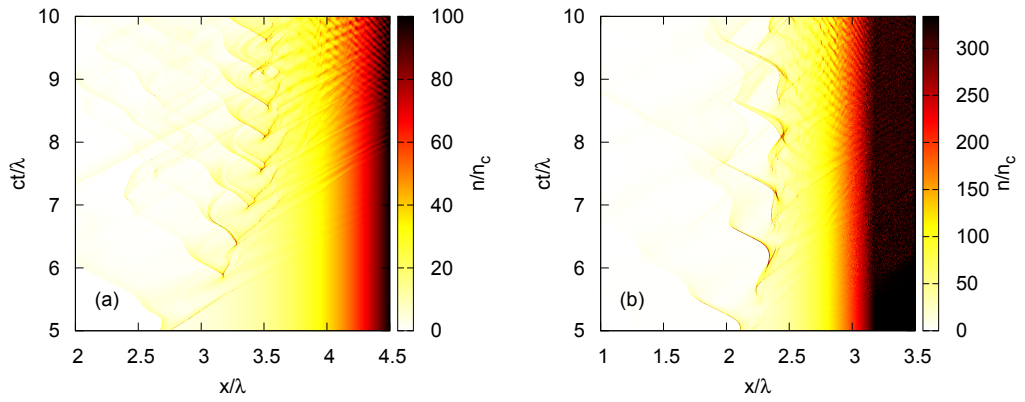

Figure 3.2: The electron density distribution in space time domain by (a) normal incidence and (b) 48° oblique incidence. Simulation parameters considering from the laboratory frame are: plasma density $n_0 = 100n_c$, $\sigma = 0.5\lambda$; laser amplitude $a_0 = 10$. Note that the values in (b) are transformed concerning to the moving frame.

incidence of a p-polarized wave, there is going to be an additional longitudinal component of the electric field oscillating at frequency ω and acting on the plasma surface. Consequently the interaction becomes even more complicated, which leads to stronger oscillations of the plasma surface containing both ω and 2ω modes (Fig. 3.2 (b)).

As soon as the electrons are pulled back by the electrostatic force, they form a thin nanobunch that reaches a velocity close to c. In this case the generation of high-order harmonics is possible.

3.2 Density profile of a thin electron layer

In this section we do the first step towards our first goal described in the introduction and derive two different analytic expressions for two different cases, which roughly describe the electron density profile at the times where the sharp spikes appear. The starting point of our calculations is the approximation of the electron phase space distribution at these times. As we shall see later this distribution depends on the propagation velocity $\dot{x}_0(t)$ of the given electron layer.

First, let us consider the case of a slow electron bunch $\dot{x}_0(t) \ll c$. In Fig. 3.3 the

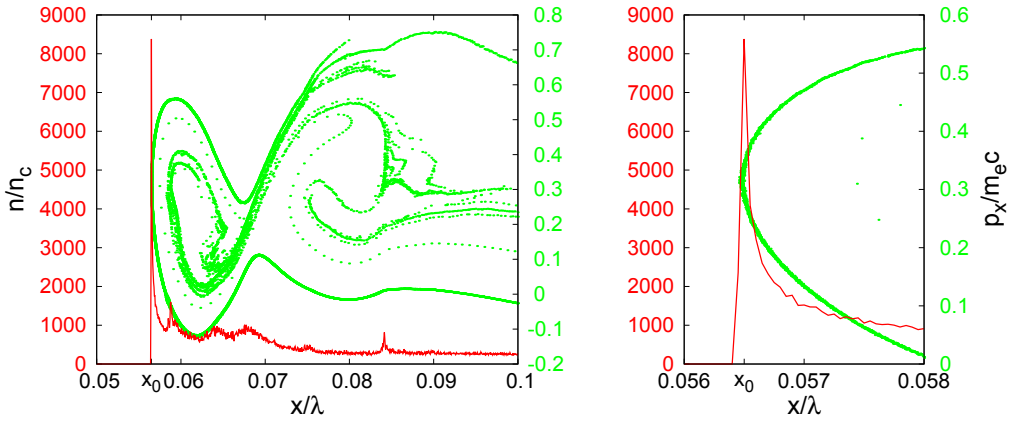

Figure 3.3: Electron density (red) and electrons in x-p_x-plane (green). x_0 is the position of the maximal density. Simulation parameters: initial plasma density $n_0 = 241 n_c$; $\sigma = 0.001\lambda$, Pulse with dimensionless amplitude $a_0 = 10$ and p-polarized oblique incidence at 57° angle has the wave length $\lambda = 820$nm. All magnitudes are taken in the simulation frame. The right picture gives a zoom of the area around x_0.

electron density and its distribution in x-p_x-phase space at time $t = 0.875\lambda/c$, when the electrons are pushed inside the plasma almost to the maximal distance by the ponderomotive force are visualized. We count the time according to Fig. 3.1 (Fig. 3.1a shows the field oscillations at the point $x = 0$ where the region with the constant plasma density begins (Fig. 3.1b)). Because we start with a cold plasma, the electron distribution function is a (curved) line in the phase space. We assume that this curve in phase space is described by the function $x(p)$ at some small interval close to the density spike. Obviously, x_0 is the local minimum of this function that coincides with the position of the spike. In fact, we have always a spike of electron density at the point, where the function $x(p)$ exhibits the local extreme value. For instance, if we take a look at another curve in phase

space, which is enclosed by the previous one, we see that there is also a local maximum of the density at the point were the curve reaches its minimal x-value. However the electrons are more scattered (heated) compared to the previous case and thus the local density maximum is much smaller. The idea, that gives us the staring point for our calculations is the following one. We can locally describe given curve in phase space as a parabola:

$$x(p,t) = x_0(t) + \alpha(t)(p - p_0(t))^2. \tag{3.7}$$

The point $(x_0(t),\ p_0(t))$ corresponds to the local minimum. We consider some short interval Δx where this assumption makes sense. The distribution function of the electrons is given by

$$f(x,p,t) = \mathcal{C}\delta\left(x - x_0(t) - \alpha(t)\left(p - p_0(t)\right)^2\right), \tag{3.8}$$

where $\mathcal{C}$ is a normalization constant. In order to get the expression of density we have to perform the integration in momentum space

$$n(x,t) = \int dp f(x,p,t). \tag{3.9}$$

By using well known integration properties of the Dirac delta function and doing some algebra we obtain the expression

$$n(x,t) = \frac{\mathcal{C}}{\sqrt{\alpha(t)\left(x - x_0(t)\right)}}. \tag{3.10}$$

The detailed derivation of this result is given in appendix A. Note that this equation makes sense only for $x > x_0$. For $x < x_0$ the density has to be zero in this model. This is true because the argument of delta function in (3.8) as the function of p vanishes only for $x > x_0$. In other words, there are no electrons on the left hand side of x_0. In order to calculate the constant $\mathcal{C}$, we initially write an equation for the number of particles in the interval Δx by integrating the density from $x_0(t)$ to $x_0(t) + \Delta x$

$$N_{\Delta x}(t) = \mathcal{C}\int_{x_0(t)}^{x_0(t)+\Delta x} \frac{dx}{\sqrt{\alpha(t)\left(x - x_0(t)\right)}} = 2\mathcal{C}\sqrt{\frac{\Delta x}{\alpha(t)}}. \tag{3.11}$$

We solve the obtained equation for $\mathcal{C}$ and insert it into equation (3.10). Finally, we obtain the expression for the electron density profile,

$$n(x,t) = \frac{1}{2}\frac{N}{\sqrt{\Delta x\,(x - x_0(t))}}, \tag{3.12}$$

where N is the number of particles contained between $x_0(t)$ and $x_0(t) + \Delta x$. Note that the parameter α cancels, so it does not affect the density profile. In Fig.

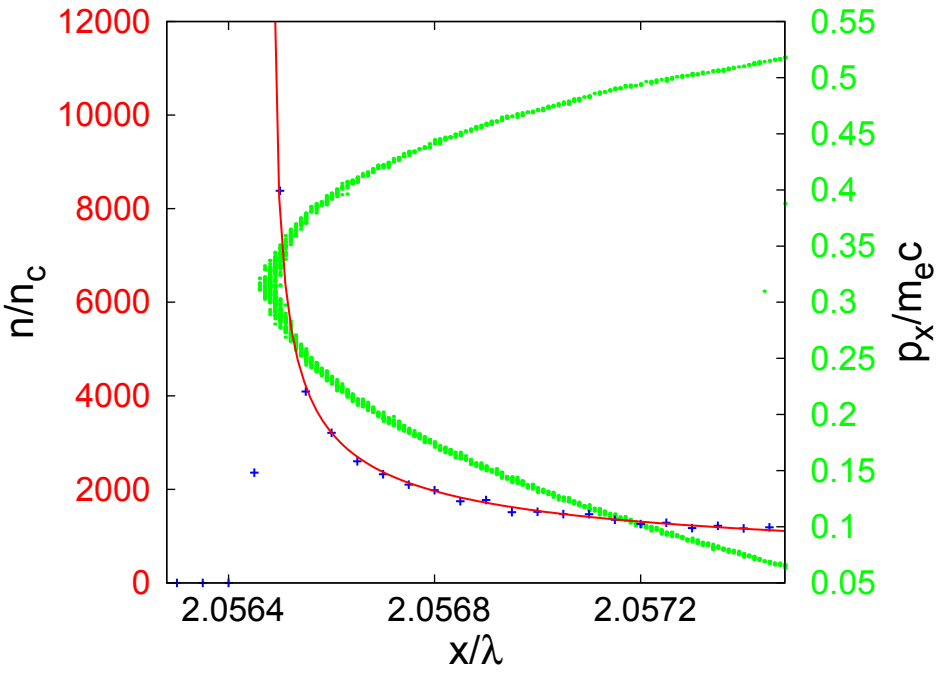

Figure 3.4: Electron density taken from simulation (blue) and calculated analytically via (3.12) (red), as well as electrons in x-p_x-plane (black), with same simulation parameters as for Fig. 3.3, $\Delta x = 0.001\lambda$ (simulation frame).

3.4 we see that the density described with (3.12) agrees very well with simulation results. This picture is actually a zoom of the Fig. 3.3 at the position of density spike. We obtain the best agreement at the instants when the electrons are pushed inside at the maximal distance. In this case, the mean momentum of the electrons is close to zero and equation (3.7) describes electrons in phase space quite well. We call the case where $\dot{x}_0(t) \ll c$ is valid "parabolic case".

Now we discuss another case with $\dot{x}_0(t) \to c$. Consider the phase space evolution taken from the other simulation illustrated in Fig. 3.5. At the beginning, $t = 6.2\lambda/c$, the momentum is close to zero and the distribution is parabolic as

expected. Further, as soon as the electron bunch is pulled back by the electrostatic force, the negative momentum of the bunch grows constantly with time and the distribution changes its form until it becomes a kind of a "whip" between $t = 6.5\lambda/c$ and $t = 6.6\lambda/c$. The extremely dense electron nanobunch reaches the velocity close to c during this period. This picture is taken from the same

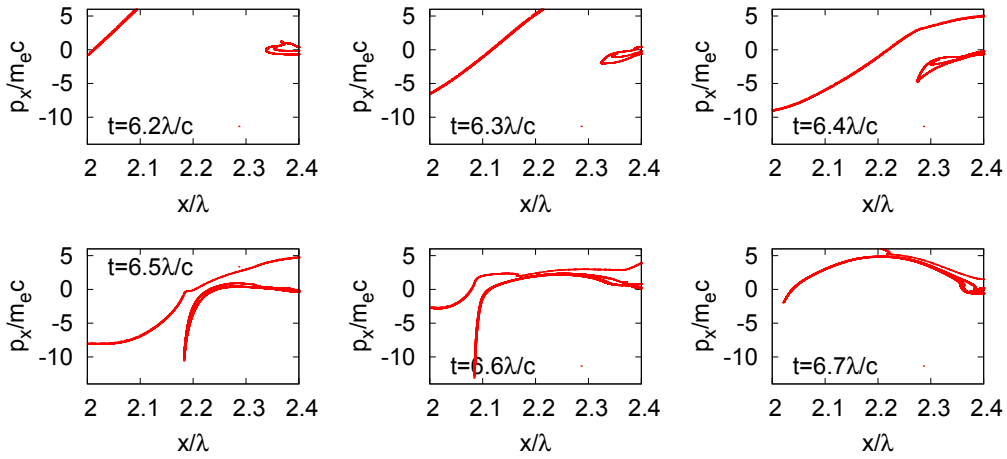

Figure 3.5: Electrons in x-p_x-plane taken from the simulation to different times t during the process of nanobunching. Simulation parameters: initial plasma density $n_0 = 100n_c$; $\sigma = 0.5\lambda$ (laboratory frame), Pulse with dimensionless amplitude $a_0 = 10$ and p-polarized oblique incidence at 48° angle has the wave length $\lambda = 820$nm.

simulation as Fig. 3.2 (b). In this case the phase space distribution can be roughly fitted with an exponential function

$$x_p(p,t) = x_0(t) + e^{\alpha(t)(p-p_0(t))} \tag{3.13}$$

(see Fig. 3.6). As we will show later, the incident angle and the density gradient that were used here are optimal for producing the most intense attosecond pulse. The phase space distribution belongs to the nanobunch that emits this pulse. In order to simplify the notation we drop the time dependence and set $p_0 = x_0 = 0$. At this point we have

$$x_p(p) = e^{\alpha p}, \tag{3.14}$$

and the distribution function:

$$f(x,p) = \mathcal{C}\delta\left(x - x_p(p)\right). \tag{3.15}$$

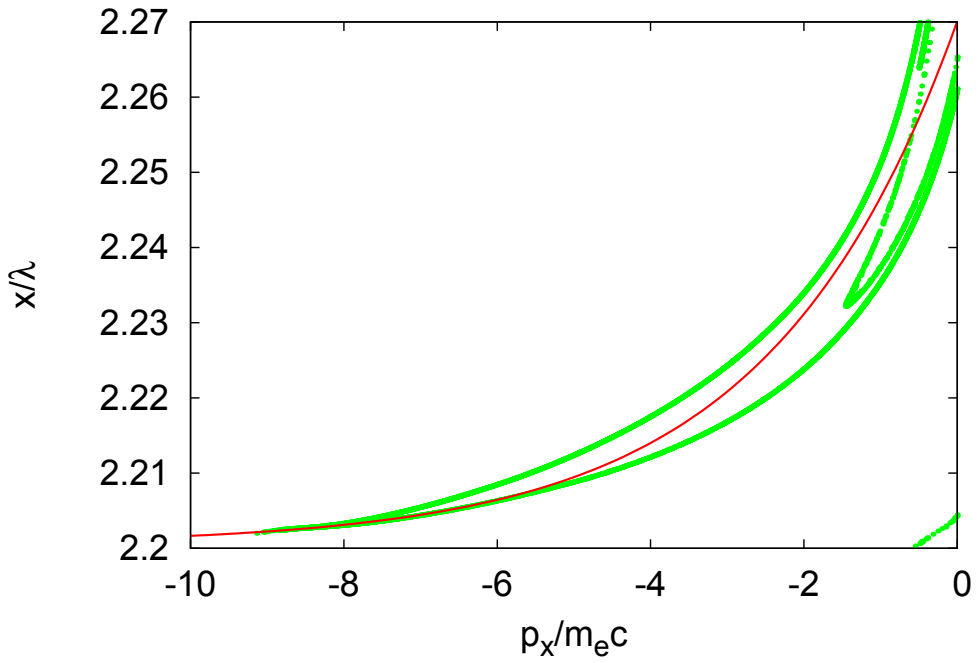

Figure 3.6: Electrons in x-p_x-plane (green) and the exponential fit (red) from the same simulation as Fig. 3.5, taken to the time $t = 6.48\lambda/c$.

Going along the same line as in the previous case, we obtain:

$$n(x) = \mathcal{C} \int dp\ \delta\left(x - x_p(p)\right) = \frac{\mathcal{C}}{\alpha x}. \tag{3.16}$$

See appendix A for more details. Obviously equation (3.14) can not be applied at the whole interval $[0 : \Delta x]$ as in the parabolic case since the momentum of the electrons is limited by some amount p_{cut}. Therefore the description (3.14) is valid only on some interval $[x_{\min} : x_{\max}]$, where $x_{\min} = e^{-\alpha p_{\text{cut}}}$. Strictly speaking by performing the integration in (3.16) we have to take $-p_{\text{cut}}$ as a lower limit, instead of $-\infty$. This would not change the form of the result but the interval on which it is valid, namely for $x > x_{\min}$. Consequently, we integrate the expression (3.16) from $x_{\min}$ to $x_{\max}$ in order to calculate $\mathcal{C}$ and get

$$n(x) = \frac{N}{\ln\left(\frac{x_{\max}}{x_{\min}}\right) x}. \tag{3.17}$$

As we can see from Fig. 3.7 equation (3.17) approximates the density profile quite well even over the comparably long interval. We call the case where $\dot{x}_0(t) \to c$ is

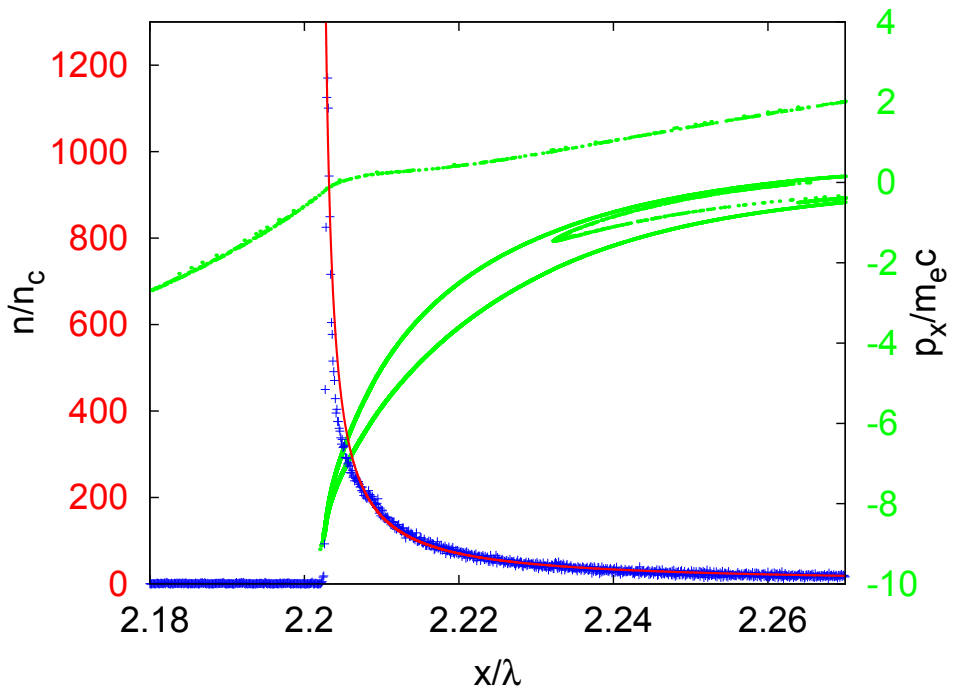

Figure 3.7: Electron density taken from simulation (blue) and calculated analytically via (3.17) (red), as well as electrons in x-p_x-plane (green), with same simulation parameters compared to Fig. 3.5, taken at $t = 6.48\lambda/c$. $x_{\min} - x_0 = 8,5 \cdot 10^{-4}\lambda$; $x_{\max} - x_0 = 0.05\lambda$ (simulation frame).

valid "whip case".

Although the functions (3.12) and (3.17) work well on the given intervals, we still have the problem that they both are not continuous or even exhibit a singularity. Such behavior is obviously not physical. In fact, we are able to describe only a part of the spike correctly. In order to solve this problem we need to find an expression that would describe the whole spike. That means for instance on interval $[x_0 - \Delta x : x_0 + \Delta x]$. In order to find such function we have to replace the delta function, which is used for the definition of the distribution function in equations (3.8) and (3.15) by some limited function $\delta_a(x)$ with the property

$$\lim_{a \to 0} \delta_a(x) = \delta(x). \tag{3.18}$$

The parameter a describes the width of δ_a, which means that $a > 0$ is required. Gaussian function would fulfill these conditions, but if we use it in order to define δ_a we would not be able to solve the integral (3.9) analytically. That's why we

define:

$$g_a(x) \equiv \frac{3}{4a}\left(1 - \frac{x^2}{a^2}\right) \tag{3.19}$$

$$\delta_a(x) \equiv \begin{cases} g_a(x) & \text{for} \quad x \in [-a, a] \\ 0 & \text{otherwise} \end{cases} \tag{3.20}$$

It is easy to check that with this definition $\delta_a(x)$ does satisfy the condition (3.18).

Let us calculate the electron density profile for the parabolic case with $x(p) = \alpha p^2$ again now, which holds if the electron bunch moves slowly. We have:

$$n_a(x) = \mathcal{C} \int dp \; \delta_a\left(x - \alpha p^2\right)) \tag{3.21}$$

This integration is more complicated as for the simple case with the δ-function. We have to be careful with integration boundaries, since δ_a is a bounded support function. As a result we obtain:

$$n_a(x) = \begin{cases} \dfrac{2\mathcal{C}}{5a^3\sqrt{\alpha}}\left(3a^2 - 2x^2 + ax\right)\sqrt{x+a} & \text{for} \quad x \in [-a, a] \\ \dfrac{2\mathcal{C}}{5a^3\sqrt{\alpha}}\Big(\left(3a^2 - 2x^2\right)\left(\sqrt{x+a} - \sqrt{x-a}\right) & \\ \qquad + ax\left(\sqrt{x+a} + \sqrt{x-a}\right)\Big) & \text{for} \quad x > a \\ 0 & \text{for} \quad x < -a \end{cases} \tag{3.22}$$

It is straight forward to show that

$$\lim_{a \to 0} n_a(x) = n(x) = \begin{cases} \dfrac{\mathcal{C}}{\sqrt{\alpha x}} \\ 0 \end{cases}, \tag{3.23}$$

compare with (3.10). For the number of particles $N_{a,\Delta x}$ on the interval $[-a : \Delta x]$, that means

$$N_{a,\Delta x} = 2\mathcal{C}\sqrt{\frac{\Delta x}{\alpha}} \quad \text{for} \quad a \ll \Delta x, \tag{3.24}$$

compare with (3.11). Equation (3.24) follows directly from (3.11) and (3.23) for $a \to 0$. Via integration of $n_a(x)$ on the interval $[-a, \Delta x]$ it can be shown that (3.24) holds also for $a \ll \Delta x$, which is a more general case. Actually we are

always able to chose Δx in such a way that the condition $a \ll \Delta x$ is satisfied and for that case we can finally write

$$n_{a,\Delta x}(x) = \begin{cases} \dfrac{N_{a,\Delta x}}{5a^3\sqrt{\Delta x}} \left(3a^2 - 2x^2 + ax\right) \sqrt{x+a} & \text{for} \quad x \in [-a, a] \\ \dfrac{N_{a,\Delta x}}{5a^3\sqrt{\Delta x}} \Big(\left(3a^2 - 2x^2\right) \left(\sqrt{x+a} - \sqrt{x-a}\right) & \\ \qquad + ax \left(\sqrt{x+a} + \sqrt{x-a}\right) \Big) & \text{for} \quad x > a \\ 0 & \text{for} \quad x < -a. \end{cases} \tag{3.25}$$

Detailed calculation of this result is shifted to appendix A. We plot some examples in order to show how our function looks like for different parameters a (Fig. 3.8 (a)). Now let us fit the simulated density from above with the calculated analytical

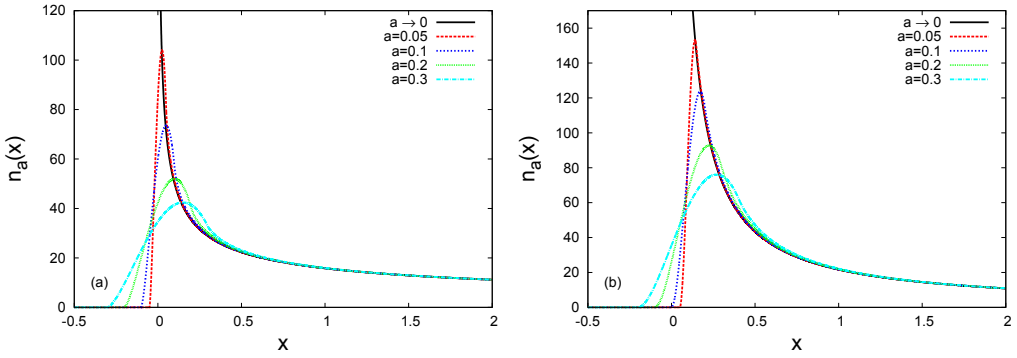

Figure 3.8: example of some analytical density profiles with same $N = 100$, but different a in case (a) $x_p(p) = \alpha p^2$, $\Delta x = 10$ and (b) $x_p(p) = e^{\alpha p}$, $x_{\min} = 0.1$, $x_{\max} = 10$.

profile (Fig. 3.9). We chose a quite small value for a because the plasma is cold and we are dealing with very the big and sharp spike as it is shown in this example. This is the case since we use strong laser pulse and very small cell size ($5 \cdot 10^{-5}\lambda$). As we can see, our function agrees well with the simulated profile.

Of course the generalization $\delta(x) \to \delta_a(x)$ can be also used to calculate the density in the whip case where $x_p(p) = e^{\alpha p}$. But now we have to take p_{cut} as a lower limit by the integration (3.16), since otherwise the integral would diverge for $x \in [x_{\min} - a, x_{\min} + a]$. Doing the same steps as in the previous case, we finally

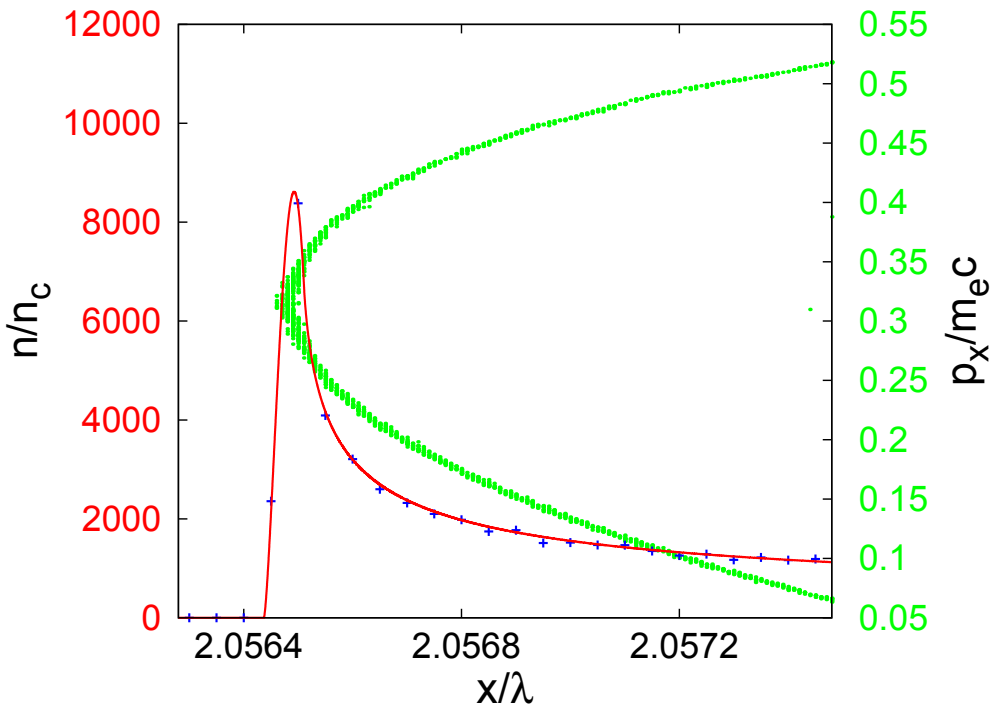

Figure 3.9: Electron density taken from the simulation (blue) and calculated analytically via (3.25) (red), with same simulation parameters as for Fig. 3.3, $\Delta x = 0.001\lambda$; $a = 3,7 \cdot 10^{-5}$ (simulation frame).

obtain the density profile

$$n_a(x) = \begin{cases} \dfrac{3N}{4a^3 \ln\left(\frac{x_{\max}}{x_{\min}}\right)} \left((x+a)\left(x + (x-a)\left(\dfrac{1}{2} + \ln\left(\dfrac{x_{\min}}{x+a}\right)\right)\right) \right. & \\ \left. \qquad + x_{\min}\left(\dfrac{1}{2}x_{\min} - 2x\right)\right) & \text{for} \quad x \in [x_{\min} - a, x_{\min} + a] \\ \dfrac{3N}{4a^3 \ln\left(\frac{x_{\max}}{x_{\min}}\right)} \left(2ax - (x^2 - a^2)\ln\left(\dfrac{x+a}{x-a}\right)\right) & \text{for} \quad x > x_{\min} + a \\ 0 & \text{for} \quad x < x_{\min} - a \end{cases} \tag{3.26}$$

(see appendix A fo more details). Some examples of this function are plotted in Fig. 3.8 (b). Now as in the previous case we are going to compare the calculated analytical function with the simulated density profile (Fig. 3.10). Again we obtain a good agreement and are able to describe the density spike quite well.

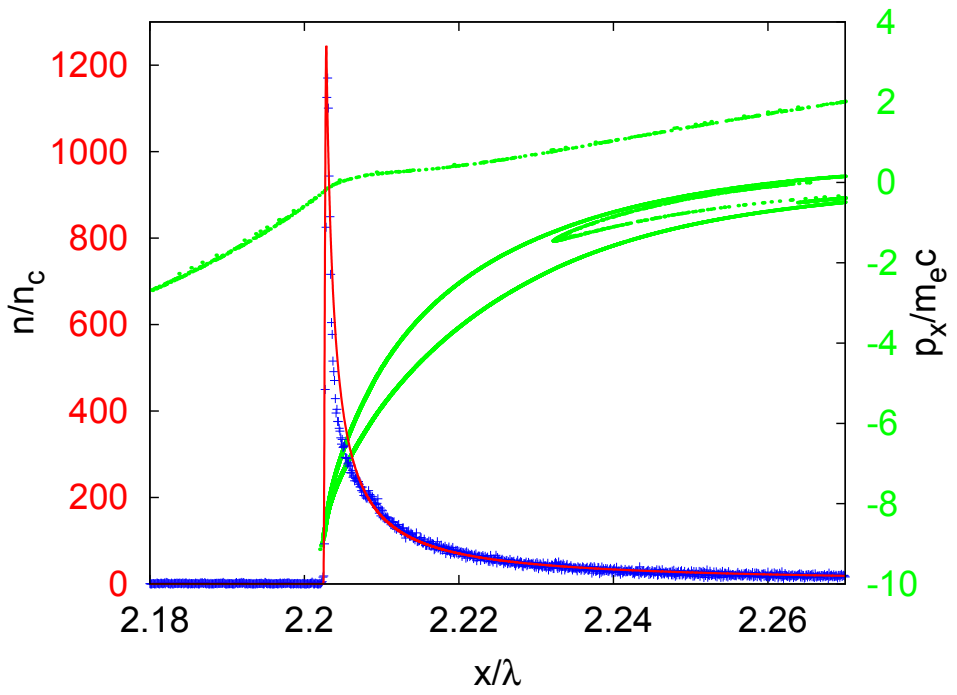

Figure 3.10: Electron density taken from simulation (blue) and calculated analytically via (3.26) (red), as well as electrons in x-p_x-plane (green), with same simulation parameters compared to Fig. 3.5, taken at $t = 6.48\lambda/c$. $x_{\min} - x_0 = 8,5 \cdot 10^{-4}\lambda$; $x_{\max} - x_0 = 0.05\lambda$; $a = 2 \cdot 10^{-4}$ (simulation frame).

Before we go further, we analyze the intermediate case $\dot{x}_0(t) \lesssim c$. In this case, the electron phase space distribution does not have any regular shape and can not be approximated well neither with a parabolic, nor with an exponential function. Two examples of this case are shown in Fig. 3.11 and Fig. 3.12. Nevertheless, we find out that the density profile of the spike can still be well approximated with equation (3.25) (Fig. 3.11, 3.12), so we classify the cases with intermediate velocities as parabolic. Fig. 3.11 is taken from the same simulation as Fig. 3.9 but at the later time.

In the following section we are going to analyze the corresponding simulation results more extensively. We will use the descriptions of the electron density profile derived here in order to calculate an expression for the spectra of the reflected waves in different cases.

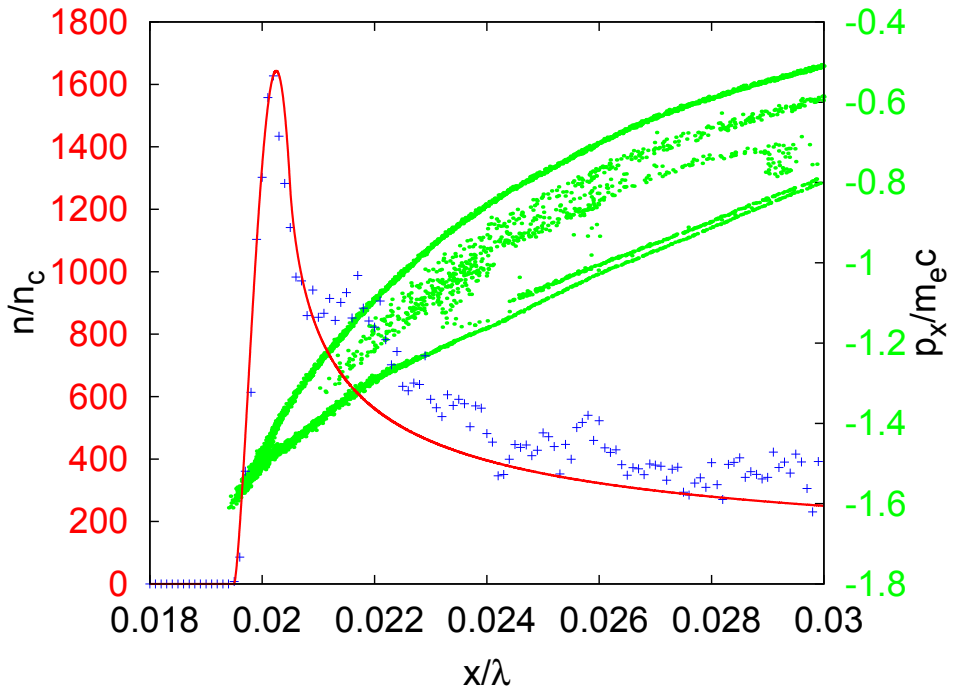

Figure 3.11: Electron density taken from simulation (blue) and calculated analytically via (3.25) (red), as well as electrons in x-p_x-plane (green), with same simulation parameters compared to Fig. 3.3 but to the later time. Parameters of the shape function: $\Delta x = 0.01\lambda$; $a = 5 \cdot 10^{-4}$ (simulation frame).

3.3 Reflected radiation in nanobunching regime

In the previous section, we did the first step towards our aim to improve the analytical description of the spectrum in the case of CSE. We derived two analytic expressions which describe the electron density profile in two different cases during CSE process. In this section we will go further and work out the equations for the transverse current distribution for the corresponding cases, where the expressions derived previously will be used.

We are interested in the high frequency spectrum of the reflected pulse mostly determined by the behavior of the electron nanobunch when it moves away from the plasma with maximal velocity. This moment corresponds to the stationary phase point (SPP) (see [43]). The gamma factor of the bunch exhibits a sharp spike at this time, the so called γ-spike [37]. One distinguishes different orders of γ-spikes depending on behavior of the transverse current (see below).

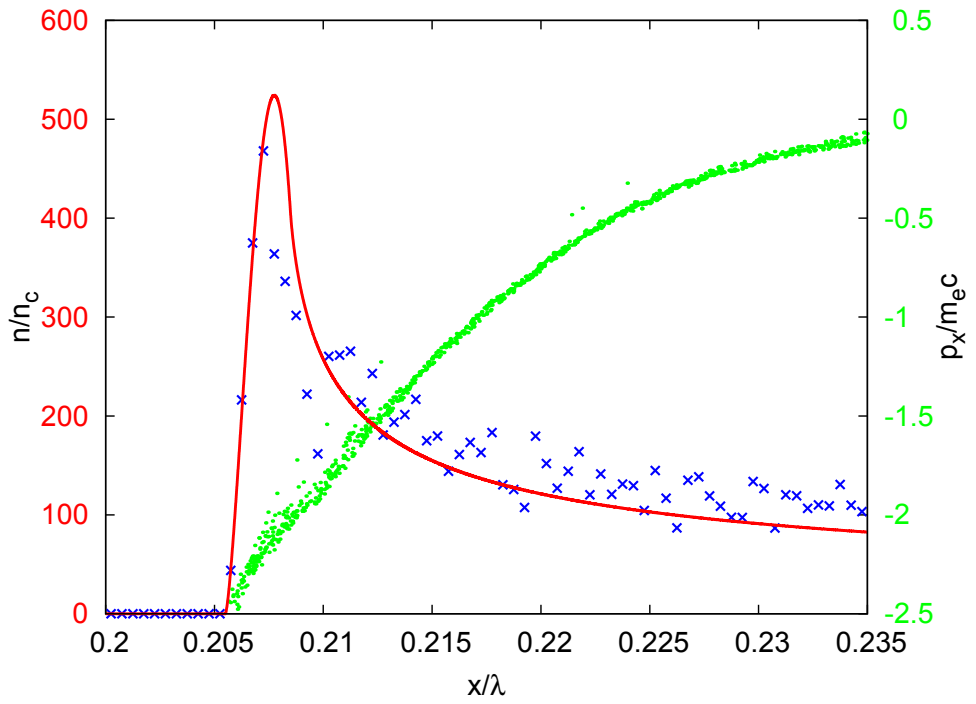

Figure 3.12: Electron density taken from simulation (blue) and calculated analytically via (3.25) (red), as well as electrons in x-p_x-plane (green). Simulation parameters: initial plasma density $n_0 = 100n_c$; $\sigma = 0.066\lambda$ (laboratory frame), Pulse with dimensionless amplitude $a_0 = 10$ and p-polarized oblique incidence at 60° angle has the wave length $\lambda = 820$nm. Parameters of the shape function: $\Delta x = 0.013\lambda$; $a = 1.5 \cdot 10^{-3}$ (simulation frame).

First, we investigate the example of the whip case ($\dot{x}_0(t) \to c$) from the previous section illustrated in Fig. 3.2(b), Fig. 3.5 and Fig. 3.10 more extensively. The reflected wave obtained in this simulation is shown in Fig. 3.13 (a). Since we use a few cycle laser pulse, we get an attosecond pulse train as reflected radiation. In the following, we consider only the most intense reflected pulse $E_r^{\text{pls}}(t)$ that is filtered out by the Gaussian function (Fig. 3.13 (b)), i.e.

$$E_r^{\text{pls}}(t) = E_r(t)e^{(t-t_{\max})^2/\tilde{\sigma}^2}, \tag{3.27}$$

where $t_{\max}$ corresponds to the maximal wave amplitude and $\tilde{\sigma} = 0.2\lambda/c$. The amplitude of the pulse is about five times larger than of incident wave like in the CSE case. The electron nanobunch which radiates this pulse can be clearly recognized from the density distribution shown in Fig. 3.14. For convenience, we chose the coordinates in Fig. 3.14 (b) in such a way that the SPP is in the point

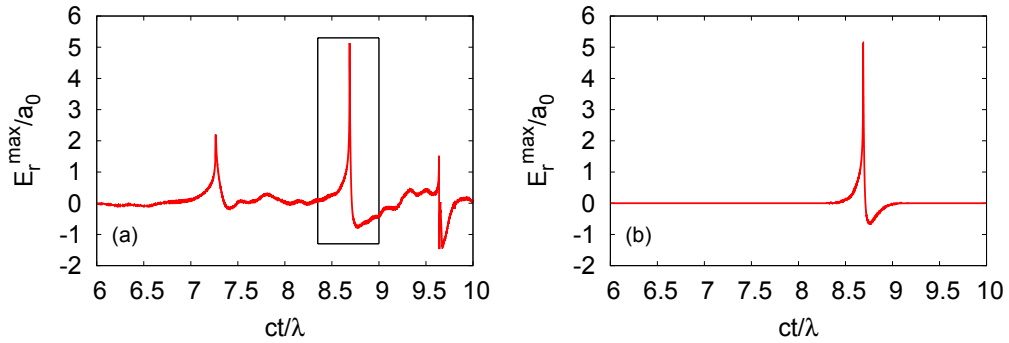

Figure 3.13: (a): Part of the reflected radiation given by $\frac{1}{2}(E_y(t) - B_z(t))$. (b): Single pulse from the reflected pulse train filtered out by the Gaussian function. Simulation parameters are the same as for Fig. 3.5.

(0,0), while in Fig. 3.14 (a) it corresponds to the point (2.16λ, 6.52λ/c). As we saw in chapter 2 the reflected radiation is determined by the transverse current distribution $J_\perp(x,t)$ via

$$E_r(x,t) = -\frac{2\pi}{c}\int_x^\infty J_\perp\left(x', t - \frac{x'-x}{c}\right)dx', \tag{3.28}$$

(since the wave is p-polarized only y-component is considered). For simplicity we translate this equation to normalized PIC units. First, we multiply the space argument in each function with $1/\lambda$ and the time argument with c/λ. Then substitute $x_{\text{num}} = x/\lambda$ in the integral and get

$$E_r(x_{\text{num}}, t_{\text{num}}) = -\frac{2\pi\lambda}{c}\int_{x_{\text{num}}}^\infty J_\perp\left(x'_{\text{num}}, t_{\text{num}} - (x'_{\text{num}} - x_{\text{num}})\right)dx'_{\text{num}}. \tag{3.29}$$

Further, we multiply each side of this equation with the factor $\frac{e}{mc\omega}$ and subsequently use the definition of the critical density in order to simplicity the factor on the right hand side. As a result equation for reflected radiation simplifies to

$$E_r^{\text{num}}(x_{\text{num}}, t_{\text{num}}) = -\pi\int_{x_{\text{num}}}^\infty J_\perp^{\text{num}}\left(x'_{\text{num}}, t_{\text{num}} - (x'_{\text{num}} - x_{\text{num}})\right)dx'_{\text{num}}. \tag{3.30}$$

Now the equation contains purely numerical quantities. We drop the subscript "num" and write

$$E_r(x,t) = -\pi\int_x^\infty J_\perp\left(x', t - (x'-x)\right)dx'. \tag{3.31}$$

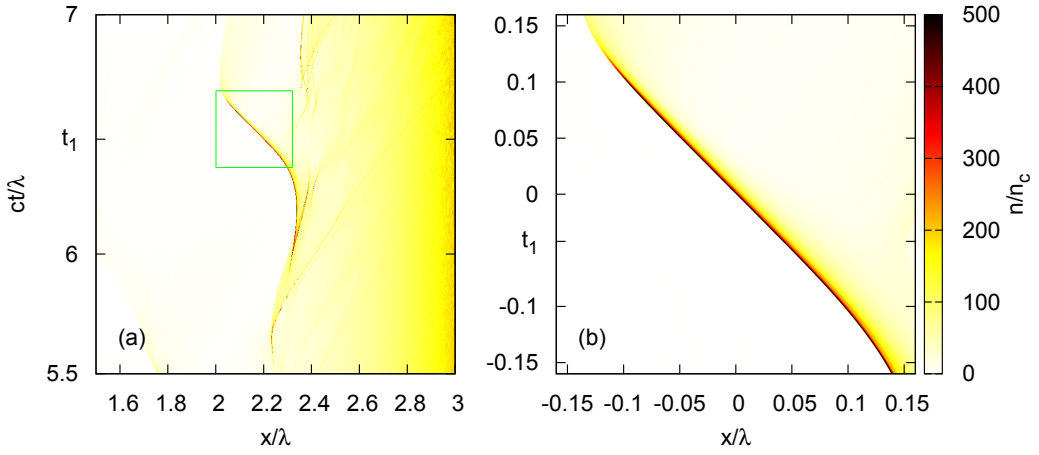

Figure 3.14: The electron density distribution in space time domain. Simulation parameters are the same as for Fig. 3.5. All magnitudes are taken in the simulation frame The green square in (a) marks the nanobunch that is zoomed in (b). This bunch is responsible for the radiation of the strong pulse shown in Fig. 3.13. In (a) $t_1 = 6.48\lambda/c$ as in Fig. 3.10.

After we translated the equation for reflected field to the normalized units we want to simplify this expression further by eliminating the x-dependence, which is not important in our case since we consider the reflected radiation behind the plasma. To do so, we consider the field on at some point (x_0, t_0) with $t_0 = -x_0$ and evaluate the limit

$$\lim_{x_0 \to \infty} E_r(x_0, -x_0) = -\pi \int_{-\infty}^{\infty} J_\perp(x, -x)\, dx. \tag{3.32}$$

Finally, we define

$$E_r(t) \equiv \lim_{x_0 \to \infty} E_r(x_0, -x_0 + t), \tag{3.33}$$

and obtain the simplified expression

$$E_r(t) = -\pi \int_{-\infty}^{\infty} J_\perp(x, t - x)\, dx. \tag{3.34}$$

Starting from this equation we make some assumption of current behavior in the vicinity of the SPP. Our derivation is similar to the one in [43], but is more detailed. First of all, we assume that the transverse current density does not

change its shape during the time and write

$$J_\perp(x,t) = n(x,t)v_\perp(x,t) \approx j(t)f(x - x_0(t)), \tag{3.35}$$

with the density $n(t,x)$, the velocity $v_\perp(t,x)$ and the position of the bunch x_0. The function f is the shape that is assumed to be constant close to the SPP. If we compare the both sides of the last equation in (3.35), we can approximate

$$v_\perp(x,t) \approx \bar{v}_\perp(t), \qquad n(x,t) \approx n_\mathrm{m} f(x - x_0(t)). \tag{3.36}$$

This means that equation (3.35) assumes the transverse velocity being approximately constant in space and equal to the mean velocity $\bar{v}_\perp(t)$. The density profile has a constant shape with the maximal value n_m and only changes its position $x_0(t)$. Thus the equation (3.35) takes the form

$$J_\perp(x,t) \approx n_\mathrm{m}\bar{v}_\perp(t)f(x - x_0(t)), \qquad j(t) = n_\mathrm{m}\bar{v}_\perp(t). \tag{3.37}$$

In the next step, we assume the ultrarelativistic regime, which means that absolute velocity of the particles is always close to c. In this case we can write

$$\sqrt{\dot{x}_0(t)^2 + \bar{v}_\perp(t)^2} \approx v \approx c. \tag{3.38}$$

Now we are going to Taylor expand $j(t)$. Let us first take a look at the Fig. 3.15 (a). It shows the transverse current distribution of the given nanobunch. In the SPP the bunch exhibits maximal longitudinal velocity $v_x = v$ which is close to c, so that the transverse component almost vanish. As a result, the transverse current vanishes as well. This can be seen in the picture. We can also see, that the current does not change its sign at the SPP. So we assume

$$j(t) \approx \alpha_0 t^2. \tag{3.39}$$

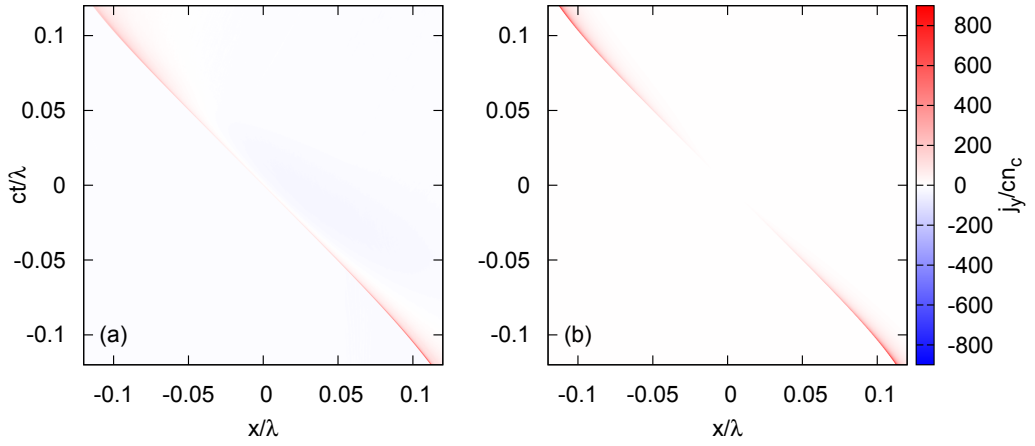

Figure 3.15: Transverse current density from the simulation (a) and calculated analytically (b). In (a) the simulated current density near the SPP (0,0) is illustrated. As we see the transverse current almost vanish in SPP. Simulation parameters are the same compared to Fig. 3.5. In (b) the analytically calculated current distribution is shown. The parameters used in equation (3.41) are: $\alpha_0 = 6 \cdot 10^4$, $n_\mathrm{m} = 1100$ and $\gamma = 15$, while the parameters used for the shape are: $a = 1,5 \cdot 10^{-4}\lambda$, $x_\mathrm{min} = 8 \cdot 10^{-4}\lambda$ and $\tilde{\tilde{\sigma}} = 0.02\lambda$. The velocity υ in (3.41) is obtained from the gamma factor.

Combining this relation with the second equation from (3.37) and inserting it in (3.38) leads to

$$\dot{x}_0(t) \approx -\sqrt{\upsilon^2 - \frac{\alpha_0^2}{n_\mathrm{m}^2} t^4} \approx -\upsilon + \frac{\alpha_0^2}{2\upsilon n_\mathrm{m}^2} t^4, \tag{3.40}$$

$$x_0(t) \approx -\upsilon t + \frac{\alpha_0^2}{2\upsilon n_\mathrm{m}^2} \frac{t^5}{5} \equiv -\upsilon t + \alpha_1 \frac{t^5}{5}. \tag{3.41}$$

Here we have the negative sign in front of the square root since the electron layer moves in the negative direction. To describe the shape f we use the expression for the density profile (3.26) which is derived in the previous section. With this function we replace the Gaussian function that is used in [43]. Obviously the function (3.26) fits the density much better than the Gaussian function as shown above. From the second equation of (3.36), we read that the maximal value of f

is one. Consequently we conclude, that

$$f(x) = \frac{1}{n_{\mathrm{m}}} n_a(x). \tag{3.42}$$

Since n_{m} should represent the maximum of n_a, we can write $n_{\mathrm{m}} = n_a(x_{\mathrm{m}})$, where x_{m} is the extrem value of n_a, which depends on parameters a and x_{min}. In addition we multiply the shape function with a wider Gaussian function since f decays too slowly ($\propto 1/x$) for positive x and after certain x-value does not coincide with the given density. Thus, the Gaussian helps as to cut this "tail" with no influence on the spectrum structure. So we have

$$f(x) = \frac{n_a(x)}{n_a(x_{\mathrm{m}})} e^{-\frac{x^2}{\tilde{\sigma}^2}}. \tag{3.43}$$

Now, we just need to insert the equations (3.39), (3.41) and (3.43) in (3.35) in order to obtain the analytical expression of the current distribution.

$$J_\perp(x,t) = \alpha_0 t^2 \frac{n_a(\zeta)}{n_a(x_m)} e^{-\frac{\zeta^2}{\tilde{\sigma}^2}}, \quad \zeta \equiv x + \upsilon t - \alpha_1 \frac{t^5}{5}. \tag{3.44}$$

To get some result we need to choose the parameters contained in this formulas, in the way that the calculated distribution would be similar to those we obtained from the simulation (Fig. 3.15 (a)). Moreover, the physical values like the maximal density n_{m} or maximal velocity υ have to be in line with the simulation results. We find that the parameter set we used to obtain Fig. 3.15 (b) is a good choise. First of all, we see that the analytical current distribution fits the original one quite well (Fig. 3.15). The chosen maximal density n_{m} is in line with the simulation as can be seen from Fig. 3.10. In order to have an idea concerning the order of magnitude of the gamma factor, we visualized the distribution of γ in vicinity of the density spike (Fig. 3.16). As we see γ almost reaches the value $\gamma = 15$. The numbers a and x_{min} that characterize the shape are similar to those we used in Fig. 3.10. They are slightly different because these numbers pass better for fitting the current density through some finite time interval, while in case of Fig. 3.10 only one particular time point is considered.

Now we consider the radiation emission from the assumed current distribution as well as its spectrum. Equation (3.28) enables us to calculate the radiation and the spectrum analytically (see appendix A). Here we give the expression of radiated

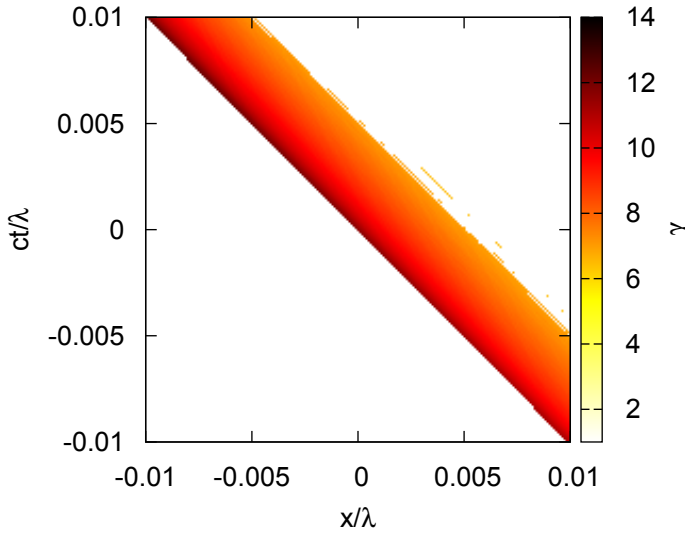

Figure 3.16: Distribution of γ factor in the given nanobunch calculated only in cells with density bigger than $200n_c$.

spectrum that is derived in line with [43].

$$I(\omega) = E_r^2(\omega) = 4\pi^4 \alpha_0^2 (\alpha_1 \omega)^{-\frac{6}{5}} \left(Ai_2''(\alpha_1^{-\frac{1}{5}} \delta \omega^{\frac{4}{5}}) \right)^2 |f(\omega)|^2, \tag{3.45}$$

$$\alpha_1 = \frac{a_0^2}{2\upsilon n^2}, \quad \delta = 1 - \upsilon, \quad Ai_2'' = \frac{d^2}{dx^2} \frac{1}{2\pi} \int e^{i\left(xt + \frac{t^5}{5}\right)} dt.$$

The Fourier transform of the shape function $f(\omega)$ is calculated numerically using FFT. In Fig. 3.17 (b) the spectrum calculated using (3.45) is compared with the spectrum calculated from original reflected pulse (Fig. 3.13) via FFT. Obviously the description works very well almost until 1000-th harmonic. Both graphs diverge for $\omega < 100\omega_0$ but anyway the method of SPP used here works only for high harmonics, so we may not expect the coincidence for low frequencies. In Fig. 3.17 (a) the corresponding pulses are compared. So the red one is the same as shown in Fig. 3.13 and the black one is determened from the assumed analytical current distribution using (3.28). Both graphs behave in the similar manner. To conclude, we can say that we obtained quite good results applying our new shape function derived in the previous section instead of a Gaussian function.

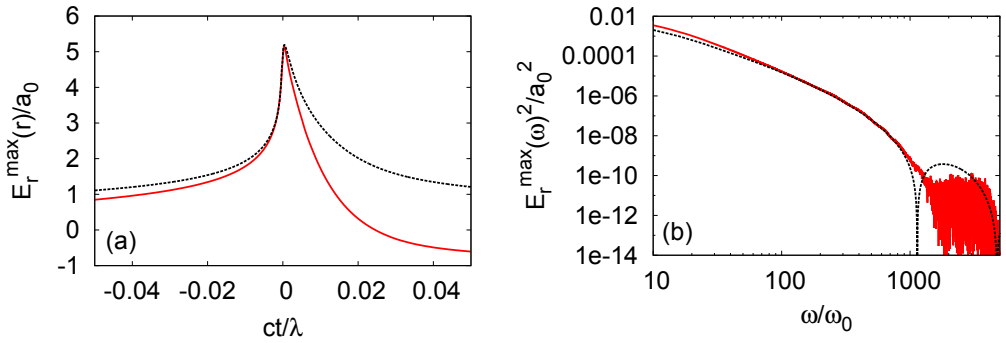

Figure 3.17: Reflected radiation obtained from the simulation ((a) red) and from the analytical current distribution ((a) black), as well as the corresponding spectra in (b). The spectrum from the simulation is taken directly from the radiated pulse via FFT, while the other one is obtained using the equation (3.45).

Going along the same line we analyze now the intermediate case $\dot{x}_0(t) \lesssim c$ shown in Fig. 3.11 and 3.12. As we said before, we attribute this case to the parabolic case. In these figures we have two examples of this case which originate from two different simulations. We will investigate both of them in order to make sure that our model works not only for one particular parameter set. First of all, we consider the reflected pulse trains and filter out the pulses we are interested in (Fig. 3.18 and 3.19). The density and the gamma factor of the corresponding

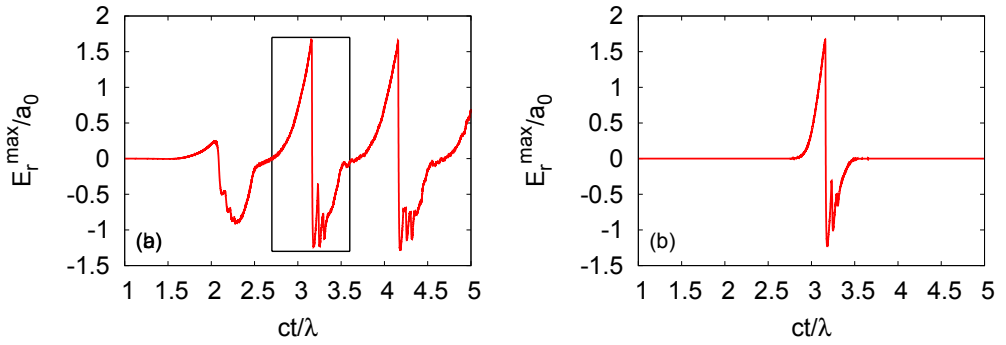

Figure 3.18: (a) Part of the reflected radiation given by $\frac{1}{2}(E_y(t) - B_z(t))$. (b) Single pulse from the reflected pulse train filtered out by the Gaussian function. Simulation parameters are the same as for Fig. 3.3.

electron bunch is shown in Fig. 3.20 and 3.21. The point (0,0) corresponds to the SPP like in the previous case. Even from this picture one can clearly see that the velocity in the SPP significantly deviates from the speed of light and is approximately $0.85c$ in Fig. 3.20 and $0.91c$ in Fig. 3.21. From the distribution of

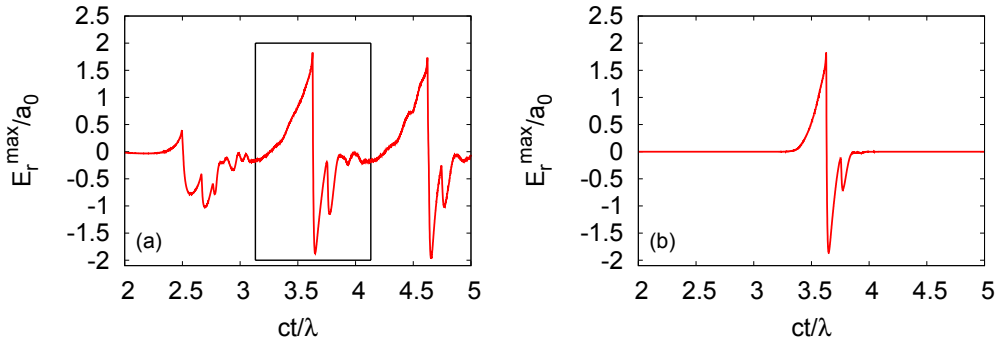

Figure 3.19: (a) Part of the reflected radiation given by $\frac{1}{2}(E_y(t) - B_z(t))$. (b) Single pulse from the reflected pulse train filtered out by the Gaussian function. Simulation parameters are the same as for Fig. 3.12.

the gamma factor we see that it is roughly constant within the electron layer. So we can use the same approximation as in the previous case

$$\sqrt{\dot{x}_0(t)^2 + \bar{v}_\perp(t)^2} \approx v. \tag{3.46}$$

The difference between (3.38) and (3.46) is of course that in last equation v is not

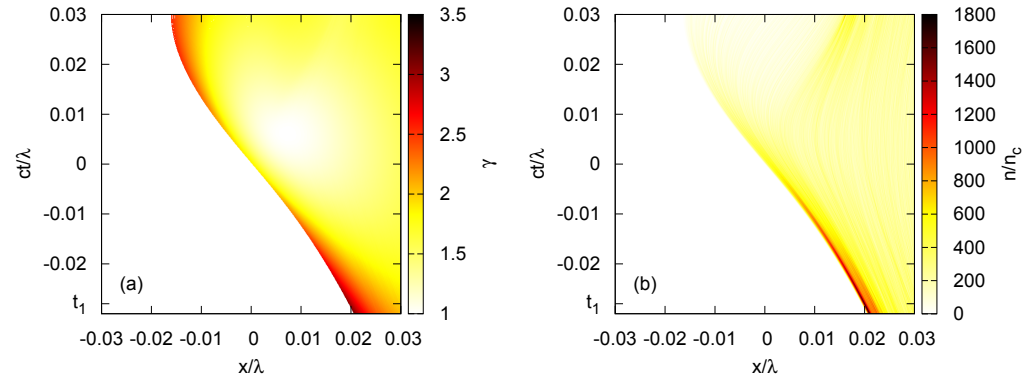

Figure 3.20: (a) Distribution of the gamma factor in the given electron bunch in space time domain. (b) The electron density distribution in space time domain. Simulation parameters are the same compared to Fig. 3.3. All magnitudes are taken in the simulation frame. t_1 denotes the time which corresponds to Fig. 3.11, $t_1 = -0.028\lambda/c$.

close to c. For that reason the electron phase space distribution does not become "whip-like" (Fig. 3.11 and 3.12). Now let us consider the corresponding current

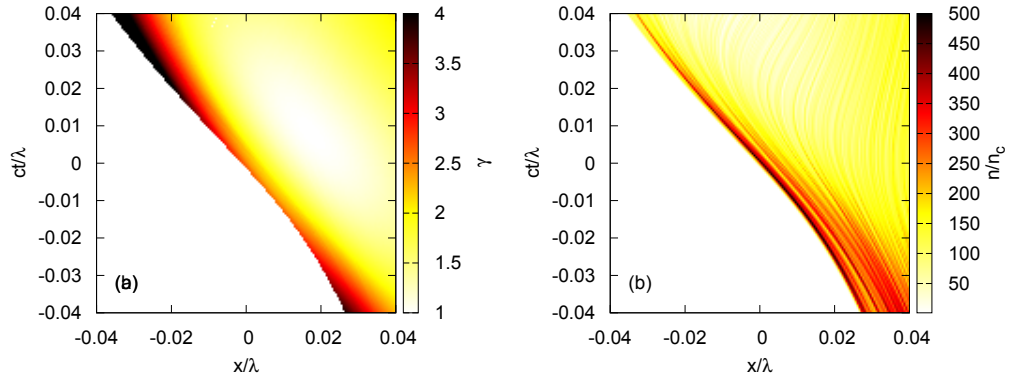

Figure 3.21: (a) Distribution of the gamma factor in the given electron bunch in space time domain. (b) The electron density distribution in space time domain. Simulation parameters are the same compared to Fig. 3.12, which corresponds to $t = 0$. All magnitudes are taken in the simulation frame.

distributions (Fig. 3.22(a) and 3.23(a)). In this case, the current changes its sign in the SPP, so we can assume

$$j(t) \approx -\alpha_0 t. \tag{3.47}$$

Similar to the previous case, we derive

$$x_0(t) \approx -vt + \frac{\alpha_0^2}{2vn_\mathrm{m}^2}\frac{t^3}{3} \equiv -vt + \alpha_1\frac{t^3}{3}. \tag{3.48}$$

Using these assumptions we calculate the current distributions analytically (Fig. 3.22(b) and 3.30(b)). The gamma factors can be roughly read from Fig. 3.20 and 3.21, so we set $\gamma = 2$ and $\gamma = 2.5$ respectively. These values match well the corresponding maximum longitudinal velocities of the layer obtained above. Finally, we obtain the spectrum of a reflected wave (see appendix A)

$$I(\omega) = E_r^2(\omega) = 4\pi^4\alpha_0^2(\alpha_1\omega)^{-\frac{4}{3}}\left(Ai_1'(\alpha_1^{-\frac{1}{3}}\delta\omega^{\frac{2}{3}})\right)^2|f(\omega)|^2, \tag{3.49}$$

$$\alpha_1 = \frac{a_0^2}{2vn^2}, \quad \delta = 1 - v, \quad Ai_1' = \frac{d}{dx}\frac{1}{2\pi}\int e^{i\left(xt+\frac{t^3}{3}\right)}dt.$$

The corresponding pulses and their spectra are shown in Fig. 3.24 and 3.25.

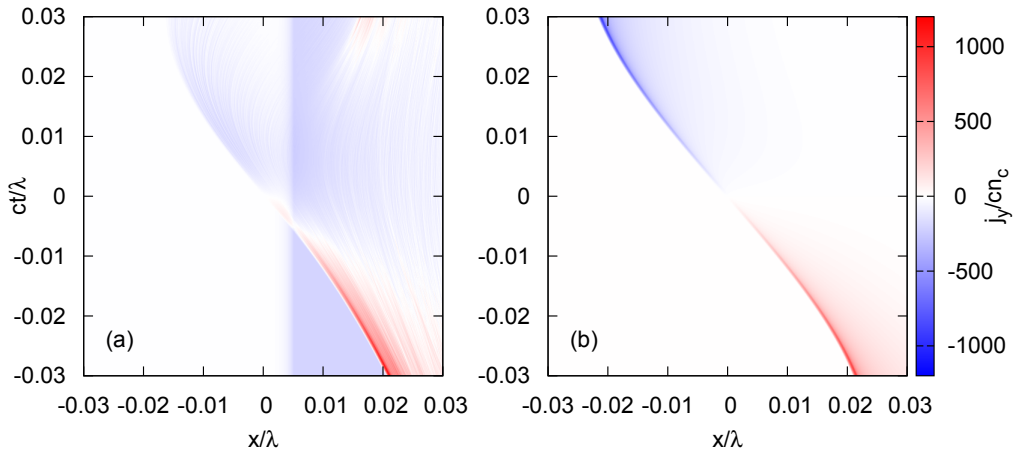

Figure 3.22: Transverse current density from the simulation (a) and calculated analytically (b). In (a) the simulated current density near the SPP is illustrated. Simulation parameters are the same compared to Fig. 3.3. In (b) the analytically calculated current distribution is shown. The parameters used in equation (3.48) are: $\alpha_0 = 3 \cdot 10^4$, $n_\mathrm{m} = 1000$ and $\gamma = 2$, while the parameters used for the shape are: $a = 4 \cdot 10^{-4}\lambda$ and $\tilde{\tilde{\sigma}} = 0.02\lambda$. The velocity υ in (3.41) is derived from the given gamma factor.

Even if the above assumptions did not work as good as in the previous case, the obtained results still give a satisfactory approximation.

We can generalize the equations (3.45) and (3.49) and write:

$$I(\omega) = E_r^2(\omega) = 4\pi^4 \alpha_0^2 (\alpha_1 \omega)^{-\frac{2n+2}{2n+1}} \left(\frac{d^n}{d\xi^n} Ai_n(\xi_n) \right)^2 |f(\omega)|^2, \tag{3.50}$$

$$\xi_n = \alpha_1^{-\frac{1}{2n+1}} \delta\omega^{\frac{2n}{2n+1}}, \quad Ai_n = \frac{1}{2\pi} \int e^{i\left(xt + \frac{t^{2n+1}}{2n+1}\right)} dt. \tag{3.51}$$

We obtain this formula from the general assumption $j(t) = \alpha_0(-t)^n$ for the transverse current. The index n corresponds to the order of a certain γ-spike. Thus, we see that in the first example (whip case) we have the second order gamma spike, while in the second example (parabolic case) the first order gamma spike is obtained.

Now it is time to deal with our second goal, namely to investigate the most efficient case of HHG at moderate laser intensity ($a_0 = 10$). For this purpose we perform

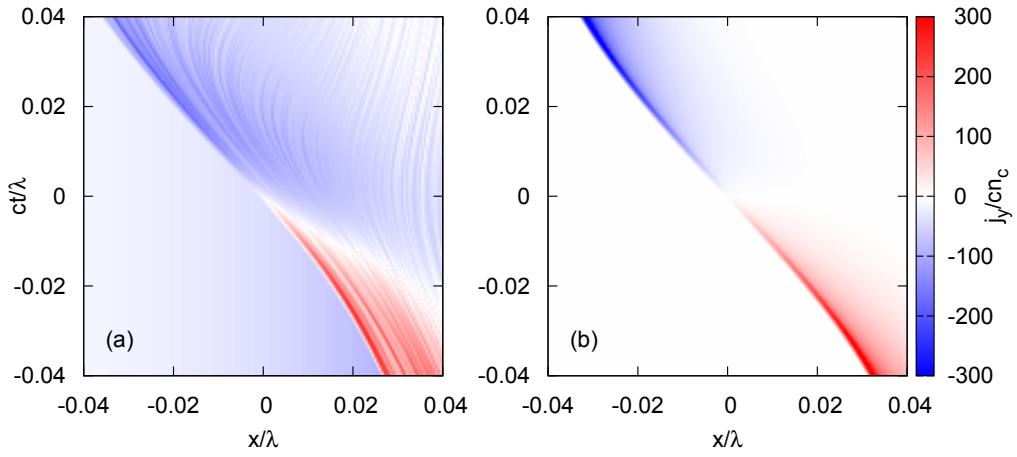

Figure 3.23: Transverse current density from the simulation (a) and calculated analytically (b). In (a) the simulated current density near the SPP is illustrated. Simulation parameters are the same compared to Fig. 3.12. In (b) the analytically calculated current distribution is shown. The parameters used in equation (3.48) are: $\alpha_0 = 1 \cdot 10^4$, $n_\mathrm{m} = 500$ and $\gamma = 2.5$, while the parameters used for the shape are: $a = 1 \cdot 10^{-3}\lambda$ and $\tilde{\tilde{\sigma}} = 0.02\lambda$. The velocity v in (3.41) is derived from the given gamma factor.

several 1D PIC simulations and vary the steepness of the exponential density gradient as well as the incident angle. For each parameter set we consider the reflected radiation in order to find the increase of the amplitude that is common in the case of nanobunching. In Fig. 3.26 we visualized the maximal amplitude of the reflected wave for each parameter set respectively. Consider the incident angle between 45° and 60°, since by this angles the most interesting things happen. Of course, one notices the sharp increase of the reflected wave amplitude in the area around $\sigma = 0.4\lambda$ zoomed in Fig. 3.26(b). By $\sigma = 0.5\lambda$ and the angle 48° (laboratory frame) we get the amplification of a factor of five. This is the most efficient HHG we could obtain. We call this area high amplitude parameter set (HAPS). In this area we mostly obtain the second order γ-spikes and the current does not change its sign in the SPPs like in Fig. 3.15. Furthermore, our study shows that the maximum longitudinal velocity of the boundary electron layer increases monotonically with σ until HAPS, where it almost reaches c. For $\sigma < 0.05\lambda$ the boundary oscillates too slowly so that no short pulses are generated. Roughly in the range between 0.05λ and 0.1λ we obtain the reflected radiation

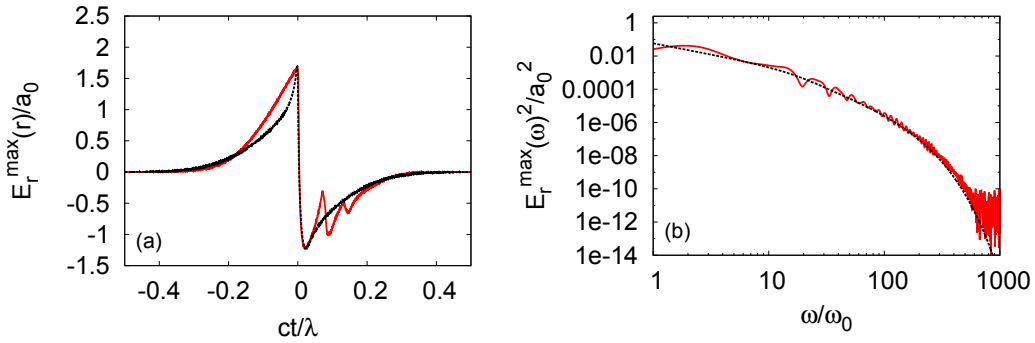

Figure 3.24: Reflected radiation obtained from the simulation ((a) red) and from analytical current distribution ((a) black), as well as the corresponding spectra in (b). The spectrum from the simulation is taken directly from the radiated pulse via FFT, while the other one is obtained using the equation (3.49). Simulation parameters are the same as for Fig. 3.3.

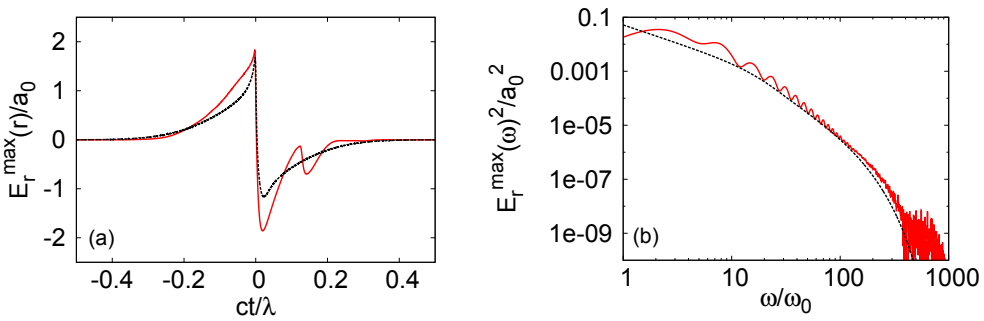

Figure 3.25: Reflected radiation obtained from the simulation ((a) red) and from analytical current distribution ((a) black), as well as the corresponding spectra in (b). The spectrum from the simulation is taken directly from the radiated pulse via FFT, while the other one is obtained using the equation (3.49). Simulation parameters are the same as for Fig. 3.12.

very similar to that from Fig. 3.18, 3.19 and generated via the same mechanism. We call this area moderate amplitude parameter set (MAPS). Here we have only the first order γ-spikes and the current changes sign in the SPPs. Thus, the reflected spectrum in MAPS can be approximated with equation (3.25) (parabolic case) and the area of HAPS corresponds to the exponential case (equation (3.26)). In the area between MAPS and HAPS the interaction is too complicated to be attributed to any model.

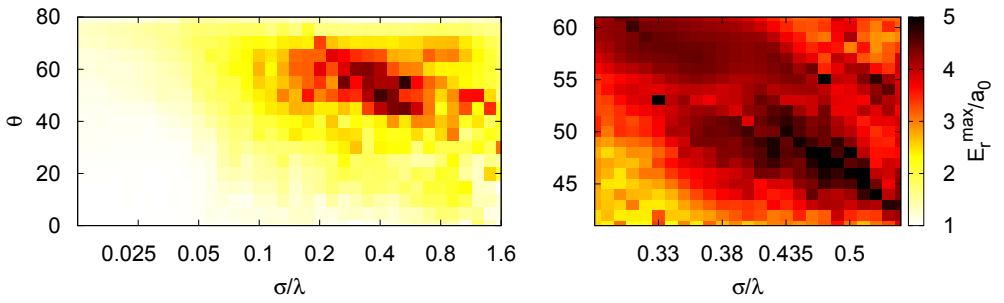

Figure 3.26: Each point in these pictures corresponds to the maximal amplitude obtained from the reflected radiation taken from corresponding simulation. We have different angles of incidence along the y-axis and different steepness of the density gradient along the x-axis, where σ is taken from (3.6) and $n_0 = 100n_c$ (laboratory frame). The right picture is the zoom in the parameter range where the most strong amplification is obtained.

3.4 Transmitted radiation in nanobunching regime

We considered only reflected radiation untill now, but the question if the transmitted radiation could also be described with our model still can be asked. The CSE in transmission has already been obtained by normal incidence on ultra-thin foils [44, 45]. So we performed several simulations using the 0.2λ foil and varying the density gradient and the density. By choosing $\sigma = 0.4$ for the

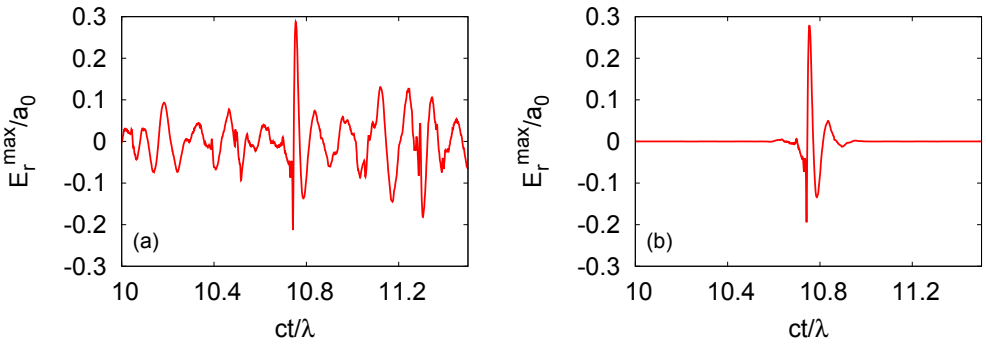

Figure 3.27: (a) Part of the transmitted radiation. (b) Single pulse filtered out by the Gaussian function. Simulation parameters: initial plasma density $n_0 = 40n_c$; $\sigma = 0.4\lambda$, normal incident pulse with dimensionless amplitude $a_0 = 10$ has the wave length $\lambda = 820$nm.

density gradient and a density of $40n_c$, we could obtain a transmitted pulse with a maximum amplitude that reaches almost 30% of the incident amplitude (Fig. 3.27). This pulse is radiated by the electron nanobunch that is accelerated in

forward direction and reaches a velocity of $v \approx 0.95c$ in the SPP (Fig. 3.28 (b)). Unfortunately, the electrons are distributed very arbitrarily in phase space (Fig.

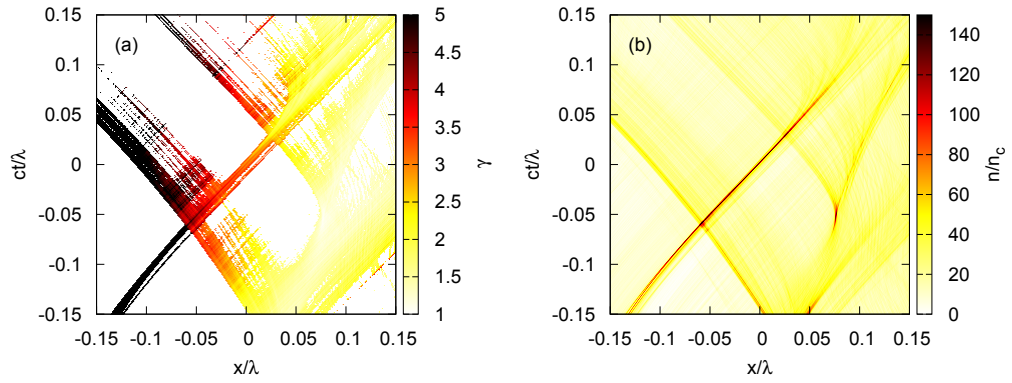

Figure 3.28: (a) Distribution of the gamma factor in the given electron bunch in space time domain. Gamma factor is shown only for the cells with density above $20n_c$. (b) The electron density distribution in space time domain. Simulation parameters are the same compared to Fig. 3.27.

3.29), so there is no chance to apply our analytical formulas for the density spike in this case. The reason of the broad distribution function can be the significant rise of the electron temperature. Instead, the density profile of the considered electron bunch can be roughly described with a simple Gaussian

$$f(x) = e^{-\frac{x^2}{\sigma^2}}. \tag{3.52}$$

as done in [42, 43]. In Fig. 3.30 (a) the transverse current distribution of the given electron bunch is demonstrated. We see that the current changes its sign in the SPP, so we use equation (3.47) here, while $x_0(t)$ changes its sign compared to (3.48),

$$x_0(t) \approx vt - \alpha_1 \frac{t^3}{3}. \tag{3.53}$$

Now we can calculate the current distribution of the bunch that is shown in Fig. 3.30 (b). In order to calculate the transmitted radiation, we use

$$E_{tr}(t) = \pi \int J_\perp(x, t+x)dx, \tag{3.54}$$

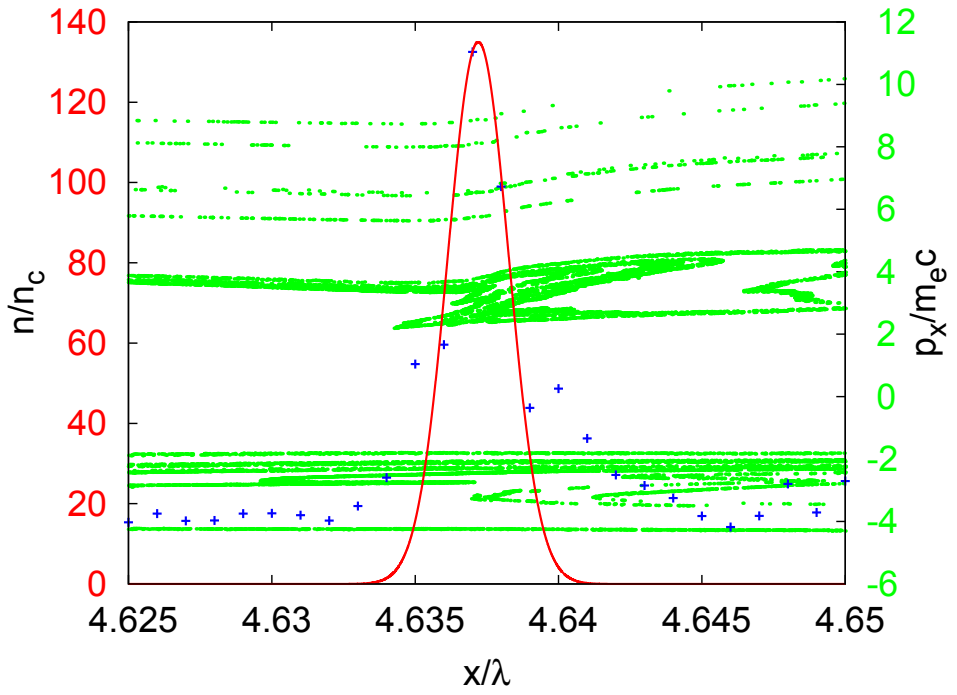

Figure 3.29: Electron density is taken from simulation in SPP (blue) and calculated analytically via (3.25) (red), as well as electrons in x-p_x-plane (green), Simulation parameters are the same comparing to Fig. 3.27, while by analytical description we used $\tilde{\tilde{\sigma}} = 0.0015\lambda$.

while the formula for the spectrum is obviously the same as in (3.49). Since we use a Gaussian function as the shape here, we insert its analytical Fourier image in (3.49). Subsequently, as in the cases of reflected radiation, we consider the analytical and numerical transmitted pulses as well as their spectra (Fig. 3.31). It is not very surprising that the results do not fit exactly, especially for the low frequency range. This is because the radiation is formed within the skin layer and has to propagate through whole foil. The trajectory of the radiating electron nanobunch is not in vacuum anymore, but encompasses the bulk plasma.

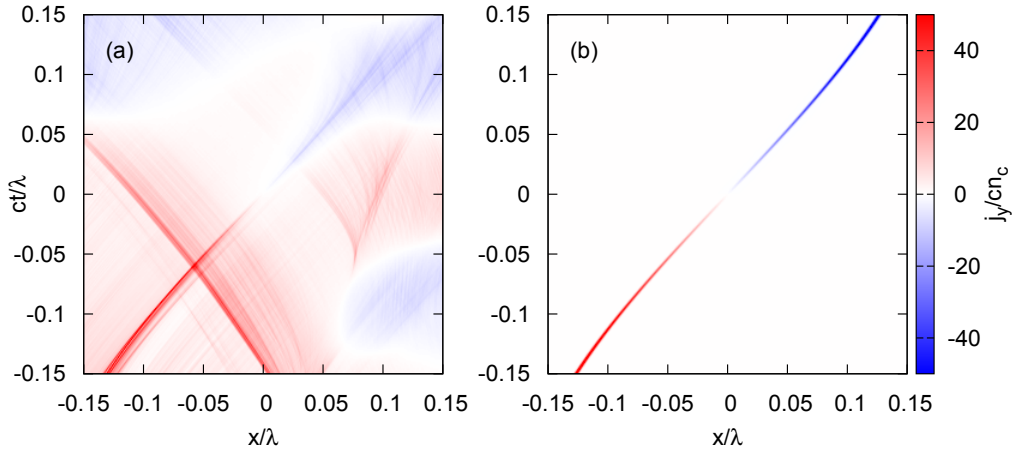

Figure 3.30: Transverse current density from the simulation (a) and calculated analytically (b). In (a) the simulated current density near the SPP is illustrated. Simulation parameters are the same comparing to Fig. 3.27. In (b) the analytically calculated current distribution is shown. The parameters are used in equation (3.48): $\alpha_0 = 500$, $n_\mathrm{m} = 100$ and $\gamma = 3$, while for the shape we used: $\tilde{\tilde{\sigma}} = 0.0015\lambda$. The velocity v in (3.41) is derived from the given gamma factor.

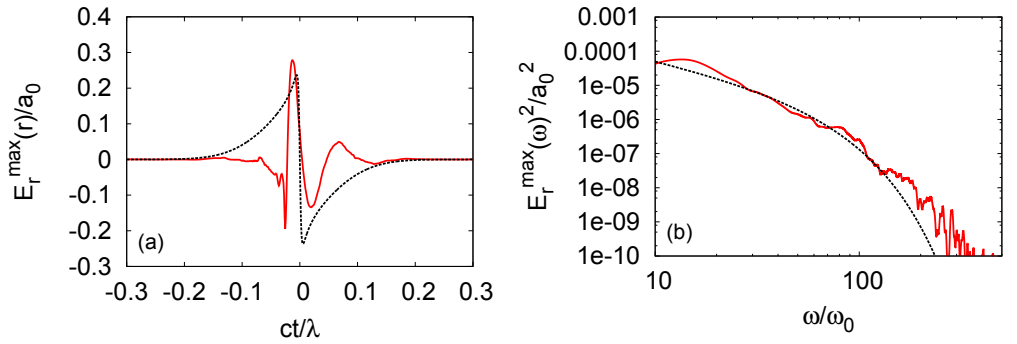

Figure 3.31: Transmitted radiation obtained from the simulation ((a) red) and from analytical current distribution ((a) black), as well as the corresponding spectra in (b). The spectrum from the simulation is taken directly from the radiated pulse via FFT, while the other one is obtained using the equation (3.49).

3.5 Conclusions

We were able to obtain two different analytical expressions of the electron density profile describing the density spikes in two different cases specified by the electron phase space distribution. First, we presented the parabolic case, where the phase space distribution can be approximated by a parabola. In the second case, the electrons in phase space could be fitted with an exponential function. We called this case the whip case. A few examples, where the analytical formulas describe the simulated density quite well have been presented . Furthermore, we discussed simulation results of HHG, where we were able to obtain an amplitude increase in the reflected pulse by a factor of five without using extremely intense incident laser pulses. This was possible after we found optimal parameters for the density gradient combined with an optimal incident angle. Moreover, based on some simple assumptions, we were able to describe the distribution of transverse current in the vicinity of the SPP analytically in both cases. The obtained expressions together with the analytical expressions for electron density give us the possibility to fit the numerically obtained spectra of the back radiated pulse quite good.

Chapter 4

Wavebreaking-associated transmitted emission

Authorship claim: The content of this chapter is largely reproduced from the paper [64] published in New Journal of Physics on June 2016.

4.1 Simulation set up

Both one-dimensional (1D) and 2D particle-in-cell (PIC) simulations are carried out using the Virtual Laser Plasma Lab (VLPL) code[62]. We firstly present the 1D results to investigate the radiation mechanism in detail. Here, we demonstrate the basic idea mainly by considering the simplest configuration of normal laser incidence and step plasma density profile. As such, this mechanism can be pointed out most clearly since it is easily distinguished from the other mechanisms. For example, CWE cannot play a role with this geometry, because it requires oblique laser incidence and short density gradient[65]. Besides, the emission cannot simply be attributed to ROM either, because ROM only occurs in the reflection direction[45].

The incident laser is linearly polarized in z-direction, with a Gaussian temporal profile $a_z(t) = a_L \exp(-t^2/\tau^2)$, where $a_L = eE_L/(m_e c\omega_0)$ is the normalized laser amplitude with E_L and ω_0 the laser field amplitude and the laser frequency respectively, e, m_e, and c are respectively the electron mass, the elementary charge and the speed of light in vacuum, and $\tau = 0.5T_0$ is the pulse duration with $T = 2\pi/\omega_0$ the laser pulse duration. Here for simplicity we firstly consider this

quasi-single-cycle pulse. The effect of multi-cycle laser pulses will be discussed in section 5.2. The fully ionized plasma, with a thickness of d=120 nm and an electron density of $n_0 = 100n_c$, is initially located between $x = 5\lambda_0$ and $x = 5.15\lambda_0$, where λ_0= 800 nm is the laser wavelength, $n_c = m_e\omega_0^2/4\pi e^2$ is the critical plasma density. The ions are assumed to be immobile due to the short interaction time being considered. The cell size is $\lambda_0/2000$ and each cell is filled with 100 macroparticles.

4.2 Radiation features

To show the essential signatures of the transmitted XUV pulses, we present the results of two reference cases in Fig. 4.1, with frames (a) and (b) for a laser amplitude $a_L = 20$, and frames (c) and (d) for $a_L = 30$. From the temporal profiles of the electric field depicted in Fig. 4.1(a) and (c), one can see intense few-cycle pulses have been generated. The emitted pulse has the same polarization with the laser pulse, i.e., only with electric field along z-direction. This is different from CWE, which emits y-polarized HHG even for a z-polarized obliquely incidence laser[65]. The peak electric field is only about one order of magnitude smaller than that of the laser field. The transmitted XUV emission is strong. Its energy is about one-fifth of that carried by the reflected XUV harmonics (XUV frequency components from $10\omega_0$ to $100\omega_0$ are compared). For $a_L = 30$, the XUV pulse is nearly single-cycle, reaching an extremely high peak field of $E_z/E_L = 0.3$, corresponding to $E_z = 3.5 \times 10^{13}$ V/m. The insets of Fig. 4.1(a) and (c) show the pulse intensity. The full-width at half-maximum (FWHM) of the pulses are approximately 190 attoseconds and 20 attoseconds for $a_L = 20$ and $a_L = 30$, respectively.

Fig. 4.1(b) and (d) are the Fourier spectra corresponding to Fig. 4.1(a) and (c), respectively. The spectra display a low-frequency cutoff at the initial plasma frequency $\omega_{p0} = 10\omega_0$. Thus, the pulse can be used directly as it is already filtered by the target. The pulse energy for $a_L = 20$ as shown in Fig. 4.1(b) is mostly concentrated at the frequencies $\geq \omega_{p0}$. The spectrum for $a_L = 30$ shown in Fig. 4.1(d) is broader and extends to higher frequencies. As such, the temporal pulse width in Fig. 4.1(c) is much shorter than that in Fig. 4.1(a). When we further increase the incident laser amplitude a_L to above 40, the spectra show

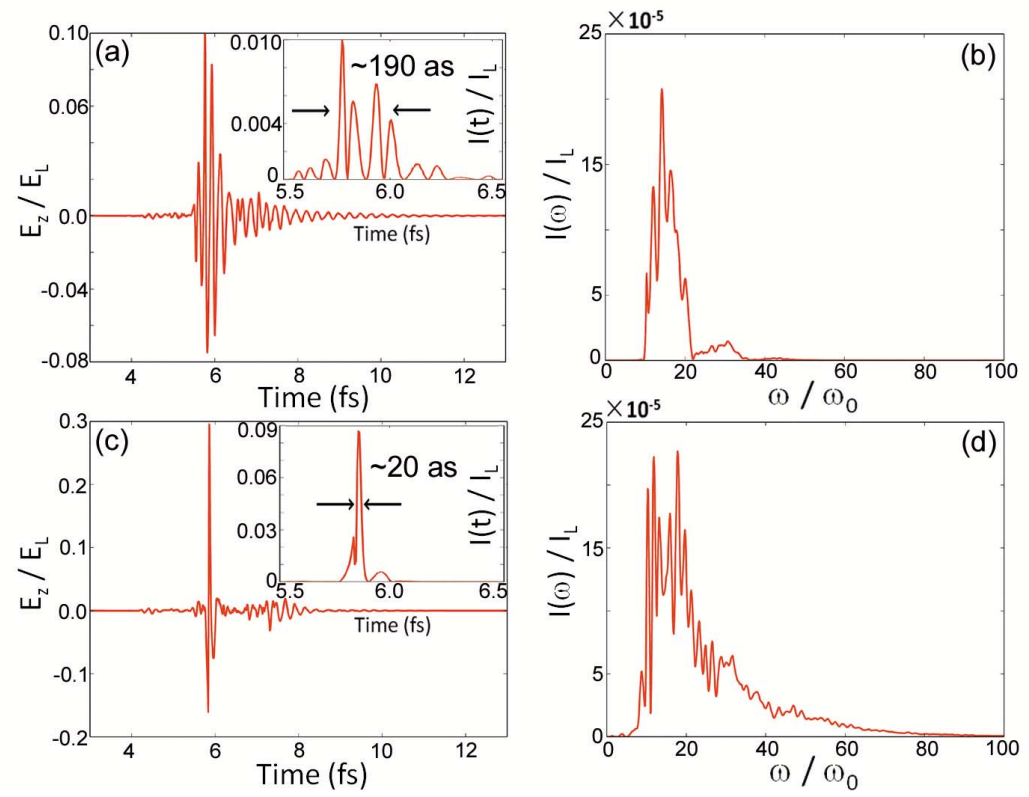

Figure 4.1: (a), (c) Temporal profiles and (b), (d) frequency spectra of the XUV pulses observed at the rear side. Frames (a) and (b) are for $a_L = 20$, and frames (c) and (d) for $a_L = 30$. The insets of (a) and (c) show the temporal profiles plotted as intensity.

lower frequencies indicating laser light transmission, as a result of strong target compression by the light pressure.

4.3 Radiation mechanism

In this section we focus on revealing the underlying mechanism of the XUV emission. Here we select the case of $a_L = 20$ for demonstration, since the basic features of radiation and the interaction dynamics are similar for both cases, as can be seen from the Supplemental movies SM1 and SM2*.

We start with discussing the possible origins of high-frequency emission based on the expression for total transverse current leading to the transverse radiation field. Considering a more general case of laser at oblique incidence with an angle of θ, the expression for the radiation source, i.e., the total transverse current $\mathbf{j}_\tau$, can be obtained as[65]

$$\mathbf{j}_\tau(x,t) = -\frac{e^2 n_e(x,t)}{m_e \cos\theta}\frac{\mathbf{A}(x,t)}{\gamma(x,t)} - ec\tan\theta\Big[Zn_i(x,t) - \frac{1}{\cos\theta}\frac{n_e(x,t)}{\gamma(x,t)}\Big]\hat{\mathbf{e}}_y, \tag{4.1}$$

where $\mathbf{A}$ is the total vector potential, Z is the ion charge number, n_i is the ion density, and $\hat{\mathbf{e}}_y$ is the unit vector along y-axis.

The second term is always along the y-direction and only occurs for oblique incidence with $\theta \neq 0$. This is the source term responsible for the CWE mechanism[65]. It can emit radiation directly from the plasma oscillation n_e, without the need to couple with the transverse laser field. This is obviously not the case in our scheme where $\theta = 0$ and the emission is in the z-direction. In addition to requiring oblique incidence, CWE is only possible in the presence of a density gradient, since its mechanism is basically the inverse process of resonance absorption.

Under the condition of laser field E_z at normal incidence with $\theta = 0$, the total transverse current is recast to be

$$\mathbf{j}_\tau(x,t) = -\frac{e^2}{m_e}\frac{n_e(x,t)}{\gamma(x,t)}\mathbf{A}_z(x,t), \tag{4.2}$$

*See the supplemental material available at http://iopscience.iop.org/1367-2630/18/6/063014/media for further results: the animated version of the field and plasma dynamics for $a_L = 20$ (1D simulations) in movie SM1, $a_L = 30$ (1D simulations) in movie SM2, and $a_L = 20$ (2D simulations) in movie SM3.

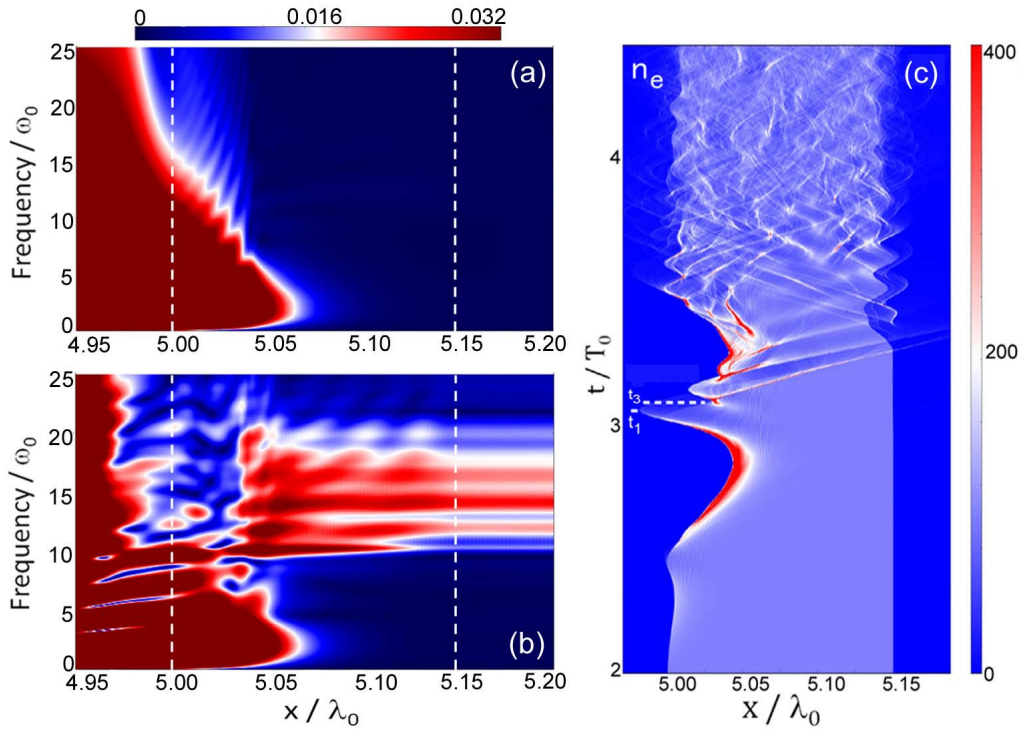

Figure 4.2: (a)-(b) Spatially resolved spectrum of transverse electric field E_z. At each spatial observation point x, Fourier transform is carried out with respect to the temporal waveform recorded. The time interval is from $t = 0$ to $t = 3.06T_0$ (marked as t_1 in frame (c)) for frame (a), and from $t = 3.06T_0$ to $t = 8.0T_0$ for frame (b). The vertical dashed white lines mark the initial plasma boundaries. (c) Spatial-temporal distribution of the electron density $n_e(x, t)$ in units of n_c. Time $t_3 = 3.10T_0$ is also marked, which indicates the onset of wavebreaking. Here, $a_L = 20$.

In this case, high frequencies can be introduced by temporal modulation of the effective plasma density n_e/γ and the vector potential $\mathbf{A}_z$, and Doppler upshifting effect. The ROM mechanism is dominated by the Doppler upshifting effect, and thus can only occur in the reflected direction[45]. In the following, we show that our observed transmitted emission can be mainly attributed to strong density oscillations at wavebreaking level coupled to transverse electric fields in the laser-illuminated surface layer.

4.3.1 Region of emission

We firstly demonstrate that the transmitted emission originates from the laser-illuminated front layer of the target. To see this, we plot the spatially resolved

spectra in Figs. 4.2(a)-(b), which give the information about when and where the emission occurs. The procedure to obtain these spectra is as following. First, we record the temporal profile of the transverse electric field $E_z(x_0, t)$ at the spatial position x_0 over a period of time. Next, Fourier transformation is carried out with respect to this temporal profile $E_z(x_0, t)$ to obtain $E_z(x_0, \omega)$. We do this for each point of x in the range between $x = 4.95\lambda_0$ and $x = 5.20\lambda_0$. Finally we map the spatial-spectra distribution of $E_z(x, \omega)$ as Figs. 4.2(a)-(b). The time interval for Fig. 4.2(a) is from $t = 0$ to $t = 3.06T_0$, and for Fig. 4.2(b) from $t = 3.06T_0$ to $t = 8.0T_0$. Here T_0 is the laser period. Time $t = 3.06T_0$ is also marked as t_1 in Fig. 4.2(c), which shows the spatial-temporal distribution of the electron density $n_e(x, t)$. Time $t_3 = 3.10T_0$ marked in Fig. 4.2(c) indicates, as we will show later, the onset time of wavebreaking. This means that Fig. 4.2(a) and (b) are plotted respectively before and after the time when wavebreaking occurs. As can be seen, there is no transmitted emission before the wavbreaking occurs (see Fig. 4.2(a)), while after the onset of wavebreaking the transmitted emission is observed (see Fig. 4.2(b)). Note that the frequency of the transmitted emission in Fig. 4.2(b) accords with the XUV spectrum shown in Fig. 4.1(b). In addition to the timing of the transmitted emission, another important observation is that this XUV pulse observed at the target rear side originates from the front (laser-illuminated) layer of the target. The XUV pulse then propagates through the plasma slab.

Next, we show that strong plasma density oscillations occur in this front layer. From the spatial-temporal distribution of the electron density shown in Fig. 4.2(c), one can see that electrons at the front plasma surface are initially pushed forward by the laser light pressure and then bounce back in the first half laser cycle. The same process repeats in the second half laser cycle, but with some different features: in addition to follow the driving-laser-pulse shape, the plasma surface also exhibits higher frequency oscillations. As mentioned above, it is during this time the transmitted emission occurs.

4.3.2 Onset of wavebreaking

To understand how the strong density oscillations arise, we present the plasma dynamics at six characteristic times in Fig. 4.3: $t_0 = 2.66T_0$, $t_1 = 3.06T_0$, $t_2 = 3.09T_0$, $t_3 = 3.10T_0$, $t_4 = 3.16T_0 = t_0 + T_0/2$, and $t_5 = 3.18T_0$. In the first half laser cycle, due to the large laser ponderomotive force, surface electrons are pushed

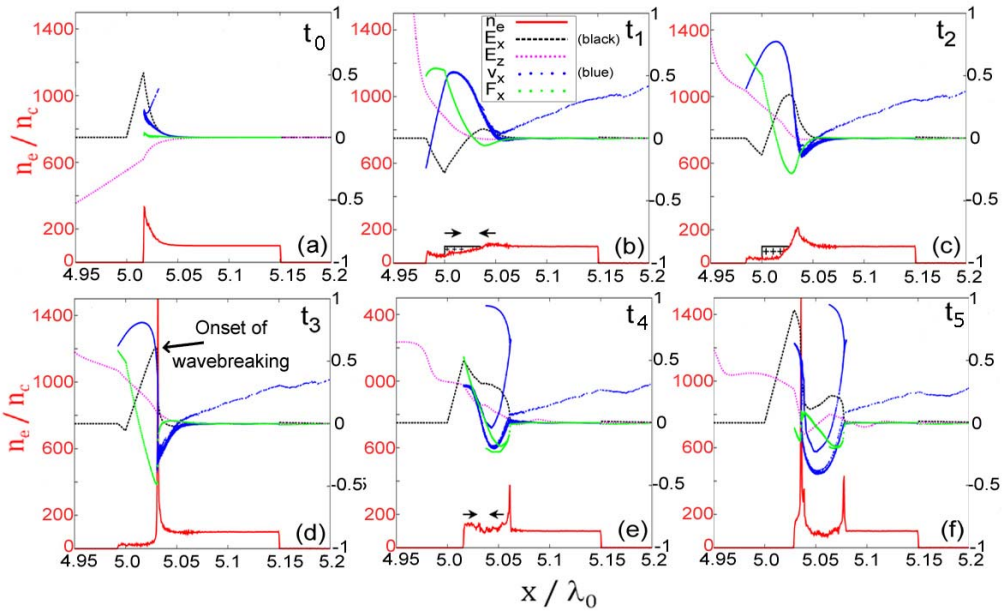

Figure 4.3: (a)-(f) Spatial profiles of n_e (red), longitudinal electric field E_x (black), transverse electric field E_z (magenta), velocity in x-direction v_x (blue), and x-component of the total force F_x (green) at six reference times, $t_0 = 2.66T_0$, $t_1 = 3.06T_0$, $t_2 = 3.09T_0$, $t_3 = 3.10T_0$, $t_4 = 3.16T_0 = t_0 + T_0/2$, and $t_5 = 3.18T_0$, where T_0 is the laser period. Here $a_L = 20$. The very sharp high-density spike formed at t_3 and the onset of a multi-stream motion in the phase space are the signatures of wavebreaking.

deep inside the plasma (see Fig. 4.3(a)), creating a large electrostatic field. As the laser ponderomotive pressure passes its first maximum, the surface electrons are pulled back by the large electrostatic restoring force, gaining a large kinetic energy before exiting beyond the initial foil edge at $x = 5\lambda_0$ (see Fig. 4.3(b)). This group of electrons experiences a stronger inward acceleration in the second half of the laser cycle, when the ponderomotive pressure and electrostatic forces in the vacuum region are co-directed. When this group of electrons returns to the plasma edge, it meets background electrons that were initially deeper inside the surface layer and are now moving in the opposite direction. When the two groups of electrons cross (see Fig. 4.3(c)), a very sharp high-density spike forms at t_3 (see Fig. 4.3(d)), also indicating the onset of a multi-stream motion in the phase space - *signatures* of wavebreaking[58]. For initially cold plasma, the wavebreaking causes an extremely high spike in the local plasma density, although thermal pressure effects may limit the actual density increase[66, 67].

4.3.3 Strong density oscillation subsequent to wavebreaking

The onset of wavebreaking is followed by a high level of plasma density oscillation. This can be seen from the spatial-temporal profile of the electron density shown in Fig. 4.2(c), and more clearly from the movie SM1 in the Supplemental Material. The dynamic process of the density oscillation subsequent to wavebreaking can be understood as following. The electrons, which start to move in the negative direction at the beginning of the second half laser period, largely affect the following plasma oscillation. They represent the electron boundary after crossing over the electrons moving to the right. Afterwards, the laser ponderomotive force dominates and it reverses the boundary electrons (see Fig. 4.3(e)). At the same time, the other electron bunches move further inside the plasma. This leads to the density profile largely different from that of half laser period ago when no wavebreaking occurs (see Fig. 4.3(a)). In the case of without wavebreaking, E_x decreases exponentially in the surface layer after reaching its maximum, while in the case of wavebreaking the electric field decays much slowly (see Fig. 4.3(e)). As a result, the electrostatic force starts to dominate in the surface layer (see the total force) and consequently the electrons in this area start to move in the negative direction. At the same time, the electrons near the boundary still move in the positive direction, so a second sharp density spike is expected (see Fig. 4.3(f)).

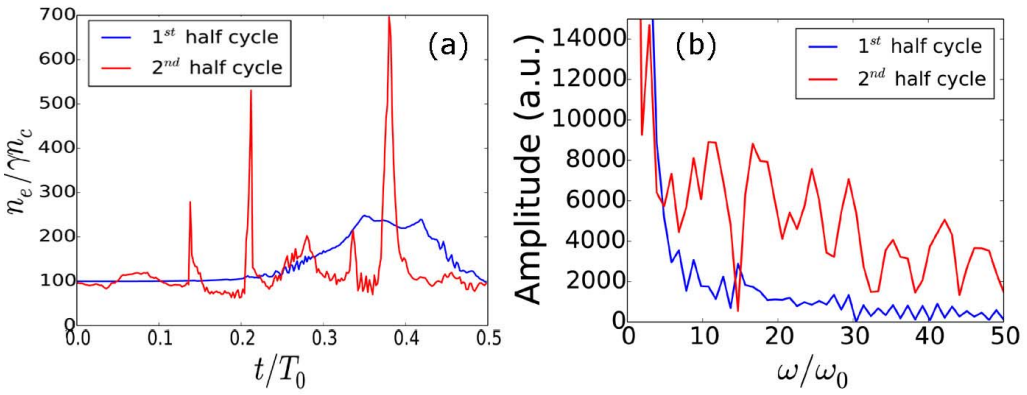

Figure 4.4: (a) The temporal profiles and (b) frequency spectra of the effective plasma density oscillation n_e/γ, recorded at a fixed position $x = 5.05\lambda_0$ near the front surface. The blue lines correspond to a time interval between $t = 2.5T_0$ and $t = 3.0T_0$ (i.e., before the wavebreaking), while the red lines between $t = 3.0T_0$ and $t = 3.5T_0$ (i.e., after the wavebreaking).

This process repeats several times that several periods of density oscillation can be expected.

From the point of view of wavebreaking, a direct consequence of wavebreaking is a large number of formerly nonresonant main body electrons can rapidly exchange energy with the plasma wave and acquire momenta efficiently. In other words, wavebreaking implies a considerable fraction of the plasma electrons are trapped and start oscillating. This leads to a greatly increased plasma fluctuation level. The strong oscillation of many surface electrons can be seen from the rotating structure of the electron phase-space distribution at latter times, as shown by the blue dotted lines in Figs. 4.3(f)-(e) and more clearly from the supplemental movie SM1.

The density variation is low and smooth before the wavebreaking, while high and fast after it. For further demonstration, we present one example of the density variation recorded at a fixed position near the front surface $x = 5.05\lambda_0$. Figures 4.4(a) and (b) show the temporal profiles and the corresponding Fourier spectra, respectively. Here the (relativistically corrected) effective plasma density n_e/γ is used and the Lorentz γ-factor is cell-averaged ($\gamma =< \gamma >_{cell}$). The blue lines in Fig. 4.4 correspond to a time interval between $t = 2.5T_0$ and $t = 3.0T_0$ (i.e., before the wavebreaking), while the red lines between $t = 3.0T_0$ and $t = 3.5T_0$ (i.e., after the wavebreaking). On the one hand, the amplitude of the density

variation is much higher after the wavebreaking than before it (see the temporal profiles shown in Fig. 4.4(a)). On the other hand, the frequency of the density oscillation is also higher after the wavebreaking, as shown in the frequency spectra of Fig. 4.4(b).

4.3.4 Emission of XUV pulses

Radiation source

Although the plasma oscillation is longitudinal, it is coupled to the electromagnetic emission via the transverse velocity of electrons in the front surface layer. To understand this coupling, we consider the wave equation with source term (as shown in equation (4.2)) in the 1D case. Assuming the laser potential $a_z^{laser}(x,t)$ in the skin layer is large, we can obtain the expression for the small emitted wave a_z^e:

$$\left(\partial_x^2 - \frac{1}{c^2}\partial_t^2\right) a_z^e(x,t) \approx \frac{4\pi e^2}{m_e c^2}\left[\frac{n_e(x,t)}{\gamma(x,t)} - \frac{n_{0e}(x,t)}{\gamma_0(x,t)}\right] a_z^{laser}. \tag{4.3}$$

Here, $n_{0e}(x,t)$ and $\gamma_0(x,t)$ are the electron density and $\gamma-$factor in the skin layer respectively in the absence of the plasma oscillations. According to equation (4.3), the emission is proportional to the laser amplitude and the amplitude of the electron plasma oscillation.

The XUV amplitude increases with increasing the laser amplitude can be expected. To see the effect of density variation, we also did the same simulations by use of a lower intensity laser ($a_L = 1$), or using a high intensity ($a_L = 30$) but circularly polarized laser. In both cases, no wavebreaking and subsequent strong density oscillation can occur. As a result, no transmitted emission has been observed. Only in the wavebreaking regime, the electron density oscillation can reach such a high level that allows this kind of emission efficiently generated. It is also seen from the radiation source term in equation (4.3) that the temporal variation of n_e/γ is mainly responsible for the high-frequency XUV emission, since the laser field changes on a much longer time scale than the plasma oscillation assuming $n_e \gg n_c$. These demonstrate the strong density oscillation subsequent to wavebreaking indeed plays a dominant role in the emission process. This is why we call this radiation "wavebreaking-associated transmitted emission.

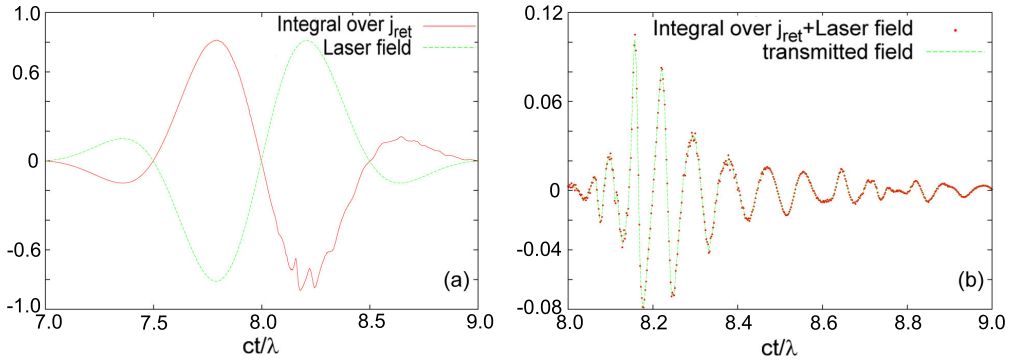

Figure 4.5: (a) The numerically calculated integral given by the first term in the RHS of equation (4.5) (red) and the second term of the laser field $E_{laser}(t)$ (green). (b) The sum of the two colored plots given in frame (a) (red) and the transmitted field obtained directly from the PIC simulation results (green).

Simulated transverse current

The density variation itself, though playing a dominate role in the emission process, does not fully determine the radiation properties. It is the retarded transverse current distribution that contains full information about the radiation. The transverse electric field measured from the rear side of the target is given by the general equation:

$$E_z(t,x) = -\frac{2\pi}{c}\int_{-\infty}^{x} j_z\left(t - \frac{x-x'}{c}, x'\right)dx' + E_{laser}(t,x). \tag{4.4}$$

The first term in the right hand side (RHS) of equation (4.4) is the integral of the retarded transverse current distribution j_z and the second term is the z-polarized laser field $E_{laser}(t,x)$ that propagates through vacuum. To calculate the radiation at the end of the simulation box, we set $x = 10\lambda$ and use dimensionless values. Thus we can drop the x-dependence of the fields and obtain:

$$E_z(t) = -2\pi\int_{0}^{x_c} j_z\left(t - x_c + x', x'\right)dx' + E_{laser}(t), \tag{4.5}$$

with $x_c = 10$. Since the values of j_z at each point of time and space can be obtained from the PIC simulation results, we can calculate the integral numerically as a function of time. The result is shown in Fig. 4.5.

During the first half laser cycle when no wavebreaking-associated plasma oscillation occurs, the value of the integral matches -$E_{laser}(t)$, i.e., the transmitted field

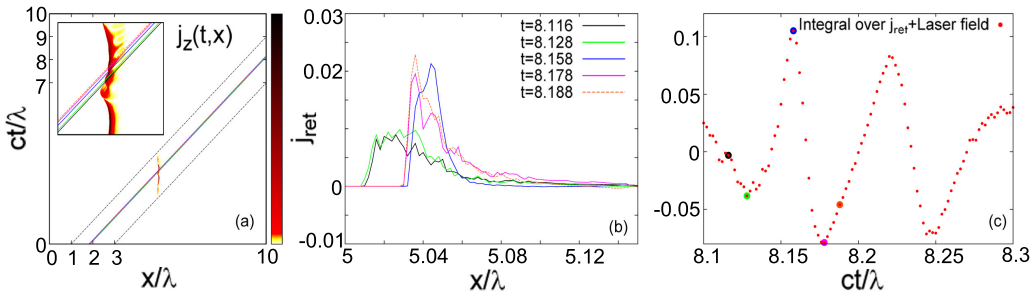

Figure 4.6: (a) The current distribution $J_z(t, x)$ as a function of time and space. The colored oblique lines represent the paths along which $J_z(t, x)$ has to be integrated to calculate the transmitted field. (b) Spatial distribution of the retarded current density for five different times. Each line in frame (b) corresponds to the line of the same color in frame (a). (c) The transmitted fields calculated numerically using equation (4.5). Each colored point corresponds to the current of the same color in frame (b).

is zero. During the second half laser cycle, the shape of the integral has some additional oscillations. Using equation (4.5) we get the calculated transmitted field that matches the result obtained directly from the PIC simulations as expected (see Fig. 4.5(b)).

The emission can also be seen directly from the evolution of E_z obtained from the PIC simulations, as shown in Figs. 4.3(a)-(f). E_z is an evanescent wave in the skin layer before the wavebreaking (see, e.g., Fig. 4.3(a)). The distribution of E_z changes drastically after the onset time of wavebreaking, e.g., as depicted in Fig. 4.3(f), E_z arises beyond the skin depth and propagates through the plasma foil. From the animated version of the field and plasma dynamics shown in movie SM1), one can see more clearly that the transmitted emission occurs right after the onset of wavebreaking.

We can also analyze how the retarded current density oscillation evolves with time and how it corresponds to each value of the transmitted field. From the green line in Fig. 4.6(b), we can see that at time $t = 8.128T_0$, the left boundary of the current profile reverses its moving direction and starts to move to the right. This leads to the transmitted field reaching a local maximum at the same time, as shown in Fig. 4.6(c). Similar process occurs at time $t = 8.158T_0$. The left boundary of the current profile reverses its moving direction again (see the blue line in Fig. 4.6(b)). Accordingly, the transmitted field reaches another local maximum(see Fig. 4.6(c)).

Obviously, this behavior of the retarded current corresponds to the plasma-density oscillation we discussed above. The density oscillation leads to a fast variation of the total current and thus gives rise to radiation at higher frequencies that can propagate through the plasma.

Let us go back to Fig. 4.6 and consider the next time point $t = 8.178\lambda/c$ (pink). At this time we have an extreme point by the transmitted field (Fig. 4.6c), but it does not coincide with the changing of the current boundary shifting direction, as in previous two cases. The current boundary reverses its direction at the time $t = 8.188\lambda/c$ (orange). Fortunately, we have an explanation of this disagreement. If we compare the last two graphs at the interval $x > 5.08\lambda$, we notice that the orange curve is significantly lower than the pink one. That's why the value of the integral is lower than we could expect if these two curves would be close to each other like in case of the black and green graphs. In fact, as the electron skin layer starts to emit radiation, this electromagnetic waves propagate through the plasma. Since the frequency of them is of the same order of magnitude as the plasma frequency, they induce the oscillation of the background electrons deeper in plasma during the propagation. Consequently, these oscillating electrons affect further emission. In other words the difference of the last two curves mentioned above is the result of these background electron oscillations. If we would consider more plots for different times as shown in Fig. 4.6b we would be able to distinguish these oscillations clearly. We see from Fig. 4.5b that the frequency of the transmitted wave is the largest in the first quarter of the second period. It happens because of two effects. First, the local plasma frequency increase, since the electrons are pressed by the ponderomotive force and secondly we have a Doppler shifting, since the electrons are pushed inside. After the first quarter of the cycle the Doppler effect vanishes and we expect strong decrease of the radiation frequency, which would also agree with the behavior of current distribution oscillations inside the skin layer (Fig. 4.6). However, we consider only a slow diminishing of the radiation frequency (fig 4.5b) and the background electron oscillations caused by the propagation of the radiation through the plasma explain these contradiction.

4.3.5 Theoretical analysis

To enable the transmitted emission propagate through the plasma slab, the plasma should locally support higher frequency oscillations which then couple to the

transverse electric fields. Here we give a simple model to show in principle it is possible for the local plasma frequency to be higher than the background plasma frequency due to density compression effect. Let us consider the local plasma frequency at the laser-plasma interface. Let the plasma be overdense with $\omega_p \gg \omega_0$. The laser is characterized by its normalized vector potential $\mathbf{a}(t) = e\mathbf{A}(t)/m_e c^2$. Electrons oscillate transversely in the laser field at the laser frequency with the normalized momentum $\mathbf{p}_\perp = \mathbf{a}$. The ponderomotive force is $\mathbf{F}_p = -\nabla\gamma$[68, 69], where the gamma factor $\gamma = \sqrt{1+a^2}$. The ponderomotive force compresses electron density within the skin depth. The force balance is then

$$\mathbf{F} = -n_i x - \frac{\partial \gamma}{\partial x} + \int_{x_0}^{x} n_e(x')dx' = 0, \tag{4.6}$$

where n_i and n_e are respectively the ion and electron density, x_0 indicates the position of the front of the electron skin layer (may be different from the initial position $x_{ini} = 0$ due to the compression), and x is a position inside the skin layer. Taking the spatial derivative of equation (4.6), we find the equilibrium electron density

$$n_e(x) = n_i + \frac{\partial^2 \gamma}{\partial x^2}. \tag{4.7}$$

Thus, the equilibrium electron density within the skin layer is, as expected, higher than the ion density due to the compression by the laser ponderomotive force.

For simplicity, we consider laser field as quasi-static with respect to the high plasma frequency. Thus, together with the electron-density compression and the acquired relativistic γ-factor of electrons, the local plasma frequency changes as well. It can be obtained from the equation of motion $\mathrm{d}\mathbf{p}/\mathrm{d}t = -\mathbf{E}$ and the Maxwell's equation $\partial\mathbf{E}/\partial t = n_e\mathbf{p}/\gamma$[69], where $\mathbf{E}$ is the electric field, so that the local plasma frequency is

$$\omega_p(x) = \sqrt{\frac{n_e(x)}{\gamma(x)}} = \sqrt{\frac{\omega_{p0}^2 + \partial^2\gamma/\partial x^2}{\gamma(x)}}, \tag{4.8}$$

where $\omega_{p0} = \sqrt{n_i}$. Because the local plasma frequency has a strong spatial dispersion, plasma waves excited in this region break easily. The change in the plasma frequency has two sources: electron density compression and increase of the electron relativistic γ-factor. These two effects tend to compensate each other, but this compensation is incomplete.

We assume an exponential decay of the laser field in the skin layer $a(x) = a_s e^{-\omega_p(x)(x-x_s)}$ in the vicinity of x_s, which is a position inside the skin layer. Considering within the skin layer the field amplitude can be small, we can write $\gamma \approx 1 + a^2/2$. To proceed further, since $\omega_p(x)$ appears in the expression for $a(x)$, let us firstly find the zeroth-order approximation of ω_p near the position x_s. Now the γ-factor is constant and its derivative vanishes. Then equation (4.8) gives

$$\omega_p(x_s) \approx \frac{\omega_{p0}}{\sqrt{\gamma(x_s)}} \equiv \omega_{p1} \tag{4.9}$$

To get the first-order correction, we can write $a(x) \approx a_s e^{-\omega_{p1}(x-x_s)}$ and set $x = x_s$ after calculating the second derivative of γ. In this case we obtain

$$\omega_{p2} = \sqrt{\frac{\omega_{p0}^2 + 2a_s^2\omega_{p1}^2}{\gamma(x_s)}}. \tag{4.10}$$

For the next higher-order approximations, we can insert ω_{p2} instead of ω_{p1} in the expression for $a(x)$ and so on in the same way. Consequently we obtain the sequence

$$\omega_{p\ n+1} = \sqrt{\frac{\omega_{p0}^2 + 2a_s^2\omega_{pn}^2}{\gamma(x_s)}}, \quad n = 1, 2, ... \tag{4.11}$$

The limit of this sequence is given by

$$\lim_{n\to\infty} \omega_{pn} = \frac{\omega_{p0}}{\sqrt{\gamma(x_s) - 2a_s^2}} \approx \frac{\omega_{p0}}{\sqrt{1 - \frac{3}{2}a_s^2}}. \tag{4.12}$$

Therefore we arrive at the approximate local plasma frequency at the position x_s under the assumption of small laser amplitudes within the skin layer:

$$\omega_p(x_s) \approx \frac{\omega_{p0}}{\sqrt{1 - \frac{3}{2}a_s^2}}. \tag{4.13}$$

This expression is larger than the background plasma frequency mainly due to density compression. Thus, the local plasma oscillations can excite electromagnetic waves at frequencies above the background plasma frequency. These waves can propagate through the plasma slab and exit from the rear side of the target. When the laser intensity is too high, plasma oscillations can have a fundamental frequency blow that of the background. However, if the oscillations are nonlinear, their harmonics can propagate through.

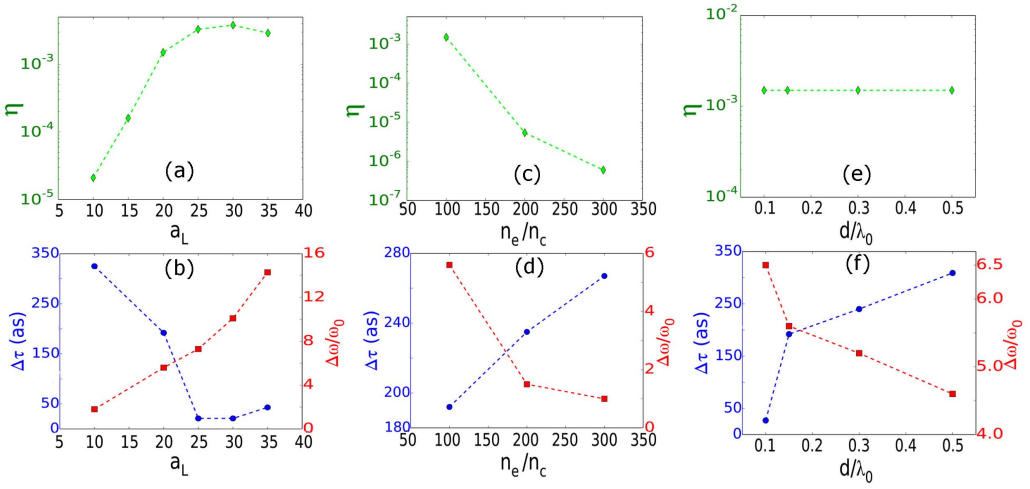

Figure 4.7: Influences of laser normalized amplitude a_L (a-b), initial plasma density n_e (c-d), and foil thickness d (e-f) on the XUV energy conversion efficiency η, XUV pulse FWHM width $\Delta\tau$, and XUV pulse FWHM bandwidth $\Delta\omega$. In these simulations, when one parameter is varied, the other parameters are the same with that presented in section 2. The laser amplitude is $a_L = 20$ in (c)-(f).

4.4 Discussions

4.4.1 Parametric study

Here we present a systematic study to show how the parameters such as laser intensity, initial plasma density and target thickness influence the generated XUV pulses. Figure 4.7(a) shows the energy conversion efficiency η grows with the normalized laser amplitude a_L, reaching about 4×10^{-3} when $a_L = 30$. Here, $\eta = \int E^2(\xi_{tr})d\xi_{tr} / \int E^2(\xi_0)d\xi_0$, with $\xi = t - x/c$, ξ_{tr} and ξ_0 denoting the transmitted and incident pulses, respectively. When a_L further increases, η decreases and the foil becomes more transparent to the laser pulse. Figure 4.7(b) suggests that higher laser intensity also favors the generation of XUV pulse with shorter FWHM duration $\Delta\tau$, and correspondingly broader FWHM bandwidth $\Delta\omega$. Figure 4.7(c)-(d) show the influence of the initial plasma density n_e. While $\Delta\tau$ increases and $\Delta\omega$ decreases with the increase of n_e, the conversion efficiency η drops rapidly. This is because wavebreaking and strong density oscillations are more difficult to drive for higher density plasmas. The laser intensity should also increase with the plasma density in order to keep the laser plasma dynamics the same, as indicated by the dimensionless similarity parameter $S = n_e/a_L n_c$ from the similarity theory in the ultrarelativistic regime $a_L^2 \gg 1$[48]. For the foil thickness d, it does not

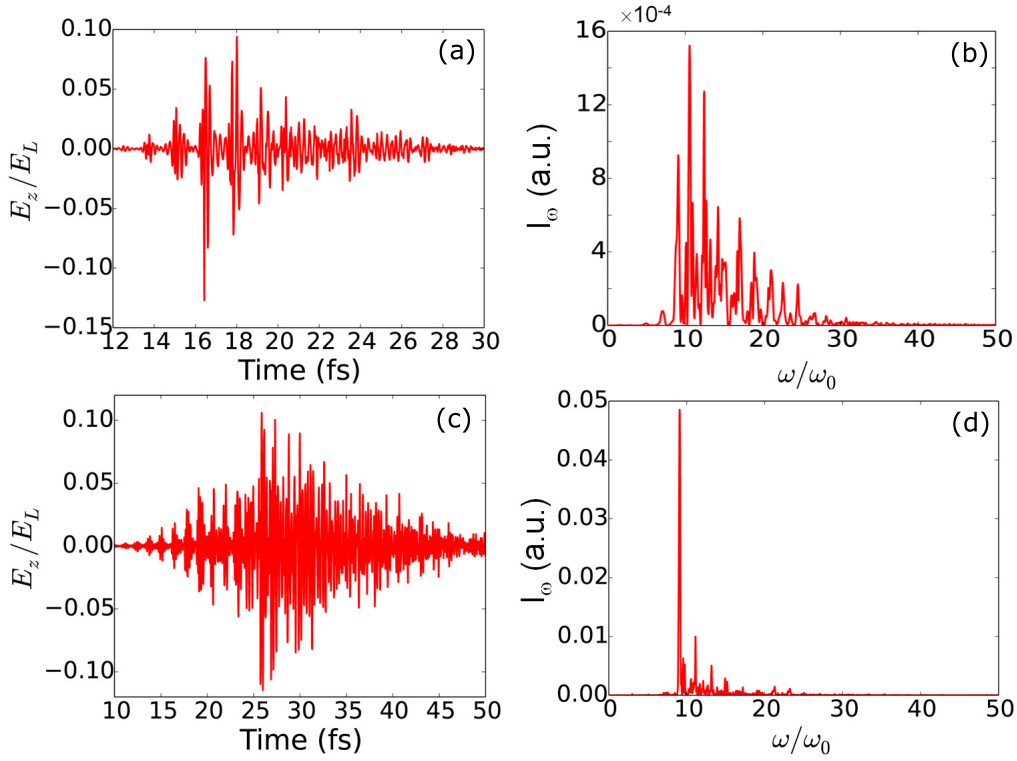

Figure 4.8: Temporal profile and the corresponding Fourier spectrum of the transmitted XUV emission for the case of using multi-cycle laser pulses. The laser pulse durations are 10 fs for frames (a)-(b) and 30 fs for (c)-(d). The other parameters are the same with that in Fig. 4.1(a).

affect the conversion efficiency, as shown in Fig. 4.7(e). This is understandable because the generation process occurs at the front layer of the target. However, $\Delta\tau$ increases with d while $\Delta\omega$ decreases (see Fig. 4.7(f)). This can be attributed to a result of dispersion when the pulses propagate through the plasmas.

4.4.2 Effect of laser pulse duration

Next we examine the WTE generation by considering two of the most concerns in real experimental cases, i.e., the effect of using multi-cycle laser pulses and presence of a finite plasma density gradient, to demonstrate the robustness of this mechanism.

Figure 4.8(a)-(b) show respectively the temporal profile and the Fourier spectrum of the WTE using a laser pulse with duration of 10 fs. The other parameters are the same with the case of $a_L = 20$ in the above simulations. It is seen that a

train of attosecond XUV pulses have been generated. The frequency spectrum contains finer structures than that in Fig. 4.1(b), as a result of the interference between different pulses in the attosecond pulse train. The effect of interference is more evident with a longer duration pulse of 30 fs, as shown in Figs. 4.8(c)-(d). Frequency components below $10\omega_0$ can be attributed to a lowered plasma frequency of the relativistically heated foil. Using techniques such as polarization gating, an isolated attosecond XUV pulse may be obtained. Nevertheless, these results shows the WTE mechanism also works by use of multi-cycle laser pulses.

4.4.3 Effect of plasma density gradient

Since the WTE process relies on the strong plasma-density oscillation subsequent to wavebreaking, a finite density ramp in the front of the plasma surface will affect the threshold of wavebreaking and thus the temporal and spectral structures of the WTE. From the cold nonrelativistic wavebreaking field $E_{WB} = m_e c\omega_p/e$, which is dependent on the plasma frequency and thus the plasma density, we see that a density ramp can lower the wavebreaking threshold. Consequently, the presence of a pre-plasma allows the WTE to occur more easily. This can be seen by considering a longer plasma gradient length. Figure 4.9(a) shows the temporal profile of the WTE for the case of an exponential plasma density gradient with scale length $L = \lambda_0/5$. The emitted pulse lasts a longer time of several femtoseconds, compared with the case of without pre-plasma in Fig. 4.1(a). This is due to an earlier wavebreaking and the subsequent strong density oscillation when the laser pulses interact with the density ramp in the front of the target, as shown in Figs. 4.9(c)-(d). We can see the multi-stream motion of electrons from the phase space distribution (x, P_x), indicating the wavebreaking has occurred (see Fig. 4.9(c)). At the same time, the profile of the transverse field E_z shows the waveform with higher frequencies (see Fig. 4.9(d)). Compared to the case of $L = \lambda_0/5$, the duration of the emitted pulse is shorter for the case of a shorter scale length of $L = \lambda_0/10$, as shown in Fig. 4.9(e). Correspondingly, the bandwidth of the spectrum in Fig. 4.9(f) is broader than that in Fig. 4.9(b).

4.4.4 Multi-dimensional effects

The results obtained so far are based on the 1D case. We also performed 2D simulations to check whether this mechanism works in multidimensional cases. Here we only intend to compare with the 1D results of the case shown in

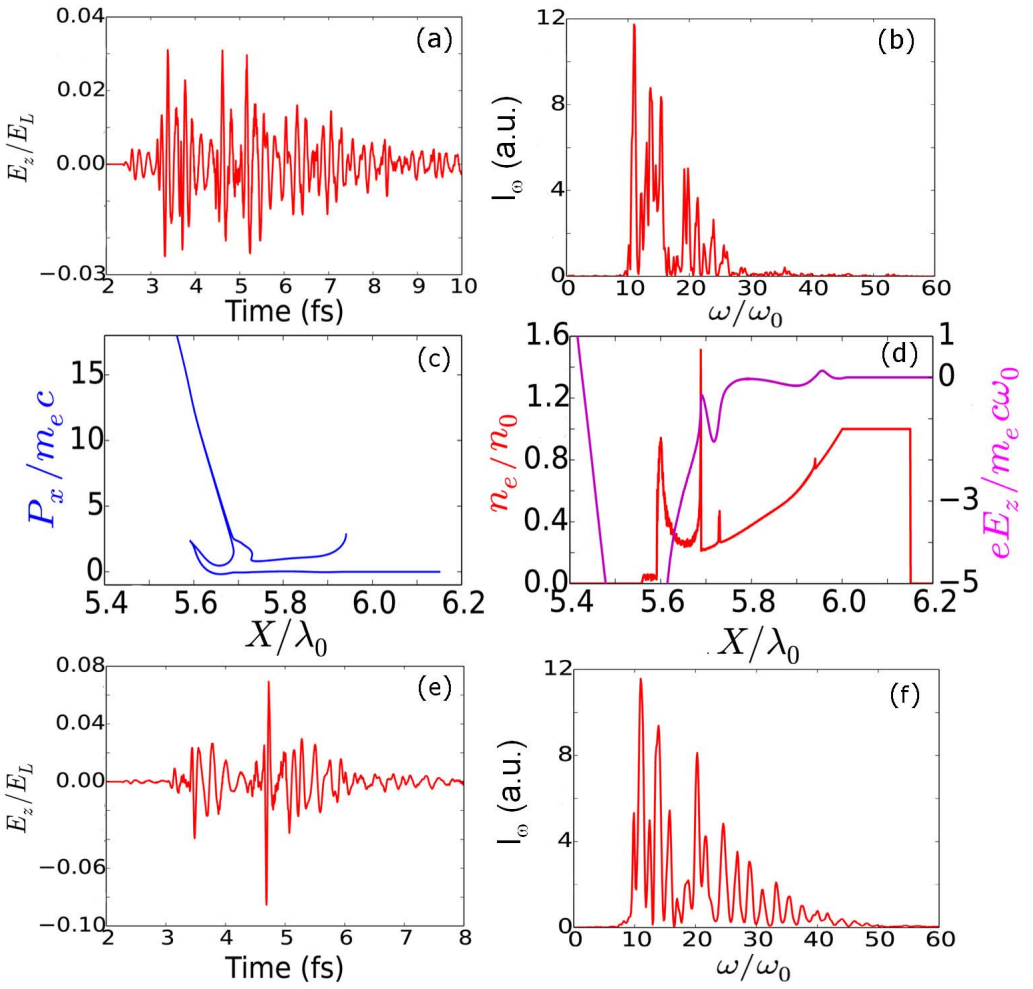

Figure 4.9: (a) Temporal profiles and (b) Fourier spectra of the transmitted XUV emission for an exponential plasma density gradient with scale length $L = \lambda_0/5$. (c) Phase space distribution (x, P_x) and (d) profiles of the electron density n_e and transverse field E_z at time $t = 3.4T_0$ for the case of $L = \lambda_0/5$. (e) Temporal profiles and (f) Fourier spectra of the transmitted XUV for the case of $L = \lambda_0/10$. The other parameters are the same with that in Fig. 4.1(a).

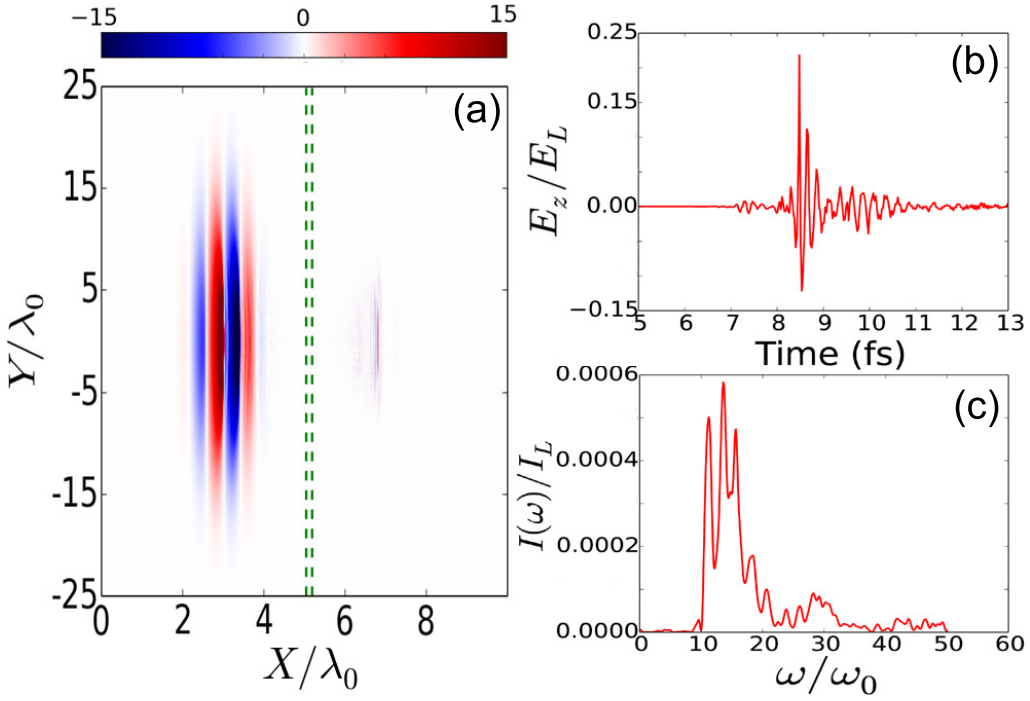

Figure 4.10: 2D simulation results. (a) A snapshot of the transverse electric field a_z distribution at simulation time $t = 5T_0$. The green dashed lines mark the initial plasma boundaries. (b) Temporal waveform and (c) frequency spectrum of the transmitted emission recorded at (x=6λ_0, y=0).

Fig. 4.1(a)-(b) to validate the basic physics. In the simulation, a very small grid step of $\lambda_0/1000$ is used in the x direction in order to resolve the wavebreaking related process. Each cell is filled with 8 macroparticles. The other laser and plasma parameters are the same with those used in Fig. 4.1(a)-(b) in the 1D simulations, except that the laser pulse has a Gaussian transverse profile with a focal spot size of $10\lambda_0$. Figure 4.10(a) shows a snapshot of the transverse electric field distribution at time $t = 5T_0$. We see that an ultrashort pulse is generated at the rear side of the target. Figures 4.10(b)-(c) show the temporal profiles and the corresponding frequency spectra of the transmitted emission observed at the position (x=$6\lambda_0$, y=0) at the rear target side, respectively. The signatures of both the temporal waveform and frequency spectrum are in good agreement with the 1D simulation results. An animated demonstration of the laser-plasma dynamics similar with the 1D case can be seen in movie SM3 in the Supplemental Material. The density spike indicating the onset of wavebreaking at $t = 3.11T_0$ and the subsequent transmitted emission at later times can be clearly seen from the movie. As for the concern of transverse instabilities, we note that experiments of femtosecond-picosecond laser interaction with nanometer-micrometer thin target are routinely available nowadays. A number of experiments have been carried out using similar parameters with ours. For example, experiments of a much longer pulse laser of 500 fs duration ($a_L \approx 20$) interacting with thin targets of thickness 125-200 nm have successfully demonstrated the transmitted emission due to the CSE mechanism[44]. These results indicate the transverse instabilities are not fatal with the parameters we considered here.

4.5 Conclusions

A new regime of attosecond XUV pulses generation from overdense plasma surfaces, namely, wavebreaking-associated transmitted emission (WTE), has been demonstrated. The emission originates from the plasma front surface and propagates through the target, with frequencies mainly around the local plasma frequencies. The underlying physics can be attributed to the coupling of the transverse fields in the skin layer and the strong plasma-density oscillation subsequent to wavebreaking. Thus the emission is evident only in the wavebreaking regime. This novel scenario of ultrafast XUV pulse emission from overdense plasmas provides new insights into the dynamics of laser-plasma interactions and

the physics of radiation process. It may also offer an alternative option to generate relativistically intense ultrashort XUV pulses that may find extensive applications.

Chapter 5

Summary

After detailed introduction in development of the laser technology and subsequently in different mechanisms of HHG, we started with the review of theoretical aspects concerning laser-plasma physics in chapter 2.

In chapter 3 we extensively investigated the nanobunching regime of HHG, represented by CSE mechanism. The main goal here was to provide a detailed analytical description of the radiated spectrum. For this purpose we have introduced a novel analytical approach in order to describe the electron density spikes close to stationary phase points. We started from the simple assumptions concerning the electron phase space distribution. As a result we obtained two analytic expressions, which describe the electron density profile in two different cases during the CSE process. We called those cases "parabolic case" and "whip case" respectively. Using these results we worked out the analytic equations for the transverse current distribution in corresponding cases using a set of assumptions. These equations led us directly to the analytic expressions of the spectrum. Further in this chapter we found the most efficient case of HHG at moderate laser intensity (a0 = 10), where the maximal amplitude of the reflected radiation was five times larger than the original one. We did several 1D PIC simulations varying the steepness of the exponential density gradient as well as the incident angle. Based on the simulation results the parameter spectra which corresponds to parabolic or "whip" cases were determined. In the last section of the chapter we found an electron bunch moving and radiating in the forward direction.

In chapter 4 we introduced and explored a new mechanism of attosecond pulse generation. Using a simulation set up with normal laser incidence and step plasma

density profile we obtained the transmitted XUV emission at the rare side of the foil. Analyzing the radiation process in detail we found out that the emission results from the strong electron density oscillations inside the skin layer after onset of wave breaking. Moreover we analyzed the plasma oscillations process analytically using some basic assumptions and derived the expression for the local plasma density inside the skin layer. At the end of the chapter the effects of the pulse duration, plasma density gradient as well as multidimensional effects were discussed.

Appendix A

Analytical derivations

A.1 Moving frame for oblique incidence.

Consider an electromagnetic wave which propagates within xy-plane and its velocity vector builds an angle θ with the x-axis in the laboratory frame L. Let us introduce another frame M which is moving parallel to the y-axis with velocity V (Fig. A.1). The velocity components of the wave can be expressed as

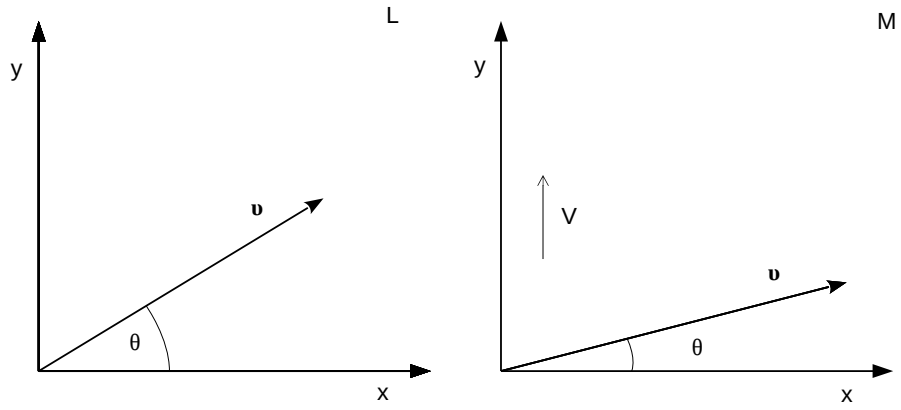

Figure A.1: Propagation direction of the electromagnetic wave considered from laboratory frame L and moving frame M.

$$v_x^L = c\cos\theta^L, \quad v_y^L = c\sin\theta^L \tag{A.1}$$

in the laboratory frame and as

$$v_x^M = c\cos\theta^M, \quad v_y^M = c\sin\theta^M \tag{A.2}$$

in the moving frame. These quantities are related to each other via the Lorenz transformation [63]

$$v_x^L = \frac{v_x^M\sqrt{1-\frac{V^2}{c^2}}}{1+\frac{v_y^M V}{c^2}}, \quad v_y^L = \frac{v_y^M + V}{1+\frac{v_y^M V}{c^2}}. \tag{A.3}$$

Taking the quotient of the both components in L leads to the relation between the angles

$$\frac{\cos\theta^L}{\sin\theta^L} = \frac{c\cos\theta^M\sqrt{1-\frac{V^2}{c^2}}}{c\sin\theta^M + V}. \tag{A.4}$$

We are interested in the case where the wave propagates parallel to the x-axis so that the angle θ^M vanishes. Thus, we set $\theta^M = 0$ and obtain

$$\frac{1}{\sin\theta}\sqrt{1-\sin^2\theta} = \frac{c}{V}\sqrt{1-\frac{V^2}{c^2}}. \tag{A.5}$$

Here we have dropped the index L and used $\cos\theta = \sqrt{1-\sin^2\theta}$. From the last equation we can immediately see that

$$V = c\sin\theta. \tag{A.6}$$

In this case we would see the electromagnetic wave normally incident on the plasma surface from the moving frame if the surface lays in the yz-plane.

Consider how each component of the electric and magnetic fields transforms in the moving frame. The transformation formulas for the field tensor are given by

$$E_x^M = \frac{E_x^L + \frac{V}{c}B_z^L}{\sqrt{1-\frac{V^2}{c^2}}}, \quad E_y^M = E_y^L, \quad E_z^M = \frac{E_z^L - \frac{V}{c}B_x^L}{\sqrt{1-\frac{V^2}{c^2}}}, \tag{A.7}$$

for electric field components and by

$$B_x^M = \frac{B_x^L - \frac{V}{c}E_z^L}{\sqrt{1-\frac{V^2}{c^2}}}, \quad B_y^M = B_y^L, \quad B_z^M = \frac{B_z^L + \frac{V}{c}E_x^L}{\sqrt{1-\frac{V^2}{c^2}}}, \tag{A.8}$$

for the magnetic field components. In the case of p-polarized wave the corresponding field vectors can be written as

$$\boldsymbol{E}^L = \begin{pmatrix} -E_0 \sin\theta \\ E_0 \cos\theta \\ 0 \end{pmatrix}, \quad \boldsymbol{B}^L = \begin{pmatrix} 0 \\ 0 \\ E_0 \end{pmatrix} \tag{A.9}$$

in laboratory frame. Applying the transformation formulas from above we obtain

$$\boldsymbol{E}^M = \begin{pmatrix} 0 \\ E_0 \cos\theta \\ 0 \end{pmatrix}, \quad \boldsymbol{B}^M = \begin{pmatrix} 0 \\ 0 \\ E_0 \cos\theta \end{pmatrix} \tag{A.10}$$

in the moving frame. Note that the x-component of the electric field vanishes in the moving frame under condition (A.6). We obtain a polarized wave which propagates parallel to the x-axis and has only one nonzero component $E_y^M = E_y^L = E_0 \cos\theta$. As a result the initial two dimensional problem of oblique incidence can be reduced to one dimension in the moving frame (Fig. A.2). Still we have to be

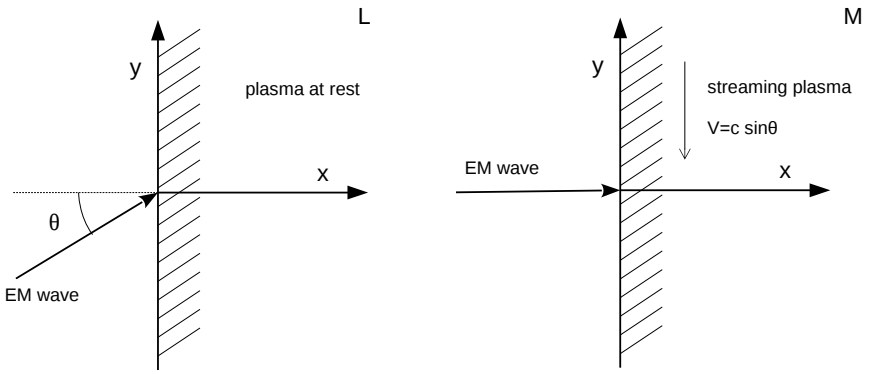

Figure A.2: Oblique incident wave in the laboratory frame L and normally incidence in the moving frame M.

careful, since the frequency of the wave in not the same in different frames.

If we consider the wave four-vector

$$k^i = \left(\frac{\omega}{c}, \boldsymbol{k}\right), \tag{A.11}$$

where $\boldsymbol{k}$ corresponds to the classical wave vector, we can obtain the relation between ω^L and ω^M. The time component of the wave four-vector transforms as

$$\frac{\omega^M}{c} = \frac{\frac{\omega^L}{c} - \frac{V}{c}k_y^L}{\sqrt{1-\frac{V^2}{c^2}}}, \tag{A.12}$$

and with $k_y^L = \frac{\omega}{c}\sin\theta$ we can easily derive the relation between both frequencies

$$\omega^M = \omega^L \cos\theta. \tag{A.13}$$

Moreover the transformation of the y-component yields $k_y^M = 0$ es expected.

The next important quantity is the electron density. The density at the curtain point ($\boldsymbol{r}$) can be expressed as

$$n(\boldsymbol{r}) = \frac{dN(\boldsymbol{r})}{dxdydz}. \tag{A.14}$$

Considering from the moving frame the plasma is streaming in the negative y-direction. Then dy transforms es

$$dy^M = dy^L\sqrt{1-\frac{V^2}{c^2}} = dy^L\cos\theta. \tag{A.15}$$

Consequently

$$n^M = \frac{n^L}{\cos\theta}. \tag{A.16}$$

Since we are working with the normalized quantities in our simulations, let us consider how the transformation formulas looks like for dimensionless units. In order to simulate the moving frame we just let the whole plasma move in the y-direction with some constant velocity. It means that the numerical wave length $\lambda_{\text{num}} = 1$ remains unchanged in each frame. With other words the central normalization parameter is now $\lambda = \lambda_0/\cos\theta$, where λ_0 is the wave length in the laboratory frame. First of all we notice that the normalized x-coordinates scale within

$$x_{\text{num}}^M = x_{\text{num}}^L \cos\theta. \tag{A.17}$$

Moreover the expression for the critical density (3.3) contains $\omega^2 = \omega_0^2 \cos^2\theta$. This fact together with the equation (A.16) results to

$$n_{\text{num}}^M = \frac{n_{\text{num}}^L}{\cos^3\theta}. \tag{A.18}$$

Further we consider the electric and magnetic fields. The important point is that due to the transformation into the moving frame, the amplitude of the wave is reduced by the factor $\cos\theta$

$$\left|\boldsymbol{E}^M\right| = E_0 \cos\theta = \left|\boldsymbol{E}^L\right| \cos\theta, \tag{A.19}$$

$$\left|\boldsymbol{B}^M\right| = E_0 \cos\theta = \left|\boldsymbol{B}^L\right| \cos\theta. \tag{A.20}$$

Nevertheless, if we consider the normalized amplitude, we notice that the normalization factor is reduced by the same factor in the moving frame since it contains ω in the numerator as we see from the equation (3.2). That means that the normalized amplitude of the wave remains unchanged

$$\left|\boldsymbol{E}_{\text{num}}^M\right| = \left|\boldsymbol{E}_{\text{num}}^L\right|, \quad \left|\boldsymbol{B}_{\text{num}}^M\right| = \left|\boldsymbol{B}_{\text{num}}^L\right|. \tag{A.21}$$

A.2 Density profile from phase space distribution containing delta function

A.2.1 Parabolic case

In section 3.2 we have started with the local phase space distribution function

$$f(x,p,t) = \mathcal{C}\delta\left(x - x_0(t) - \alpha(t)\left(p - p_0(t)\right)^2\right), \tag{A.22}$$

end expressed the density function with

$$n(x,t) = \int dp f(x,p,t). \tag{A.23}$$

So we have to calculate

$$n(x,t) = \mathcal{C}\int dp\ \delta\left(x - x_0(t) - \alpha(t)\left(p - p_0(t)\right)^2\right). \tag{A.24}$$

Let us define the argument of the delta function as a function $g(p)$

$$g(p) \equiv x - x_0(t) - \alpha(t)\left(p - p_0(t)\right)^2 . \tag{A.25}$$

With this definition the equation (A.24) takes the form

$$n(x,t) = \mathcal{C} \int dp\, \delta\left(g(p)\right). \tag{A.26}$$

Let us consider the general integral $\int dx\delta(g(x))$ with a smooth function g, which vanishes at the points x_i, with an integer i. We can Taylor expand the function g with respect to the certain point x_i

$$\begin{aligned} g(x) &= g(x_i) + (x - x_i)g'(x_i) + \mathcal{O}(x - x_i)^2 \\ &= (x - x_i)g'(x_i) + \mathcal{O}(x - x_i)^2. \end{aligned} \tag{A.27}$$

Consider a short interval $[x_i - \varepsilon, x_i + \varepsilon]$ with $\varepsilon > 0$. If ε tends to zero only first order survives and we can write

$$\lim_{\varepsilon \to 0} g(x)\Big|_{x \in [x_i - \varepsilon, x_i + \varepsilon]} = (x - x_i)g'(x_i). \tag{A.28}$$

This equation can also be easily proved using the definition

$$g'(x) = \lim_{\varepsilon \to 0} \frac{g(x + \varepsilon) - g(x)}{\varepsilon}. \tag{A.29}$$

Since the delta function equals zero everywhere except the cases where the argument vanishes, we can write

$$\int dx\delta(g(x)) = \lim_{\varepsilon \to 0} \sum_i \int_{x_i - \varepsilon}^{x_i + \varepsilon} dx\delta((x - x_i)g'(x_i)). \tag{A.30}$$

Consequently, we perform the integration using the simple substitution and obtain the result

$$\int dx\delta(g(x)) = \sum_i \frac{1}{|g'(x_i)|}, \quad \text{with} \quad g(x_i) = 0, \quad g'(x_i) \neq 0. \tag{A.31}$$

We use this relation in equation (A.26) and obtain

$$n(x,t) = \mathcal{C} \sum_i \frac{1}{|g'(p_i)|}, \quad \text{with} \quad g(p_i) = 0, \quad g'(p_i) \neq 0. \tag{A.32}$$

Now we need to find zero points and the first derivative of function g defined in (A.25). We find two zero points given by

$$p_i = p_0(t) + (-1)^i \sqrt{\frac{x - x_0(t)}{\alpha(t)}}, \quad i = 1, 2. \tag{A.33}$$

The derivative is given by

$$g'(p) = -2\alpha(t)\,(p - p_0(t))\,. \tag{A.34}$$

Using the zero points p_i as an argument of the derivative we obtain

$$g'(p_i) = (-1)^{i-1} 2\sqrt{\alpha(t)\,(x - x_0(t))}, \quad i = 1, 2. \tag{A.35}$$

Inserting this relation in equation (A.32) gives the result

$$n(x,t) = \frac{\mathcal{C}}{\sqrt{\alpha(t)\,(x - x_0(t))}}. \tag{A.36}$$

A.2.2 Whip case

Further in section 3.2 we have considered other distribution function

$$f(x,p) = \mathcal{C}\delta\left(x - e^{\alpha p}\right). \tag{A.37}$$

The density is given by

$$n(x) = \mathcal{C} \int dp\, \delta\left(x - e^{\alpha p}\right). \tag{A.38}$$

Now we define the argument of the delta function as a function $g(p)$

$$g(p) = x - e^{\alpha p}. \tag{A.39}$$

This function exhibits only one zero point

$$p_1 = \frac{1}{\alpha} \ln(x), \tag{A.40}$$

and the derivative of g is given by

$$g'(p) = -\alpha e^{\alpha p}. \tag{A.41}$$

At the point p_1 we have

$$g'(p_1) = -\alpha x. \tag{A.42}$$

Using the equation (A.32) we obtain the result

$$n(x) = \frac{\mathcal{C}}{\alpha x}. \tag{A.43}$$

A.3 Density profile from generalized phase space distribution

A.3.1 Parabolic case

Here we are going to calculate the integral (A.23) with the local phase space distribution

$$f_a(x,p) = \mathcal{C}\delta_a(x - \alpha p^2), \tag{A.44}$$

where the function δ_a is defined as

$$\delta_a(x) \equiv \begin{cases} g_a(x) & \text{for} \quad x \in [-a,a] \\ 0 & \text{otherwise} \end{cases}, \tag{A.45}$$

$$g_a(x) \equiv \frac{3}{4a}\left(1 - \frac{x^2}{a^2}\right). \tag{A.46}$$

An example of the function f_a is plotted in Fig. A.3. In order to calculate the local density profile we need to calculate

$$n_a(x) = \mathcal{C}\int dp\, \delta_a(x - \alpha p^2). \tag{A.47}$$

First, we have to determine the integration boundaries correctly to be able to replace δ_a with g_a in the integral. Inserting the argument $x - \alpha p^2$ in the definition of δ_a (A.45) we see that the equation $\delta_a(x - \alpha p^2) = g_a(x - \alpha p^2)$ holds only if the condition

$$-a \leq x - \alpha p^2 \leq a \tag{A.48}$$

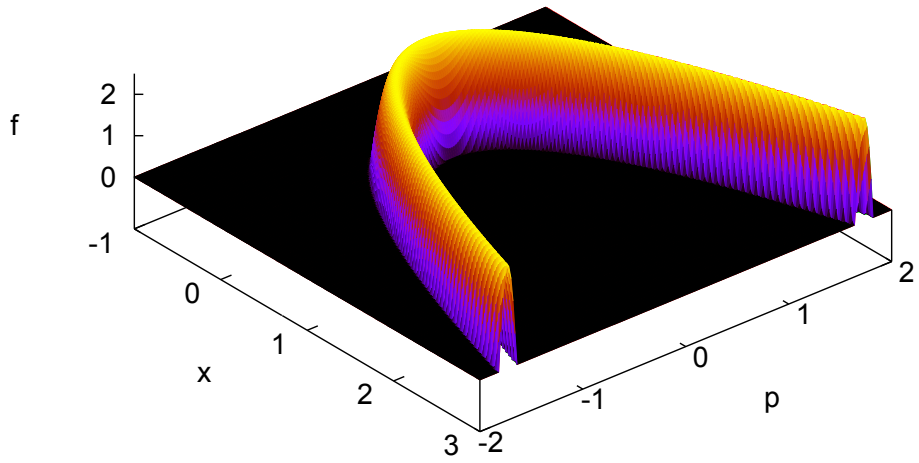

Figure A.3: The function $f_{0,3}(x,p)$ for $\alpha = 1$.

is fulfilled, which is equivalent to

$$\frac{x-a}{\alpha} \leq p^2 \leq \frac{x+a}{\alpha}. \tag{A.49}$$

From that point we have to distinguish three different cases.

- $x \geq a$:
  In this case the inequality (A.49) gives two conditions

$$\sqrt{\frac{x-a}{\alpha}} \leq p \leq \sqrt{\frac{x+a}{\alpha}} \tag{A.50}$$

$$-\sqrt{\frac{x+a}{\alpha}} \leq p \leq -\sqrt{\frac{x-a}{\alpha}} \tag{A.51}$$

- $-a \leq x < a$:
  In this case the term $\sqrt{\frac{x-a}{\alpha}}$ becomes imaginary and for the real values of p we obtain

$$-\sqrt{\frac{x+a}{\alpha}} \leq p \leq \sqrt{\frac{x+a}{\alpha}} \tag{A.52}$$

- $x < -a$:

  In this case there is no real values of p which can fulfill (A.49).

Now we have all the information that we need to write down the integrals for the different cases with corresponding integration boundaries. For the density profile that means that it will be a bounded support function

$$n_a(x) = \begin{cases} \mathcal{C} \int_{-\sqrt{\frac{x+a}{\alpha}}}^{-\sqrt{\frac{x-a}{\alpha}}} dp\, g(x-\alpha p^2) \\ + \mathcal{C} \int_{\sqrt{\frac{x-a}{\alpha}}}^{\sqrt{\frac{x+a}{\alpha}}} dp\, g(x-\alpha p^2) \quad \text{for} \quad x > a \\ \mathcal{C} \int_{-\sqrt{\frac{x+a}{\alpha}}}^{\sqrt{\frac{x+a}{\alpha}}} dp\, g(x-\alpha p^2) \quad \text{for} \quad x \in [-a, a], \quad a > 0 \\ 0 \qquad\qquad \text{for} \quad x < -a. \end{cases} \tag{A.53}$$

Using the symmetry properties of $g(x-\alpha p^2)$ within these boundaries this equation simplifies to

$$n_a(x) = \begin{cases} 2\mathcal{C} \int_{\sqrt{\frac{x-a}{\alpha}}}^{\sqrt{\frac{x+a}{\alpha}}} dp\, g(x-\alpha p^2) \quad \text{for} \quad x > a \\ 2\mathcal{C} \int_{0}^{\sqrt{\frac{x+a}{\alpha}}} dp\, g(x-\alpha p^2) \quad \text{for} \quad x \in [-a, a], \quad a > 0 \\ 0 \qquad\qquad \text{for} \quad x < -a. \end{cases} \tag{A.54}$$

Further steps are straight forward. We use the definition of the function g and define

$$\tilde{g}(p) \equiv \frac{4a^3}{3} g(x-\alpha p^2) = a^2 - \left(x - \alpha p^2\right)^2. \tag{A.55}$$

The antiderivative of $\tilde{g}$ is given by

$$\tilde{G}(p) = \left(a^2 - x^2\right) p + \frac{2}{3}\alpha x p^3 - \frac{1}{5}\alpha^2 p^5. \tag{A.56}$$

Inserting the corresponding boundaries and performing some elementary simplifications we obtain

$$\tilde{G}\Big|_{\sqrt{\frac{x-a}{\alpha}}}^{\sqrt{\frac{x+a}{\alpha}}} = \frac{4}{5\sqrt{\alpha}}\left(\left(a^2-\frac{2}{3}x^2\right)\left(\sqrt{x+a}-\sqrt{x-a}\right)+\frac{1}{3}ax\left(\sqrt{x+a}+\sqrt{x-a}\right)\right), \tag{A.57}$$

$$\tilde{G}\Big|_{0}^{\sqrt{\frac{x+a}{\alpha}}} = \frac{4}{5\sqrt{\alpha}}\left(a^2+\frac{1}{3}ax-\frac{2}{3}x^2\right)\sqrt{x+a}. \tag{A.58}$$

Now we substitute this result in equation (A.54) in the way that

$$\int_{p_1}^{p^2} dp\, g(x-\alpha p^2) = \frac{3}{4a^3}\tilde{G}\Big|_{p_1}^{p_2}. \tag{A.59}$$

Finally we insert the eqs. (A.57) to (A.59) in (A.54) and obtain

$$n_a(x) = \begin{cases} \dfrac{2\mathcal{C}}{5a^3\sqrt{\alpha}}\left(3a^2-2x^2+ax\right)\sqrt{x+a} & \text{for} \quad x\in[-a,a], \quad a>0 \\ \dfrac{2\mathcal{C}}{5a^3\sqrt{\alpha}}\Big(\left(3a^2-2x^2\right)\left(\sqrt{x+a}-\sqrt{x-a}\right) & \\ \qquad\qquad +ax\left(\sqrt{x+a}+\sqrt{x-a}\right)\Big) & \text{for} \quad x>a \\ 0 & \text{for} \quad x<-a. \end{cases} \tag{A.60}$$

Let us consider how this function behaves at the point $x=a$. We notate the density function as $n_{x<a}$ in the case of $x\in[-a,a]$ and as $n_{x>a}$ in the case of $x>a$. From equation (A.53) we can immediately see that $n_{x<a}(a)=n_{x>a}(a)$ holds, so the function n_a is continuous on the whole real axis. Next we check if the same is valid for the derivative. The derivatives of $n_{x<a}$ and $n_{x>a}$ are given by

$$n'_{x<a}(x) = (a-4x)\sqrt{x+a}+\frac{3a^2-2x^2+ax}{2\sqrt{x+a}}, \tag{A.61}$$

$$\begin{aligned} n'_{x>a}(x) = {} & (a-4x)\sqrt{x+a}+\frac{3a^2-2x^2+ax}{2\sqrt{x+a}} \\ & +(a+4x)\sqrt{x-a}-\frac{3a^2-2x^2-ax}{2\sqrt{x-a}}. \end{aligned} \tag{A.62}$$

In order to build the limit $x \to a$ for $n'_{x>a}$, we have to take a closer look at the last term of equation (A.62). In this limit the numerator as well as the denominator tend to zero, so we use the L'Hopital's rule to calculate the limit.

$$\lim_{x\to a} \frac{3a^2 - 2x^2 - ax}{2\sqrt{x-a}} = -\lim_{x\to a}(4x+a)\sqrt{x-a} = 0. \tag{A.63}$$

With this result we can directly follow

$$\lim_{x\to a} n'_{x<a}(x) = \lim_{x\to a} n'_{x>a}(x). \tag{A.64}$$

We have shown that the function n'_a is continuous for $x > -a$. That means that $n_a(x)$ is differentiable on this interval. In order to proof that the generalization we did in this section is correct, we are going to show that the limit $\lim_{a\to 0} n_{x>a}(x) = n(x)$ is valid (see equation (A.36)). To do this we multiply the first term of the function $n_{x>a}$ with the 1 expressed as $\frac{\sqrt{x+a}+\sqrt{x-a}}{\sqrt{x+a}+\sqrt{x-a}}$. We obtain

$$\begin{aligned} &n_{x>a}(x) \\ &= \frac{2\mathcal{C}}{5a^3\sqrt{\alpha}}\left(\frac{6a^3}{\sqrt{x+a}+\sqrt{x-a}} - \frac{4ax^2}{\sqrt{x+a}+\sqrt{x-a}} + ax\left(\sqrt{x+a}+\sqrt{x-a}\right)\right). \end{aligned} \tag{A.65}$$

Now we combine the last two terms and multiply the result with another "one term"

$$\begin{aligned} n_{x>a}(x) = \frac{2\mathcal{C}}{5a^2\sqrt{\alpha}}\Bigg(&\frac{6a^2}{\sqrt{x'+a}+\sqrt{x-a}} \\ &- 2x\left(\frac{x-\sqrt{x+a}\sqrt{x-a}}{\sqrt{x+a}+\sqrt{x-a}}\cdot\frac{x+\sqrt{x+a}\sqrt{x-a}}{x+\sqrt{x+a}\sqrt{x-a}}\right)\Bigg) \\ =&\frac{2\mathcal{C}}{5\sqrt{\alpha}}\left(\frac{6}{\sqrt{x+a}+\sqrt{x-a}} - \frac{2x}{\left(\sqrt{x+a}+\sqrt{x-a}\right)\left(x+\sqrt{x+a}\sqrt{x-a}\right)}\right). \end{aligned} \tag{A.66}$$

By this form of $n_{x>a}$ we can directly build the limit $a \to 0$ and obtain the correct result

$$\lim_{a\to 0} n_{x>a}(x) = \frac{2\mathcal{C}}{5\sqrt{\alpha}}\left(\frac{3}{\sqrt{x}} - \frac{1}{2\sqrt{x}}\right) = \frac{C}{\sqrt{\alpha x}}. \tag{A.67}$$

In the case of $x < a$ we can see relatively quick that

$$\lim_{a\to 0} n_{x<a}(x) = \begin{cases} \infty & \text{for} \quad x = 0 \\ 0 & \text{for} \quad x \neq 0. \end{cases} \tag{A.68}$$

In order to obtain the number of particles within the interval $[-a, \Delta x]$, we have to calculate

$$N_{a,\Delta x} = \int_{-a}^{\Delta x} dx\, n_a(x) = \int_{-a}^{a} dx\, n_{x<a}(x) + \int_{a}^{\Delta x} dx\, n_{x>a}(x) \tag{A.69}$$

This is a long calculation but each step is simple. We just need to apply the substitution to the arguments of corresponding square roots. Subsequently, we collect all the terms obtained after the integration and get

$$\begin{aligned} N_{a,\Delta x} = \frac{4\mathcal{C}}{35a^3\sqrt{\alpha}}\Big(&(8a^2\Delta x - 2\Delta x^3)\left(\sqrt{\Delta x + a} - \sqrt{\Delta x - a}\right) \\ &+ (a\Delta x^2 + 5a^3)\left(\sqrt{\Delta x + a} + \sqrt{\Delta x - a}\right)\Big). \end{aligned} \tag{A.70}$$

Now we want to simplify this result assuming $a \ll \Delta x$. For this purpose we rewrite the equation (A.70) in the way that

$$N_{a,\Delta x} = \frac{4\mathcal{C}}{35a^3\sqrt{\alpha}}\left(\Delta x M_{a,\Delta x} + 5a^3\left(\sqrt{\Delta x + a} + \sqrt{\Delta x - a}\right)\right), \tag{A.71}$$

$$M_{a,\Delta x} \equiv (8a^2 - 2\Delta x^2)\left(\sqrt{\Delta x + a} - \sqrt{\Delta x - a}\right) + a\Delta x\left(\sqrt{\Delta x + a} + \sqrt{\Delta x - a}\right). \tag{A.72}$$

We can see that the expression for $M_{a,\Delta x}$ is very similar to $n_{x>a}$ so we apply the same steps that we have used to calculate $\lim_{a\to 0} n_{x>a}(x)$

$$M_{a,\Delta x} \approx \frac{8a^3}{\sqrt{\Delta x}} - \frac{a^3}{2\sqrt{\Delta x}}. \tag{A.73}$$

Inserting this relation in equation (A.71) and neglecting a inside the square roots we obtain

$$N_{a,\Delta x} \approx \frac{4\mathcal{C}}{35a^3\sqrt{\alpha}}\left(\Delta x\left(\frac{8a^3}{\sqrt{\Delta x}} - \frac{a^3}{2\sqrt{\Delta x}}\right) + 10a^3\sqrt{\Delta x}\right) = 2\mathcal{C}\sqrt{\frac{\Delta x}{\alpha}} \tag{A.74}$$

It is not surprising, that the result is the same as in the spacial case of $a \to 0$ (see equation (3.12)). The important point here is that this relation holds even in

the case of $a \ll \Delta x$, as we could show. So it can be used in the density formula for general case if the assumption is satisfied. The final expression of the local electron density in this case is given by

$$n_{a,\Delta x}(x) = \begin{cases} \frac{N_{a,\Delta x}}{5a^3\sqrt{\Delta x}} \left(3a^2 - 2x^2 + ax\right) \sqrt{x+a} & \text{for} \quad x \in [-a, a] \\ \frac{N_{a,\Delta x}}{5a^3\sqrt{\Delta x}} \Big(\left(3a^2 - 2x^2\right) \left(\sqrt{x+a} - \sqrt{x-a}\right) & \\ \qquad + ax \left(\sqrt{x+a} + \sqrt{x-a}\right) \Big) & \text{for} \quad x > a \\ 0 & \text{for} \quad x < -a. \end{cases} \tag{A.75}$$

A.3.2 Whip case

Finally, we consider the phase space distribution

$$f_a(x,p) = \begin{cases} \mathcal{C}\delta_a\left(x - e^{\alpha p}\right) & \text{for} \quad p > p_{\text{cut}} \\ 0 & \text{for} \quad p \leq p_{\text{cut}}. \end{cases}$$

An example of the function f_a is plotted in Fig. A.4. The density profile can be obtained from

$$n_a(x) = \mathcal{C} \int_{p_{\text{cut}}}^{\infty} dp\, \delta_a(x - e^{\alpha p}). \tag{A.76}$$

Same as in the parabolic case, we are going to find the corresponding integration boundaries in order to replace δ_a with g_a. Here we take $x - e^{\alpha p}$ as an argument of these functions. They are equal under condition

$$-a \leq x - e^{\alpha p} \leq a. \tag{A.77}$$

This is equivalent to

$$\frac{1}{\alpha} \ln(x-a) \leq p \leq \frac{1}{\alpha} \ln(x+a). \tag{A.78}$$

The other condition is

$$p \geq p_{\text{cut}} = \frac{1}{\alpha} \ln(x_{\text{min}}). \tag{A.79}$$

Again we consider three different cases.

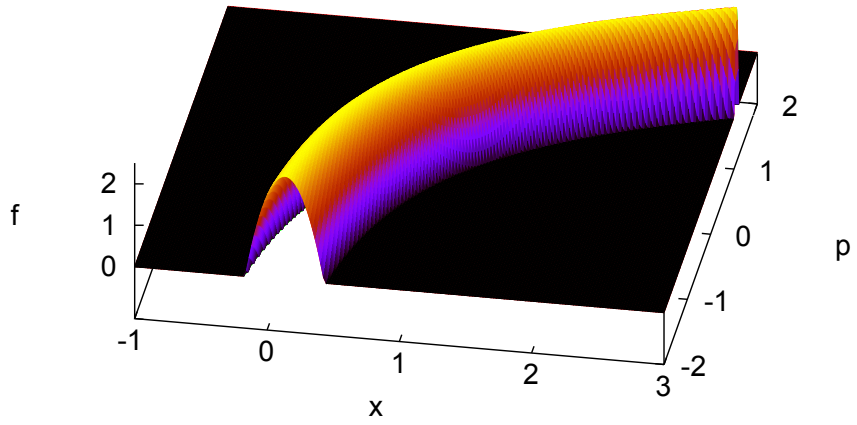

Figure A.4: The function $f_{0,3}(x,p)$ for $\alpha = 1$.

- $x \geq a + x_{\min}$:

  In this case we have

  $$\frac{1}{\alpha}\ln(x_{\min}) \leq \frac{1}{\alpha}\ln(x-a), \tag{A.80}$$

  so only the condition (A.78) is relevant.

- $-a + x_{\min} \leq x < a + x_{\min}$:

  Here we have

  $$\frac{1}{\alpha}\ln(x-a) \leq \frac{1}{\alpha}\ln(x_{\min}) \leq \frac{1}{\alpha}\ln(x+a), \tag{A.81}$$

  and the condition for p is given by

  $$\frac{1}{\alpha}\ln(x_{\min}) \leq p \leq \frac{1}{\alpha}\ln(x+a). \tag{A.82}$$

- $x < -a + x_{\min}$:

  In this case we have

  $$\frac{1}{\alpha}\ln(x_{\min}) \geq \frac{1}{\alpha}\ln(x+a), \tag{A.83}$$

and consequently there is no values of p which can fulfill both conditions (A.78) and (A.79).

Es a result we obtain the integration boundaries from eqs. (A.78) and (A.82) for the first two cases, while there is nothing to integrate in the third case. The expression for the density profile has the form

$$n_a(x) = \begin{cases} \mathcal{C} \int_{\frac{1}{\alpha}\ln(x_{\min})}^{\frac{1}{\alpha}\ln(x+a)} dp\, g(x - e^{\alpha p}) & \text{for} \quad x \in [x_{\min} - a, x_{\min} + a], \quad a > 0 \\ \mathcal{C} \int_{\frac{1}{\alpha}\ln(x-a)}^{\frac{1}{\alpha}\ln(x+a)} dp\, g(x - e^{\alpha p}) & \text{for} \quad x > x_{\min} + a \\ 0 & \text{for} \quad x < x_{\min} - a. \end{cases} \tag{A.84}$$

The calculation of the integrals is straight forward as in the previous case. The result is

$$n_a(x) = \begin{cases} \dfrac{3\mathcal{C}}{4a^3\alpha}\left(\dfrac{3}{2}x^2 + (a - 2x_{\min})x + \dfrac{1}{2}(x_{\min}^2 - a^2) + (x^2 - a^2)\ln\left(\dfrac{x_{\min}}{x+a}\right)\right) & \\ \qquad\qquad \text{for} \quad x \in [x_{\min} - a, x_{\min} + a] & \\ \dfrac{3\mathcal{C}}{4a^3\alpha}\left(2ax + (x^2 - a^2)\ln\left(\dfrac{x-a}{x+a}\right)\right) \quad \text{for} \quad x > x_{\min} + a & \\ 0 \qquad\qquad\qquad\qquad\qquad\qquad\qquad\qquad \text{for} \quad x < x_{\min} - a. \end{cases} \tag{A.85}$$

Same as in the previous case, we consider how this function behaves at the point $x = x_{\min} + a$. We notate the density function as $n_a^<$ in the case of $x \in [x_{\min} - a, x_{\min} + a]$ and as $n_a^>$ in the case of $x > x_{\min} + a$. Equation (A.84) tells that $n_a^<(x_{\min} + a) = n_a^>(x_{\min} + a)$ holds, so the function n_a is continuous on the whole real axis. Next, we check if the same is valid for the derivative. The derivatives of $n_a^<$ and $n_a^>$ are given by

$$n_a^{<\prime}(x) = 2(a - x_{\min} + x) + 2x\ln\left(\frac{x_{\min}}{x+a}\right), \tag{A.86}$$

$$n_a^{>\prime}(x) = 4a + 2x\ln\left(\frac{x-a}{x+a}\right). \tag{A.87}$$

From these equations it is easy to see that

$$n_a^{<\prime}(x_{\min}+a) = n_a^{>\prime}(x_{\min}+a) \tag{A.88}$$

is valid. This result proofs that the function n_a defined in (A.85) is continuous and differentiable at the point $x_{\min}+a$. Further, we are going to find the limit $\lim_{a\to 0} n_a^{>}(x)$ and expect that the result will coincide with equation (A.43). In order to build this limit we use the L'Hopital's rule. Let us define the function $\tilde{n}$ via

$$n_a^{>}(x) \equiv \frac{3\mathcal{C}}{4a^3\alpha}\tilde{n}(a,x). \tag{A.89}$$

the partial derivative of $\tilde{n}$ with respect to a is

$$\frac{\partial\tilde{n}}{\partial a} = 2a\ln\left(\frac{x+a}{x-a}\right), \tag{A.90}$$

subsequently we have

$$\lim_{a\to 0} n_a^{>}(x) = \lim_{a\to 0}\frac{\mathcal{C}}{2a\alpha}\ln\left(\frac{x+a}{x-a}\right). \tag{A.91}$$

One more derivation of the numerator and denominator gives

$$\lim_{a\to 0} n_a^{>}(x) = \lim_{a\to 0}\frac{\mathcal{C}}{\alpha}\frac{x}{x^2-a^2} = \frac{\mathcal{C}}{\alpha x} \tag{A.92}$$

as expected. We also use this limit to determine the number of particles. In this case it is not exactly the same as the assumption $a \ll x_{\max}$ like in the previous case. However, we usually deal with very thin nanobunch structures and use quite small values of a, so that the assumption $a \ll 1$ would make sense. Subsequently we use the same value for $\mathcal{C}$ as in equation (3.17) in the final formula

$$n_a(x) = \begin{cases} \dfrac{3N}{4a^3 \ln\left(\frac{x_{\max}}{x_{\min}}\right)} \left(\dfrac{3}{2}x^2 + (a - 2x_{\min})x + \dfrac{1}{2}(x_{\min}^2 - a^2) \right. \\ \qquad\qquad \left. + (x^2 - a^2) \ln\left(\dfrac{x_{\min}}{x+a}\right)\right) & \text{for} \quad x \in [x_{\min} - a, x_{\min} + a] \\ \dfrac{3N}{4a^3 \ln\left(\frac{x_{\max}}{x_{\min}}\right)} \left(2ax + (x^2 - a^2) \ln\left(\dfrac{x-a}{x+a}\right)\right) & \text{for} \quad x > x_{\min} + a \\ 0 & \text{for} \quad x < x_{\min} - a. \end{cases} \tag{A.93}$$

A.4 Derivation of the analytical spectrum

In this section we are going to derive an expression for the spectrum of the reflected field radiated by a nanobunch when it passes a SPP. The reflected field is given by

$$E_r(t) = -\pi \int J_\perp (x, t - x)\, dx, \tag{A.94}$$

while the spectrum is defined by

$$I(\omega) = \bar{E}_r^2(\omega), \quad \bar{E}_r(\omega) \equiv \int E_r(t) e^{-i\omega t} dt, \tag{A.95}$$

with the assumption

$$J_\perp(x, t) = j(t) f(x - x_0(t)). \tag{A.96}$$

At first we calculate the Fourier transform of the field

$$\begin{aligned} \bar{E}_r(\omega) &= -\pi \iint j(t - x) f(x - x_0(t - x)) e^{-i\omega t} dx dt \\ &= -\pi \iint j(t) f(x - x_0(t)) e^{-i\omega(t+x)} dx dt. \end{aligned} \tag{A.97}$$

With the substitution $\zeta \equiv x - x_0(t)$ we obtain

$$\begin{aligned} \bar{E}_r(\omega) &= -\pi \iint j(t) f(\zeta) e^{-i\omega(t+\zeta+x_0(t))} d\zeta dt \\ &= -\pi \int f(\zeta) e^{-i\omega\zeta} d\zeta \int j(t) e^{-i\omega(t+x_0(t))} dt. \end{aligned} \tag{A.98}$$

The first integral is nothing else but the Fourier transform of the shape function. Subsequently we squared the transformed field and get the general expression of the spectrum

$$I(\omega) = \pi^2 |\bar{f}(\omega)|^2 \left(\int j(t) e^{-i\omega(t+x_0(t))} dt \right)^2 . \tag{A.99}$$

At this point we have to specify the time dependent part of the current distribution $j(t)$ and the position of the nanobunch $x_0(t)$ at the curtain time in order to specify the expression of the spectrum. For that we again distinguish between the parabolic and the "whip" case.

A.4.1 Whip case

In the chapter 3 we have assumed

$$j(t) \approx \alpha_0 t^2, \quad x_0(t) \approx -\upsilon t + \alpha_1 \frac{t^5}{5}, \quad \text{with} \quad \alpha_1 = \frac{\alpha_0^2}{2\upsilon n_{\mathrm{m}}^2} \tag{A.100}$$

for the "whip" case in vicinity of the SPP. Inserting these expressions in equation (A.99) gives

$$I(\omega) = \pi^2 \alpha_0^2 |\bar{f}(\omega)|^2 \left(\int t^2 e^{-i\omega\left(\delta t + \alpha_1 \frac{t^5}{5}\right)} dt \right)^2 , \quad \text{with} \quad \delta = 1 - \upsilon. \tag{A.101}$$

To proceed further, we define the generalized Airy function

$$\mathrm{Ai}_n(x) = \frac{1}{2\pi} \int e^{i\left(xt + \frac{t^{2n+1}}{2n+1}\right)} dt. \tag{A.102}$$

From this definition we obtain the well known Airy function "Ai" for $n = 1$, $\mathrm{Ai}_1(x) = \mathrm{Ai}(x)$. Now we substitute $\tau \equiv -(\alpha_1\omega)^{\frac{1}{5}} t$ by the integration in (A.101) and get a compact expression of the spectrum

$$I(\omega) = 4\pi^4 \alpha_0^2 (\alpha_1\omega)^{-\frac{6}{5}} \left(Ai_2''(\alpha_1^{-\frac{1}{5}} \delta \omega^{\frac{4}{5}}) \right)^2 |f(\omega)|^2. \tag{A.103}$$

A.4.2 Parabolic case

The assumptions for this case were

$$j(t) \approx -\alpha_0 t, \quad x_0(t) \approx -\upsilon t + \alpha_1 \frac{t^3}{3}, \quad \text{with} \quad \alpha_1 = \frac{\alpha_0^2}{2\upsilon n_{\mathrm{m}}^2}. \tag{A.104}$$

Therefore the spectrum can be written as

$$I(\omega) = \pi^2 \alpha_0^2 |\bar{f}(\omega)|^2 \left(\int t e^{-i\omega\left(\delta t + \alpha_1 \frac{t^3}{3}\right)} dt \right)^2, \quad \text{with} \quad \delta = 1 - \upsilon. \tag{A.105}$$

In order to simplify this expression we substitute $\tau \equiv -(\alpha_1 \omega)^{\frac{1}{3}} t$ in the Integral, which leads to

$$I(\omega) = 4\pi^4 \alpha_0^2 (\alpha_1 \omega)^{-\frac{4}{3}} \left(Ai'(\alpha_1^{-\frac{1}{3}} \delta \omega^{\frac{2}{3}}) \right)^2 |f(\omega)|^2. \tag{A.106}$$

Appendix B

Authorship claim

The content of the chapter 3 is largely reproduced from my paper [61]. I wrote the whole text and did all the simulations and calculations. Alexander Pukhov was a supervisor and helped me with useful ideas and tips.

The content of the chapter 4 is largely reproduced from the paper [64]. My part was the detailed description of the given process after onset of wavebreaking. The description is divided in two main parts. First, I discuss the electron density oscillations (subsections 4.3.2, 4.3.3). Further the electron current behavior as an origin of transmitted radiation is described (subsection 4.3.4 "simulated transverse current"). Furthermore I did a significant contribution to Theoretical analysis (subsection 4.3.5 p73) and derived equation (4.13).

Bibliography

[1] T. H. Maiman. Stimulated optical radiation in ruby. *Nature*, 187:493–494, 1960. 1

[2] D. Strickland and G. Mourou. Compression of ampli-fied chirped optical pulses. *Opt. Commun.*, 56:219–211, 1985. 1

[3] M. Pessot, J. Squier, G. Mourou, and D. J. Harter. Chirped-pulse amplification of 100-fsec pulses. *Opt. Lett.*, 14:797–799, 1989.

[4] M. Pessot, J. Squier, P. Bado, G. Mourou, and D. J. Harter. Chirped pulse amplification of 300 fs pulses in an alexandrite regenerative amplifier. *J. Quantum Electron*, 25:61, 1989.

[5] F. G. Patterson and M. D. Perry. Design and performance of a multiterawatt, subpicosecond neodymium:glass laser. *J. Opt. Soc. Am. B*, 8:2384–2391, 1991.

[6] G. Mourou and D. Umstadter. Development and applications of compact high-intensity lasers. *Phys. Fluids B*, 4:2315, 1992.

[7] J. P. Watteau, G. Bonand, J. Coutant, P. Dautray, A. Decoster, M. Luis-Jaquet, J. Ouvry, J. Sauteret, S. Sezuec, and D. Teychenne. Experimental program on the 20 tw laser system. *Phys. Fluids B*, 4:2217, 1992.

[8] M. D. Perry and G. Mourou. Terawatt to petawatt subpicosecond lasers. *Science*, 264:917–924, 1994.

[9] G. Mourou. The ultrahigh-peak-power laser: present and future. *Appl. Phys. B: Lasers Opt.*, 65:205–211, 1997.

[10] A. Baltuska, M. Uiberacker, E. Goulielmakis, R. Kienberger, V. S. Yakovlev, T. Udem, T. W. Hansch, and F. Krausz. Phase-controlled amplification of few-cycle laser pulses. *IEEE J. Sel. Top. Quantum Electron.*, 9:972, 2003.

[11] P. A. Norreys, K. M. Krushelnick, and M. Zepf. Pw lasers: Matter in extreme laser fields. *Plasma Phys. Controlled Fusion*, 46:B13–B21, 2004.

[12] S. W. Bahk, P. Rousseau, T. A. Planchon, V. Chvykov, G. Kalintchenko, A. Maksimchuk, G. A. Mourou, and V. Yanovsky. Generation and characterization of the highest laser intensities (1022 w/cm2). *Opt. Lett.*, 29:2837–2839, 2004. 3

[13] G. A. Mourou, T. Tajima, and S. V. Bulanov. Optics in the relativistic regime. *Rev. Mod. Phys.*, 78:309–371, 2006.

[14] V. Yanovsky, V. Chvykov, G. Kalinchenko, P. Rousseau, T. Planchon, T. Matsuoka, A. Maksimchuk, J. Nees, G. Cheriaux, G. Mourou, and K. Krushelnick. Ultra-high intensity- 300-tw laser at 0.1 hz repetition rate. *Opt. Express*, 16:2109–2114, 2008.

[15] G. A. Mourou and T. Tajima. More intense, shorter pulses. *Science*, 331:41, 2011.

[16] Yuxi Chu, Xiaoyan Liang, Lianghong Yu, Yi Xu, Lu Xu, Lin Ma, Xiaoming Lu, Yanqi Liu, Yuxin Leng, Ruxin Li, , and Zhizhan Xu. High-contrast 2.0 petawatt ti:sapphire laser system. *Opt. Express*, 21:29231, 2013. 1

[17] G. Mourou, S. Mironov, E. Khazanov, and A. Sergeev. Single cycle thin film compressor opening the door to zeptosecond-exawatt physics. *Eur. Phys. J. Special Topics*, 223:1181–1188, 2014. 1, 3

[18] G. A. Mourou, N. J. Fisch, V. M. Malkin, Z. Toroker, E. A. Khazanov, A. M. Sergeev, T. Tajima, and B. Le Garrec. Exawatt-zettawatt pulse generation and applications. *Opt. Commun.*, 285:720, 2011. 2, 3

[19] F Krausz and M Ivanov. Attosecond physics. *Rev. Mod. Phys.*, 81:163, 2009. 3

[20] P Heissler. Two-photon above-threshold ionization using extreme-ultraviolet harmonic emission from relativistic laser–plasma interaction. *New J. Phys.*, 14:043025, 2012. 3

[21] A Borot. Attosecond control of collective electron motion in plasmas. *Nat. Phys.*, 8:416, 2012. 3

[22] S Dobosz. Probing hot and dense laser-induced plasmas with ultrafast xuv pulses. *Phys. Rev. Lett.*, 95:025001, 2005. 3

[23] R. L. Carman, D. W. Forslund, and J. M. Kindel. Visible harmonic emission as a way of measuring profile steepening. *Phys. Rev. Lett.*, 46:29–32, 1981. 3

[24] R. L. Carman, D. W. Forslund, and J. M. Kindel. Observation of harmonics in the visible and ultraviolet created in co2-laser produced plasmas. *Phys. Rev. A*, 24:2649–2663, 1981. 3

[25] M. Hentschel, R. Kienberger, Ch. Spielmann, G. A. Reider, N. Milosevic, T. Brabec, P. Corkum, U. Heinzmann, M. Drescher, and F. Krausz. Attosecond metrology. *Nature*, 414:509–513, 2001. 3

[26] A. Baltuska, T. Udem, M. Uiberacker, M. Hentschel, E. Goulielmakis, C. Gohle, R. Holzwarth, V. S. Yakovlev, T. W. Hansch A. Scrinzi, and F. Krausz. Attosecond control of electronic processes by intense light fields. *Nature*, 421:611, 2003.

[27] G. Sansone, E. Benedetti, F. Calegari, C. Vozzi, L. Avaldi, R. Flammini, L. Poletto, P. Villoresi, C. Altucci, S. Stagira R. Velotta, S. De Silvestri, and M. Nisoli. Isolated single-cycle attosecond pulses. *Science*, 314:443, 2006.

[28] E. Goulielmakis, M. Schultze, M. Hofstetter, V. Yakovlev, J. Gagnon, M. Uiberacker, A. L. Aquila, E. M. Gullikson, D. T. Attwood, R. Kienberger, F. Krausz, and U. Kleineberg. Single-cycle nonlinear optics. *Science*, 320:1614, 2008. 3

[29] C. Thaury, F. Quéré, J.P. Geindre, A. Levy, T. Ceccotti, P. Monot, M. Bougeard, and F. Réau. Plasma mirrors for ultrahigh-intensity optics. *Nature Physics*, 3:424–429, 2007. 4

[30] F. Quéré, C. Thaury, P. Monot, S. Dobosz, P. Martin, J.-P. Geindre, and P. Audebert. Coherent wake emission of high-order harmonics from overdense plasmas. *Phys. Rev. Lett.*, 96:125004, 2006.

[31] P. Heissler, R. Hörlein, M. Stafe, J. Mikhailova, Y.Nomura, D. Herrmann, R. Tautz, S. Rykovanov, I.Földes, K. Varju, F. Tavella, A. Marcinkevicius,

F. Krausz, L. Veisz, and G. Tsakiris. Toward single attosecond pulses using harmonic emission from solid-density plasmas. *Appl. Phys. B*, 101:511, 2010. 4

[32] S. V. Bulanov, N. M. Naumova, and F. Pegoraro. Interaction of an ultrashort, relativistically strong laser pulse with an overdense plasma. *Phys. Plasmas*, 1:745, 1994. 4

[33] R. Lichters, J. M. ter Vehn, and A. Pukhov. Short-pulse laser harmonics from oscillating plasma surface driven at relativistic intensity. *Phys. Plasmas*, 3:3425, 1996.

[34] D. von der Linde and K. Rzàzewski. High-order optical harmonic generation from solid surfaces. *Appl. Phys. B: Laser Opt.*, 63:499, 1996.

[35] S. Gordienko, A. Pukhov, O. Shorokhov, and T. Baeva. Relativistic doppler effect: Universal spectra and zeptosecond pulses. *Phys. Rev. Lett.*, 93:115002, 2004. 4

[36] S. Gordienko, A. Pukhov, O. Shorokhov, and T. Baeva. Coherent focusing of high harmonics: A new way towards the extreme intensities. *Phys. Rev. Lett.*, 94:101903, 2005. 5

[37] T. Baeva, S. Gordienko, and A. Pukhov. Theory of high-order harmonic generation in relativistic laser interaction with overdense plasma. *Phys. Rev. E*, 74:046404, 2006. 4, 40

[38] B. Dromey, M. Zepf, A. Gopal, K. Lancaster, M. S. Wei, K. Krushelnick, M. Tatarakis, N. Vakakis, S. Moustaizis, R. Kodama, M. Tampo, C. Stoeckl, R. Clarke, H. Habara, D. Neely, S. Karsch, and P. Norreys. High harmonic generation in the relativistic limit. *Nat. Phys.*, 2:456–459, 2006. 4

[39] B. Dromey, S. Kar, C. Bellei, D. C. Carroll, R. J. Clarke, J. S. Green, S. Kneip, K. Markey, S. R. Nagel, P. T. Simpson, L. Willingale, P. McKenna, D. Neely, Z. Najmudin, K. Krushelnick, P. A. Norreys, and M. Zepf. Bright multi-kev harmonic generation from relativistically oscillating plasma surfaces. *Phys. Rev. Lett.*, 99:085001, 2007.

[40] P. Heissler, R. Hörlein, J. M. Mikhailova, L. Waldecker, P. Tzallas, A. Buck, K. Schmid, C. M. S. Sears, F. Krausz, L. Veisz, M. Zepf, and G. D. Tsakiris. *Phys. Rev. Lett.*, 108:235003, 2012. 4

[41] F. Brunel. Not-so-resonant, resonant absorption. *Phys. Rev. Lett.*, 59:52–55, 1987. 4

[42] D. an der Brügge and A. Pukhov. Enhanced relativistic harmonics by electron nanobunching. *Phys. Plasmas*, 17:033110, 2010. 4, 5, 55

[43] D. an der Brügge and A. Pukhov. Theory of attosecond pulses from relativistic surface plasmas. e-print arXiv:physics/1111.4133, 2011. 4, 5, 40, 43, 45, 47, 55

[44] B. Dromey, M. S. Rykovanov, M. Yeung, R. Horlein, D. Jung, D. C. Gautier, T. Dzelzainis, D. Kiefer, S. Palaniyppan, R. Shah, J. Schreiber, H. Ruhl, J. C. Fernandez, C. L. S. Lewis, M. Zepf, and B. M. Hegelich. Coherent synchrotron emission from electron nanobunches formed in relativistic laserplasma interactions. *Nat. Phys.*, 8:804–808, 2012. 4, 54, 79

[45] B. Dromey, S. Cousens, S. Rykovanov, M. Yeung, D. Jung, D. C. Gautier, T. Dzelzainis, D. Kiefer, S. Palaniyppan, R. Shah, J. Schreiber, J. C. Fernandez, C. L. S. Lewis, M. Zepf, and B. M. Hegelich. Coherent synchrotron emission in transmission from ultrathin relativistic laser plasmas. *New J. Phys.*, 15:015025, 2013. 54, 59, 63

[46] M. Yeung, B. Dromey, S. Cousens, T. Dzelzainis, D. Kiefer, J. Schreiber, J. H. Bin, W. Ma, C. Kreuzer, J. Meyerter-Vehn, M. J. V. Streeter, P. S. Foster, S. Rykovanov, and M. Zepf. Dependence of laser-driven coherent synchrotron emission efficiency on pulse ellipticity and implications for polarization gating. *Phys. Rev. Lett.*, 122:123902, 2014. 4

[47] A. A. Gonoskov, A. V. Korzhimanov, A. V. Kim, M. Marklund, and A. M. Sergeev. *Phys. Rev. E*, 84:046403, 2011. 4, 5

[48] S. Gordienko and A. Pukhov. Scalings for ultrarelativistic laser plasmas and quasimonoenergetic electrons. *Phys. Plasmas*, 12:043109, 2005. 5, 74

[49] S. G. Rykovanov, M. Geissler, J. Meyer ter Vehn, and G. D. Tsakiris. Intense single attosecond pulses from surface harmonics using the polarization gating technique. *New J. Phys.*, 10:025025, 2008. 5

[50] T. Baeva, S. Gordienko, and A. Pukhov. Relativistic plasma control for single attosecond x-ray burst generation. *Phys. Rev. E*, 74:065401, 2006. 5

[51] A. Pukhov. X-rays in a flash. *Nat. Phys.*, 2:439, 2006. 5

[52] N. M. Naumova, J. A. Nees, I.V. Sokolov, B. Hou, and G. A. Mourou. Relativistic generation of isolated attosecond pulses in a λ^3 focal volume. *Phys. Rev. Lett.*, 92:063902, 2004. 5

[53] Andrzej Wolski. Theory of electromagnetic fields. e-print arXiv:physics/1111.4354, 2011. 9

[54] P. W. Milonni and J. H. Eberly. *Lasers*. Wiley, New York, 1988. 9, 10, 11, 12

[55] Miguel A. Porras. Diffraction effects in few-cycle optical pulses. *Phys. Rev. E*, 65:026606, 2002. 12, 14

[56] William L. Kruer. *The physics of laser plasma interactions*. Addison-Wesley, California, 1988. 14

[57] E. Esarey, C. B. Schroeder, and W. P. Leemans. Physics of laser-driven plasma-based electron accelerators. *Rev. Mod. Phys.*, 81:1229, 2009. 14, 21

[58] John M. Dawson. Nonlinear electron oscillations in a cold plasma. *Phys. Rev.*, 113:383, 1958. 18, 20, 66

[59] Kazumi Watanabe. *Definition of Integral Transforms and Distributions*. Springer International Publishing, Cham, 2014. 23

[60] I. S. Gradshteyn and I. M. Ryzhik. *Table of integrals, series, and products*. Elsevier/Academic Press, Amsterdam, 2007. 23, 24

[61] M. Cherednychek and A. Pukhov. Analytical approach to high harmonics spectrum in the nanobunching regime. *Physics of Plasmas*, 23:103301, 2016. 27, 103

[62] A. Pukhov. Three-dimensional electromagnetic relativistic particle-in-cell. *J. Plasma Phys.*, 61:425, 1999. 27, 59

[63] L. D. Landau and E. M. Lifshitz. *The Classical Theory of Fields*. Pergamon, New York, 1964. 28, 84

[64] Z. Chen, M. Cherednychek, and A. Pukhov. Wavebreaking-associated transmitted emission of attosecond extreme-ultraviolet pulses from laser-driven overdense plasmas. *New J. Phys.*, 18:063014, 2016. 59, 103

[65] C. Thaury and F. Quéré. High-order harmonic and attosecond pulse generation on plasma mirrors: basic mechanisms. *J. Phys. B: At. Mol. Opt. Phys.*, 43:213001, 2010. 59, 60, 62

[66] T. P. Coffey. Breaking of large amplitude plasma oscillations. *Phys. Fluids*, 14:1402, 1971. 66

[67] C. B. Schroeder. Warm wave breaking of nonlinear plasma waves with arbitrary phase velocities. *Phys. Rev. E*, 72:055401(R), 2005. 66

[68] D. Bauer. Relativistic ponderomotive force, uphill acceleration, and transition to chaos. *Phys. Rev. Lett.*, 75:4622, 1995. 72

[69] A. Macchi. *A Superintense Laser-Plasma Interaction Theory Primer*. Springer, Dordrech, 2013. 72